Real-time capable individual-ion qubit measurement

Von der Fakultät für Mathematik und Physik
der Gottfried Wilhelm Leibniz Universität Hannover

zur Erlangung des Grades

Doktor der Naturwissenschaften
- Dr. rer. nat. -

genehmigte Dissertation von

M.Sc. Sebastian Halama, geb. Grondkowski

2021

Referent:	Prof. Dr. Christian Ospelkaus Institut für Quantenoptik Leibniz Universität Hannover
Korreferent:	Prof. Dr. Piet O. Schmidt Institut für Quantenoptik Leibniz Universität Hannover
Korreferent:	Prof. Dr. Christof Wunderlich Department Physik Universität Siegen
Tag der Disputation:	13. Dezember 2021

Abstract

Scaling up the number of qubits for quantum simulation and quantum computation and reaching a low error rate of the involved quantum logic operations are the major challenges in the development of a fault-tolerant universal quantum computer. Trapped ions in surface-electrode traps are a promising candidate that could satisfy both criteria. These traps can be extended into a two-dimensional array, a so-called quantum charge-coupled device, in which the ions can be moved around to different zones that fulfill a specific task. In this way an architecture can be developed that could perform multiple quantum-logic operations with many ions simultaneously.

These operations were first implemented with laser beams and have evolved in the past years to a point where they are almost reaching the threshold for fault tolerance. However, this approach is fundamentally limited by spontaneous emission and is hard to scale up to a large number of qubits. An alternative approach using microwave radiation can overcome these problems. The microwave conductors can be integrated into the surface-electrode traps and therefore feature the same scalability as the trap itself. A small distance between the ions and the microwave conductors in the trap-surface is desirable to reach a strong field to drive the quantum logic operations. A downside of a reduced distance is an increased motional heating rate of the ions. To counteract this effect, the trap can be cooled down to cryogenic temperatures. Cooling the trap and its surrounding also helps to achieve excellent vacuum conditions that are required to reduce the collision rate of the ions with background gas molecules. These collisions would be fatal during a sequence of quantum logic operations.

Another important factor for the operation of a quantum simulator or quantum computer is the ability to prepare the ions in a known state and to detect the state of the ions. In this thesis, we explain how an EMCCD camera can be used as a spatially resolving detector to readout the state of each ion simultaneously and we discuss the benefits and limitations of this technique. We could show that the combined error-rate of state preparation and camera-based detection is on the order of 0.4 % which is comparable with a photomultiplier-based detection for a single ion. We also demonstrated that the camera-based detection outperforms the photomultiplier when the state of two ions should be detected. Here we determined the amount of crosstalk between two ions to be so low that the error-rate is basically independent of the number of simultaneously detected qubits. We also discuss options for future improvements of the state preparation and detection system to further reduce the error rate.

Keywords: cryogenic surface-electrode ion trap, individual-ion state detection, EMCCD camera, SPAM error, microwave near-field, quantum simulation, quantum computation

Contents

1 Introduction

Simulating a quantum mechanical system is a challenging task for a classical computer. The amount of required memory scales exponentially with the number of involved particles [1] and can easily outrun the number of protons in the universe. To bypass this problem, Feynman proposed to simulate a quantum system with another better controllable quantum system [2]. Following this idea ultimately leads to the concept of a universal quantum computer that can simulate any arbitrary quantum system. Such a quantum computer stores its information in quantum bits, or *qubits*, that are realized by a well-controllable quantum mechanical two-level system. In contrast to a classical computer which stores the information in bits that can either be 0 or 1, the information stored in qubits can be any superposition between the two qubit states, usually named $|0\rangle$ and $|1\rangle$ to emphasize the relationship to the classical information, or sometimes $|\downarrow\rangle$ and $|\uparrow\rangle$ to point out that the quantum information is stored in the spin, a purely quantum mechanical quantity. Utilizing the superposition principle can drastically increase computational power and has led to the development of several quantum algorithms. The most prominent ones are Shor's algorithm [3] to find the prime factors of a given number and Grover's algorithm [4] for function inversion.

A universal quantum computer has to fulfill the so-called DiVincenzo-criteria [5]. These demand for "a scalable physical system with well characterized qubits", "the ability to initialize the state of the qubits to a simple fiducial state", "long relevant decoherence times, much longer than the gate operation time", "a 'universal' set of quantum gates" and "a qubit-specific measurement capability". There are multiple platforms available that can fulfill these criteria, each one with its own advantages and disadvantages. Among these the superconducting qubits [6] and trapped ions [7] are currently the most promising ones, but neutral atoms in optical lattices [8], Rydberg atoms [9], quantum dots [10], nitrogen-vacancy centers [11] and photonic qubits [12] are also investigated.

The progress made in the development of quantum computers based on superconductors [13] has recently aroused great interest inside and outside of the scientific community. With 53 qubits, this system belongs to the *noisy intermediate-scale quantum* (NISQ) regime [14]. Here the number of qubits is high enough that the computations cannot be done efficiently on a classical computer anymore. However, the error-rate and number of qubits is still far away from what is needed

for fully fault-tolerant quantum computing. Quantum error-correction protocols require several physical qubits to realize one logical qubit, therefore increasing the number of required qubits, and estimates have been made that error rates on the order of 10^{-4} are required [15] to be able to implement fault-tolerant quantum algorithms.

At this point the trapped-ion platform has specific advantages. While yet lacking a number of qubits comparable to the superconductor approach, the error rates are much lower for trapped ions, reaching 10^{-6} for single-qubit gates [16] and approaching 10^{-4} for laser-based two-qubit gates [17, 18]. Alternative approaches have been developed that do not rely on laser beams to implement the quantum logic operations, but instead use microwave radiation [19, 20] and currently achieve error rates in the 10^{-3} range [21, 22].

Scaling up the number of controllable qubits is a major challenge for every quantum computing platform. A promising approach could be the *quantum charge-coupled device* (QCCD) [23, 24] that consists of a two-dimensional array of ion traps with the ability to transfer ions between individual zones. The QCCD architecture has already been demonstrated to work in one dimension with six qubits [25]. A promising ion trap technology capable of realizing a two-dimensional QCCD is the surface-electrode ion-trap [26]. The key elements to scale up these traps in two dimensions are the junctions that have already been demonstrated to work in the 'Y'-configuration [27] and in the 'X'-configuration [28]. These chip-based traps allow for the integration of additional components like microwave conductors [29], fibers [30, 31], optics [32] or detectors [33, 34, 35].

Integrated microwave conductors can be used to perform laserless quantum logic operations and therefore simplify scaling up the trap structure to a higher number of qubits. However, this technique comes with its own challenges. The ions must be located relatively close to the trap surface to experience a microwave field that is strong enough to perform the quantum logic operations in a reasonably short time. Usually the ions are trapped a few tens of micrometers above the surface and gate times on the order of microseconds to milliseconds are achieved. A small distance to the trap surface leads to an increased heating rate due to anomalous motional heating that inversely scales with the fourth power of the distance [36]. A high heating rate can lead to a reduced fidelity of the quantum logic operations and also to loss of ions. To compensate the increased heating rate, the ion trap can be cooled down to cryogenic temperatures [37] or it can be cleaned with Argon-ion-beam bombardment [38]. A cryogenic environment also features excellent vacuum conditions that lead to reduced collisions with background gas molecules [39]. These collisions would disturb the state of the ions in an unpredictable way and can lead to ion loss, which would both be serious problems for a quantum information processor with a large number of qubits.

At the end of a quantum computation or simulation, the state of the qubits has to be read out. As previously mentioned, the detectors for this task can be integrated into the trap structure. However, an external detector also has its benefits in terms of easier reconfigurability. Especially for quantum simulation purposes this can be important when multiple qubits must be read out

simultaneously. It has been demonstrated that a multichannel photo-multiplier tube [40] and an EMCCD camera [41] can be used for this purpose.

In the context of this thesis, an EMCCD camera was taken into operation for individual-ion state detection of $^9Be^+$ ions in a cryogenic surface-electrode ion trap. In **chapter 2**, the basic working principles of the experimental apparatus are described. This includes the relevant energy levels in $^9Be^+$, the trap and its surroundings, electronic signals and their generation, laser systems as well as the properties of the imaging and detection system. In **chapter 3**, the foundation for individual-ion state detection using an EMCCD camera are laid. We present the effect of the different camera settings on the detection efficiency and discuss the flaws of the used EMCCD camera and how to work around them. In **chapter 4**, we present experiments that were conducted with one or two ions and the outcome was detected with either a photomultiplier tube or the EMCCD camera. We discuss the differences between the two detection methods and point out what the benefits of the detection with the EMCCD camera are. In **chapter 5**, we summarize the results obtained during the course of this thesis and give an outlook on the future development of our experiment.

2 Experimental techniques

In this chapter, we will discuss how we make use of the energy level structure of $^9Be^+$ to implement a qubit. We describe how our cryogenic surface-electrode ion trap works and which hardware is required to operate it. This covers the mechanical aspects of the system as well as the electronics, laser systems and imaging optics that we are using in our lab.

2.1 Energy levels in Beryllium

In this section, the energy levels of $^9Be^+$ and the relevant transitions for the experiments performed in the context of this thesis will be discussed. Beryllium ions offer several transitions in the ground state manifold which are insensitive to magnetic field fluctuations in first order at certain magnetic field strengths. This property results in a higher coherence time of the qubit compared to field-sensitive transitions [42] and therefore allows for higher gate fidelities. The magnetic field dependence of the ground state hyperfine levels of $^9Be^+$ is shown in figure 2.1.

There are first-order field-independent transitions available around an external magnetic field of approximately 12 mT, which have $\Delta m_F = \pm 1$ and require a circular polarization of the driving field [43]. Because the oscillating magnetic field produced by our integrated microwave conductors is linearly polarized, it is advantageous to use a transition with $\Delta m_F = 0$. Such a transition is available at a field of $B_0 \approx 22.3\,\mathrm{mT}$. Here the transition frequency between the states $|2,1\rangle$ and $|1,1\rangle$ (labeled "Q" in figure 2.1) reaches a minimum at around 1082.55 MHz.

Besides the two qubit states, more states are involved for laser cooling, state preparation and detection. The level structures of the $2^2S_{\frac{1}{2}}$ ground state and the $2^2P_{\frac{3}{2}}$ excited state of $^9Be^+$ at an external magnetic field $B_0 = 22.3\,\mathrm{mT}$ are shown in figure 2.2. The Beryllium ion is Doppler-cooled on the closed-cycle transition $2^2S_{\frac{1}{2}}\,|2,2\rangle \leftrightarrow 2^2P_{\frac{3}{2}}\,|\frac{3}{2},\frac{3}{2}\rangle$, where the numbers in the ket-notation stand for $|F,m_F\rangle$ for the $2^2S_{\frac{1}{2}}$ levels and $|m_J,m_I\rangle$ for the $2^2P_{\frac{3}{2}}$ levels. This cooling transition is driven with a σ^+ polarized laser beam with a wavelength of around 313 nm. While this laser beam is switched on, the population in the different hyperfine levels in the ground state is optically pumped to the $|2,2\rangle$ state, which serves as the bright state.

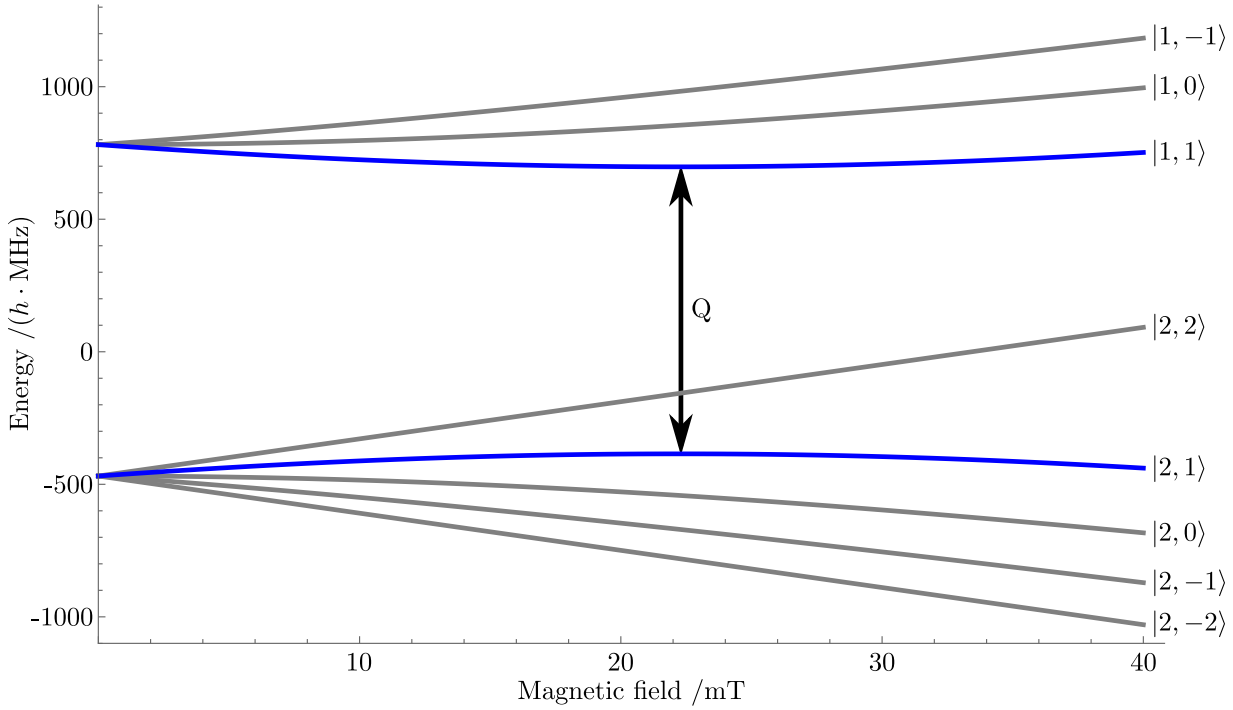

Figure 2.1: Magnetic-field dependence of the hyperfine states in the $2^2S_{\frac{1}{2}}$ ground state of $^9Be^+$. The two levels used as qubit states are highlighted in blue. At an external magnetic field of $B_0 \approx 22.3\,\mathrm{mT}$, the transition "Q" becomes field-insensitive to first order. The nomenclature to describe the states is $|F, m_F\rangle$.

After Doppler cooling, the qubit can be initialized by applying a microwave π-pulse on transition "A" with frequency $f_A \approx 853.644\,\mathrm{MHz}$. Quantum logic operations can now be performed on the field-independent qubit-transition "Q" which has a frequency of $f_Q \approx 1082.55\,\mathrm{MHz}$. In order to detect the outcome of the qubit operations, the qubit states $|\uparrow\rangle \equiv |1,1\rangle$ and $|\downarrow\rangle \equiv |2,1\rangle$ must be mapped to a bright and a dark state, which yield a distinguishable number of scattered photons during the detection interval. The population in $|\uparrow\rangle$ is transferred to the bright state $|2,2\rangle$ with another π-pulse on transition "A". The state with the smallest probability of being excited by the detection laser due to its large detuning is the $|1,-1\rangle$ state which serves as dark state. To transfer the population in $|\downarrow\rangle$ to the dark state, a series of three microwave π-pulses labeled "B", "C" and "D" is applied with frequencies $f_B \approx 1239.92\,\mathrm{MHz}$, $f_C \approx 1397.56\,\mathrm{MHz}$ and $f_D \approx 1525.46\,\mathrm{MHz}$.

After all of these transfer pulses - also called shelving pulses - are applied, the detection laser is activated for $t_{\mathrm{Det}} = 400\,\mu\mathrm{s}$. During this time, the population in the bright state leads to scattered photons, that can be detected with the imaging system (c.f. section 2.6), while the population in the dark state leads to almost no photons being scattered.

There are two more transitions labeled "E" and "F" in figure 2.2, which are of interest under certain conditions. Transition "E" has a frequency of $f_E \approx 1240.19\,\mathrm{MHz}$, which is only approximately

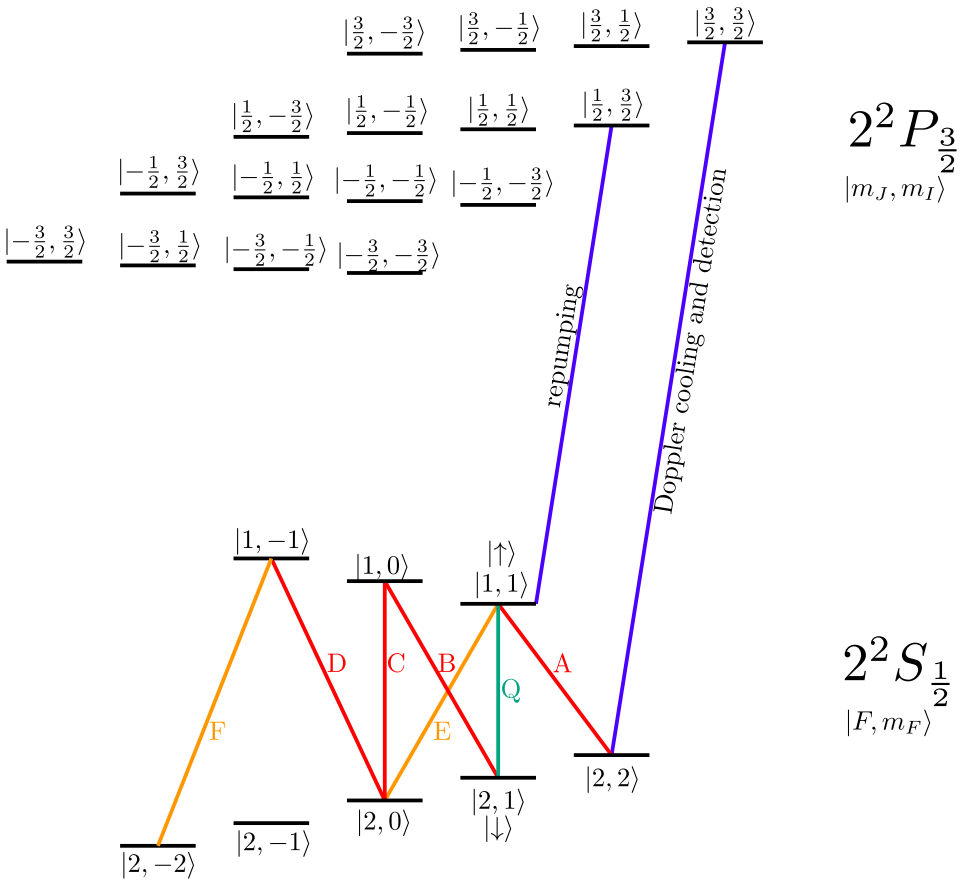

Figure 2.2: Electronic energy structure for $^9Be^+$. Only the $2^2S_{\frac{1}{2}}$ and the $2^2P_{\frac{3}{2}}$ states are shown. Microwave driven hyperfine transitions within the ground state manifold are labeled with letters. A, B, C, D: shelving transitions. Q: qubit transition. E, F; other microwave transitions of interest. Laser-driven transitions are indicated by blue lines between a hyperfine level of the ground state and the excited state.

267 kHz detuned from transition "B". Because of the Fourier-limit of the short microwave pulses on the order of 5 µs, the pulses have a full width at half maximum (FWHW) of around 200 kHz, which means that a pulse driving transition "B" will also have a chance of driving transition "E". If one does not pay attention when choosing a pulse sequence, accidental simultaneous driving of transitions "B" and "E" could lead to an error during the measurements. This should always be kept in mind when developing new pulse sequences.

Transition "F" has the highest frequency in the $2^2S_{\frac{1}{2}}$ ground state manifold with $f_F \approx 1764.46\,\text{MHz}$. In terms of magnetic-field sensitivity, this transition is the counterpart to the field-independent transition "Q". The sensitivity is the highest of all dipole-allowed transitions in the ground state manifold with $\frac{\partial f_F}{\partial B}\Big|_{B_0} \approx 24.6\,\frac{\text{Hz}}{\text{nT}}$[1]. Since the probability of being excited by the detection laser is higher than

1 For comparison, the first-order magnetic-field dependence of the transition frequency for the labeled transitions is: A: $-14.0\,\frac{\text{Hz}}{\text{nT}}$, B: $6.3\,\frac{\text{Hz}}{\text{nT}}$, C: $12.5\,\frac{\text{Hz}}{\text{nT}}$, D: $16.8\,\frac{\text{Hz}}{\text{nT}}$, E: $6.3\,\frac{\text{Hz}}{\text{nT}}$, F: $24.6\,\frac{\text{Hz}}{\text{nT}}$, Q: $0.0\,\frac{\text{Hz}}{\text{nT}}$

for the state $|1,-1\rangle$ [44] and the transition frequency lies practically outside of the frequency range that can be generated by our hardware, populating the state $|2,-2\rangle$ is difficult and has no other use than as a potential magnetic field sensor in the future.

The last labeled transition in figure 2.2 is the repumping transition between the states $2^2S_{\frac{1}{2}}\,|1,1\rangle$ and $2^2P_{\frac{3}{2}}\,|\frac{1}{2},\frac{3}{2}\rangle$, which is driven by a laser beam with a wavelength of around 313 nm, 1268 MHz red detuned with respect to the detection laser. The repumper laser will not only be used in the near future for sideband cooling (c.f. [44]), but also already during state preparation. During Doppler cooling it can happen, due to imperfect polarization of the laser beam, that a part of the population leaves the closed-cycle transition and decays to one of the $|F=1\rangle$ states, where the probability to be excited by the cooling laser is quite low compared to the $|F=2\rangle$ states. Here the repumper laser helps to depopulate the $|F=1\rangle$ states (c.f section 4.1.1).

2.2 Ion trap

To be able to manipulate single Beryllium ions, they must be isolated from environmental influences by trapping them inside a vacuum chamber. The Earnshaw theorem [45] states that a charged particle can never be trapped by purely static electric fields. This can easily be checked by looking at Laplace's equation, which must be fulfilled for an electrostatic field Φ.

$$\vec{\nabla}^2\Phi = \left(\partial_x^2 + \partial_y^2 + \partial_z^2\right)\Phi = 0 \tag{2.1}$$

To have a confining character for a positively charged ion along one direction, the curvature of Φ must be positive in that direction. To fulfill equation 2.1, the curvature - which is the second derivative - must be negative in at least one direction meaning that the potential is repelling.

Two prominent solutions to this problem are the Penning trap [46], where electrostatic fields are combined with static magnetic fields, and the Paul trap [47], where static and time-varying electric fields are combined. Since Paul traps of different kinds are commonly used in quantum computation and quantum simulation experiments, those will be discussed here. The full dynamics of the ion's motion in a Paul trap can be described by a system of Mathieu equations and is discussed in [48]. For most cases, the pseudo-potential-approach [49] is sufficient to explain the radial motional frequencies of an ion in a Paul trap. Since the ion is a charged particle, it feels a time-dependent force

$$\vec{F}(t) = q\vec{E}_0(x,y)\cos(\omega_{\mathrm{RF}}t) \tag{2.2}$$

where q is the electric charge of the ion, $\vec{E}_0$ the amplitude of the driving quadrupole field in the xy-plane and $\omega_{\mathrm{RF}} = 2\pi f_{\mathrm{RF}}$ the angular frequency of the driving field. The velocity $\vec{v}$ of the ion

with mass m can then be calculated using classical mechanics by

$$\vec{v}(t) = \frac{1}{m}\int_0^t \vec{F}(\tau)\mathrm{d}\tau = \frac{q\vec{E}_0(x,y)}{m\omega_{\mathrm{RF}}}\sin(\omega_{\mathrm{RF}}t). \tag{2.3}$$

The average kinetic energy over one period can be seen as a pseudopotential V_{PP} and is given by

$$V_{\mathrm{PP}} := \langle E_{\mathrm{kin}}\rangle = \frac{m}{2}\langle\vec{v}^2\rangle = \frac{q^2\vec{E}_0^2(x,y)}{4m\omega_{\mathrm{RF}}^2} \tag{2.4}$$

When we now expand $\vec{E}_0(x,y)$ around its minimum at (0,0) we obtain

$$\vec{E}_0(x,y) = \left(\partial_x\vec{E}_0(0,0)\right)x\vec{e}_x + \left(\partial_y\vec{E}_0(0,0)\right)y\vec{e}_y =: E_{0x}^{'}x\vec{e}_x + E_{0y}^{'}y\vec{e}_y \tag{2.5}$$

where $\vec{e}_x$ and $\vec{e}_y$ are the unit vectors in x and y direction. Now we can insert equation 2.5 into equation 2.4 and rewrite it to obtain the form of a two-dimensional harmonic oscillator with the radial angular trap-frequencies ω_x and ω_y.

$$V_{\mathrm{PP}} = \frac{m}{2}\left(\frac{q^2E_{0x}^{'2}}{2m^2\omega_{\mathrm{RF}}^2}\right)x^2 + \frac{m}{2}\left(\frac{q^2E_{0y}^{'2}}{2m^2\omega_{\mathrm{RF}}^2}\right)y^2 =: \frac{m}{2}\omega_x^2x^2 + \frac{m}{2}\omega_y^2y^2 \tag{2.6}$$

The electrostatic field in the Paul trap causes a potential that is superimposed on top of the radial trapping potential. This potential has to be confining in the z-direction to ensure three-dimensional confinement of the ions. Due to equation 2.1, this static potential must be repelling in at least one of the other direction. Depending on the specific circumstances, the static potential can be repelling either in the x and y direction or it can be confining in one of these directions and be repelling in the other. A confining static potential in one direction would increase the trap frequency in this direction while a repelling potential would decrease it. This usually results in an overall trapping potential that leads to three different trap frequencies $f_x = \omega_x/2\pi$, $f_y = \omega_y/2\pi$ and $f_z = \omega_z/2\pi$.

When there is more than one ion in the trapping potential, the repulsion between the ions caused by the Coulomb force results in the formation of a Coulomb crystal in which each ion has a distinct equilibrium position. The motion of the ions with respect to their equilibrium position can then be described by $3n$ normal modes [50], where n is the number of ions in the trapping potential.

In the following, we will consider a single ion in the trapping potential for simplicity. The considerations can be extended to multiple ions, which would increase the total number of modes. The motion of an ion with the trap frequencies f_x, f_y and f_z and its micromotion with $f_{\mathrm{RF}} = \omega_{\mathrm{RF}}/2\pi$

causes sidebands on the electronic energy structure of the ion which are qualitatively shown in figure 2.3. The ion's motion in the trap is quantized and produces additional energy levels around the electronic levels in Beryllium. When we only look at the oscillation in one direction, we can describe the Beryllium ion as a two-level system coupled with a harmonic oscillator, which results in energy levels as shown in figure 2.4. The motional frequencies f_x, f_y and f_z are not to be confused with the micromotion frequency f_{RF}.

The internal and motional states of the ion are coupled via sideband transitions, which deterministically add or remove one quantum of motion. Applying a resonant driving field at frequency f_Q induces Rabi-oscillations between $|\downarrow, n\rangle$ and $|\uparrow, n\rangle$, where n is the motional quantum number of a specific mode. This carrier transition does not affect the motion of the ion, but only its internal state. The red and blue motional sideband transitions are detuned from the carrier by the trap frequency, e.g. f_x. In the case of a red sideband the transition $|\downarrow, n\rangle \leftrightarrow |\uparrow, n-1\rangle$ is coherently excited. The counterpart is a blue sideband transition, where $|\downarrow, n\rangle \leftrightarrow |\uparrow, n+1\rangle$ is coherently excited.

Sideband pulses together with a suitable repumping scheme can be used to cool the ion's motion below the Doppler cooling limit by gradually removing motional quanta [51]. This technique can be utilized to prepare the ion in the motional ground state. Several quantum logic operations require the system to be initially in the motional ground state, such as quantum logic spectroscopy [52] or quantum logic gates [7]. Although being in the motional ground state is not a prerequisite for the Mølmer-Sørensen gate [53], which we plan to implement in our trap as an entangling two-qubit gate, it relies on motional sideband transitions to utilize the shared motion of the ions in the trap as a quantum information bus. Our group has already demonstrated this gate in a room-temperature trap [22] similar to the one used in the experiment described in this thesis.

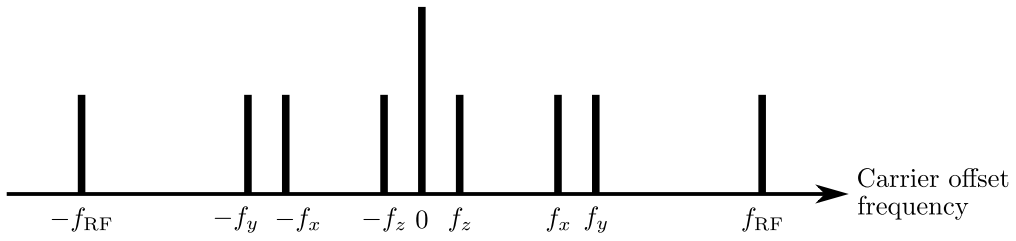

Figure 2.3: Sideband spectrum around a carrier transition for a single trapped ion. Typical values for the experiment described in this thesis are $f_z = 1\,\mathrm{MHz}$, $f_x = 10.85\,\mathrm{MHz}$, $f_y = 11.31\,\mathrm{MHz}$, $f_{\mathrm{RF}} = 99.38\,\mathrm{MHz}$. The directions are arbitrarily set so that the motional frequency in the y-direction is the highest.

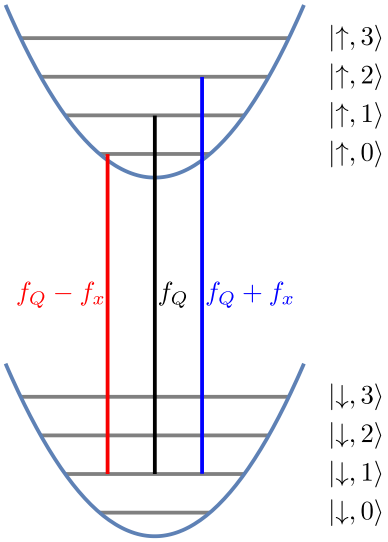

Figure 2.4: Energy levels for sideband transitions. A red and blue sideband transition drive a spin flip and simultaneously change the motional quantum number by one in a deterministic way.

2.2.1 Cryogenic Surface-electrode Paul trap

Several realizations of the linear Paul trap have evolved in the past years. The most prominent ones are the four-rod geometry, where the ions are trapped between the electrodes, and the surface-electrode Paul traps, where the ions are trapped above the electrodes of a trap chip (see figure 2.5). Other geometries are also used which combine elements of both approaches [54]. The chip-based surface-electrode architecture promises high scalability towards a high number of qubits, especially when the trap structure is extended into two dimensions [24]. Furthermore, additional electrodes can be integrated in the trap structure [20], which can then be used to manipulate the ions with microwave radiation instead of laser beams.

Our group developed and produced the surface-electrode ion trap that was used for the measurements presented in this thesis. A CAD-illustration of the trap is shown in figure 2.6. The trap has the usual RF and DC electrodes that generate the trapping potential and also three additional microwave electrodes which can be used to manipulate the internal and the motional state of the ions. When sending a microwave current through one of the outer two microwave electrodes "MWC", the resulting oscillating magnetic field at the ions' position can drive carrier transitions in the ions. The center meander-like shaped electrode "MWM" is specially designed to produce an oscillating magnetic field gradient with very low field amplitude at the ions' position [43], which is required to drive sideband transitions with the microwave near-field approach [20].

The trap is operated at a cryogenic temperature of around 5 K, which promises several benefits. First of all, the conductivity of nearly all materials is significantly better at cryogenic temperatures

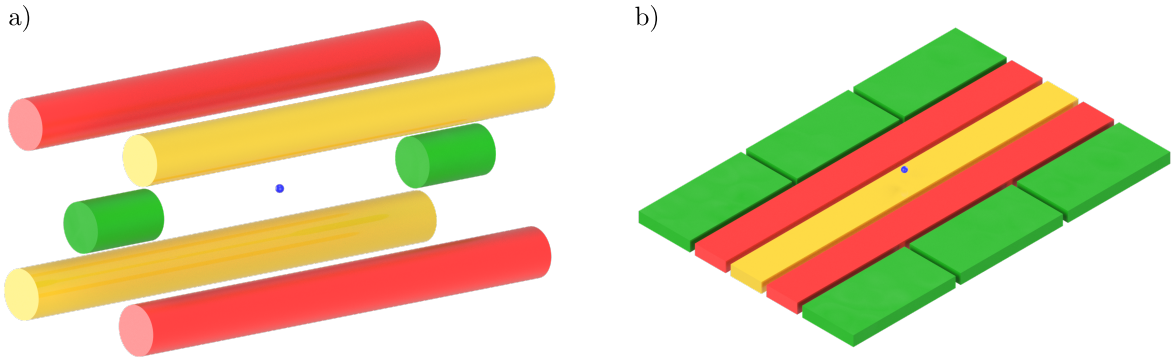

Figure 2.5: CAD view of different ion trap geometries. a) Four-rod ion trap, b) surface-electrode ion trap. The functionalities of the electrodes are color-coded. Red: RF electrode, green: DC electrode, yellow: ground. The position of the trapping potential minimum is indicated with an exaggerated blue ion.

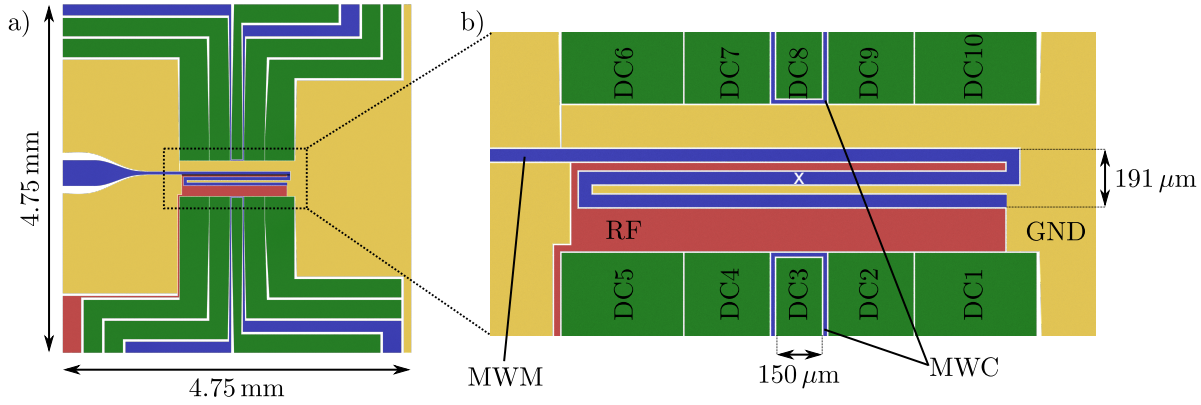

Figure 2.6: Schematic view of the surface-electrode ion trap. a) Full chip with feed lines. The electrodes are color-coded by their functionality. Red: RF electrode, green: DC electrode, yellow: ground, blue: microwave electrode. b) Center of the chip. The "x" in the middle indicates the trap center.

than at room temperature. This leads to lower resistive losses in the trap, which can be beneficial when using high power microwave currents like in this experiment. Also the Q-factor of the resonator used for impedance matching of the 50 Ω RF-source to the mainly capacitive trap electrode increases at lower temperatures [55].

The second benefit is the reduced heating rate of the ions due to the so-called anomalous motional heating. The origin of this effect is not completely understood, but it has been shown in other experiments that the heating rate depends on the trap temperature as well as the ion-electrode distance and the trap frequency [36]. Motional heating is reduced for a lower temperature of the trap, a higher trap frequency and a larger ion-electrode distance. For the microwave-nearfield approach pursued in our group, a small ion-electrode distance is needed to generate the required field gradients. Since low heating rates are desired for high fidelity two-qubit gates, we aim for a

low trap temperature.

The third benefit of a cryogenic ion trap is the excellent vacuum which leads to almost infinite ion lifetimes in the trap compared to room-temperature traps with an average lifetime on the order of a few tens of minutes. For the measurements presented here, this allowed to measure for many hours without worrying to lose an ion. In the future, when a quantum simulator or small quantum computer runs with dozens of ions, a high ion lifetime is mandatory to prevent frequent re-loading of the trap.

2.2.2 Filter board

The previously described surface-electrode ion trap is wire-bonded to an interfacing board that hosts the connectors for the trap voltages and the microwave currents. This board also features a first-order RC low-pass filter for each DC electrode, hence the name "filter board". A picture of the board with the ion trap is shown in figure 2.7. The resistors of the RC-filters are mounted on the side of the board shown in the picture, while the capacitors are mounted on the backside.

Not only would noise on the DC voltages disturb the ions' motion in the trap, but also electric fields from the environment caused by stray charges on dielectric surfaces for example. To protect the ions as much as possible from those stray charges, a shielding structure, called Faraday cage, is installed around the ion trap and is electrically connected to the ground plane of the filter board.

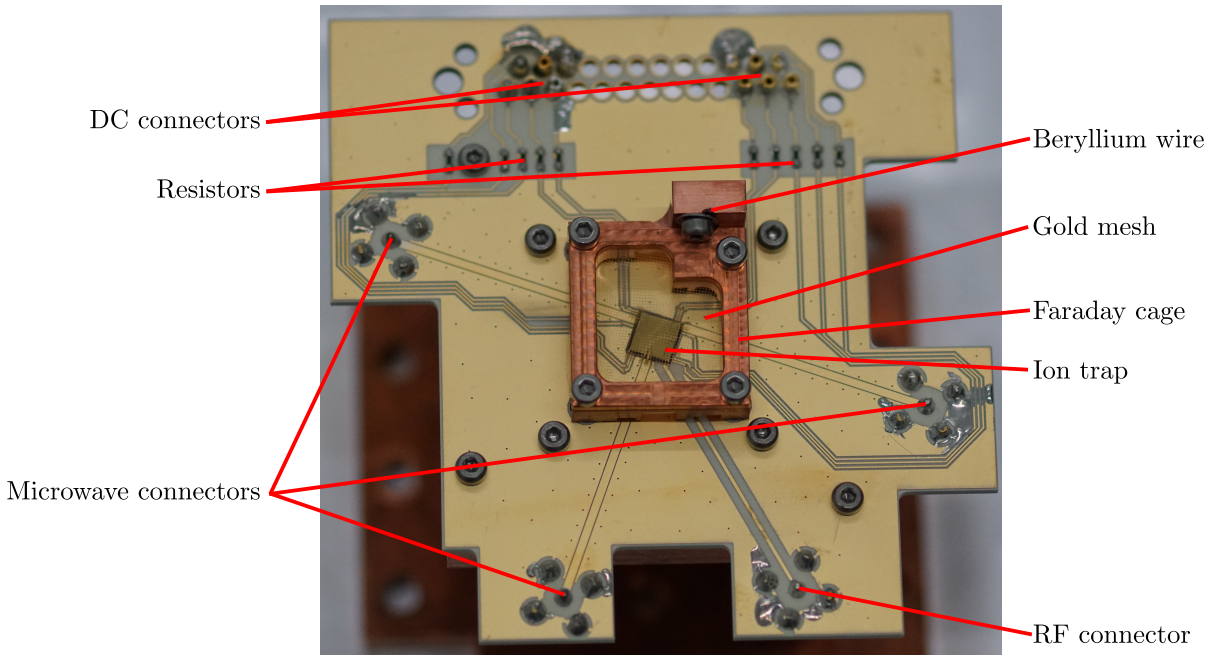

Figure 2.7: Picture of the filterboard with Faraday cage.

The outer frame of the cage is made of copper and also hosts a Beryllium wire that is used as a source of Beryllium atoms. It has gaps at the positions needed for laser access of the trap and a groove between the Beryllium wire and the trap center. The direction perpendicular to the trap surface is used to image the fluorescence light of the ions, therefore the Faraday cage "lid" is not made out of a solid metal surface, but consists of a grounded gold mesh (Precision Eforming MG17). The filter board also features a D-sub connector for the DC voltages and MCX connectors for the microwave currents and the RF voltage.

2.3 Apparatus

In order to achieve a trap temperature of 5 K, a sophisticated design was developed and described in great detail in [56], see figure 2.8 for a simplified view. The cold head used to reach cryogenic temperatures has two cooling stages, the first at around 50 K and the second stage is held at 5 K by a regulator. The available cooling power is around 1.5 W for the second cooling stage and in the range of some tens of watts for the first cooling stage. The cold head has to work against the heat load originating from thermal radiation and from heat conduction through cables. Conductive heat load from air is ruled out by pumping the outer vacuum chamber to a pressure in the low 10^{-8} mbar range. The materials used for the cables were chosen carefully to keep the heat load on the cooling states low. We made an effort to dump as much of the unavoidable remaining heat load as possible into the first cooling stage to relieve the second cooling stage.

For the radiative part, this was achieved by placing a hollow copper cylinder called "radiation shield" between the outer and the inner vacuum chamber and by mounting it to the first cooling stage. From the Stefan-Boltzmann law, we know that the radiated power scales with the fourth power of the absolute temperature. Therefore the radiative heat load between the radiation shield at 50 K and the inner vacuum chamber at 5 K is several orders of magnitude lower than the heat load due to blackbody radiation from the outer vacuum chamber at room temperature would be without the radiation shield. There are some holes in the radiation shield that are needed for optical access, but the heat load introduced by these holes is only in the milliwatt range. To reduce the amount of conductive heat load on the second cooling stage we mounted the cables to the first cooling stage in such a way that a large contact area is obtained. Most of the heat load will then be dumped into the first cooling stage and only a relatively small part of the heat load will affect the second cooling stage. An additional source of heat is present when currents flow through the cables due to resistive losses. For the wires carrying the DC trap voltages, this heat load is negligible since only very small currents are flowing while the trap voltages are changing. For the RF trap drive, resistive losses lead to approximately 200 mW of additional permanent heat load that are distributed on both cooling states. The heat load due to microwave pulses is dynamic and we measured that up to

4.0(1.0) W of microwave power at around 1 GHz could be applied continuously without exceeding the cooling power of the second cooling stage.

2.3.1 Vibration isolation

A main feature of this apparatus is the vibration isolation interface that allows to reach record low vibration amplitudes of the 5 K cold inner vacuum chamber relative to the optical table [57]. When properly aligned, the residual vibrations can go down to approximately 10 nm RMS. Low vibration levels are required for the future use of Raman-lasers and are also highly beneficial for a sharp image of the ions on the EMCCD camera.

The interface relies on gaseous helium to conduct heat while damping vibrations. The cold head has no mechanical connection to the outer (and inner) vacuum chamber but a rubber bellow between these two, that prevents the helium from escaping. The helium in the vibration isolation interface has a pressure of around 30 mbar above the air pressure in the lab. It is intuitively clear and was experimentally verified that the temperature of the Helium in the vibration isolation interface must be higher than its boiling point at 4.2 K to ensure proper vibration decoupling. We therefore operate the second cooling stage at a temperature of 5 K to have a safety margin to the helium becoming liquid and transmitting vibrations.

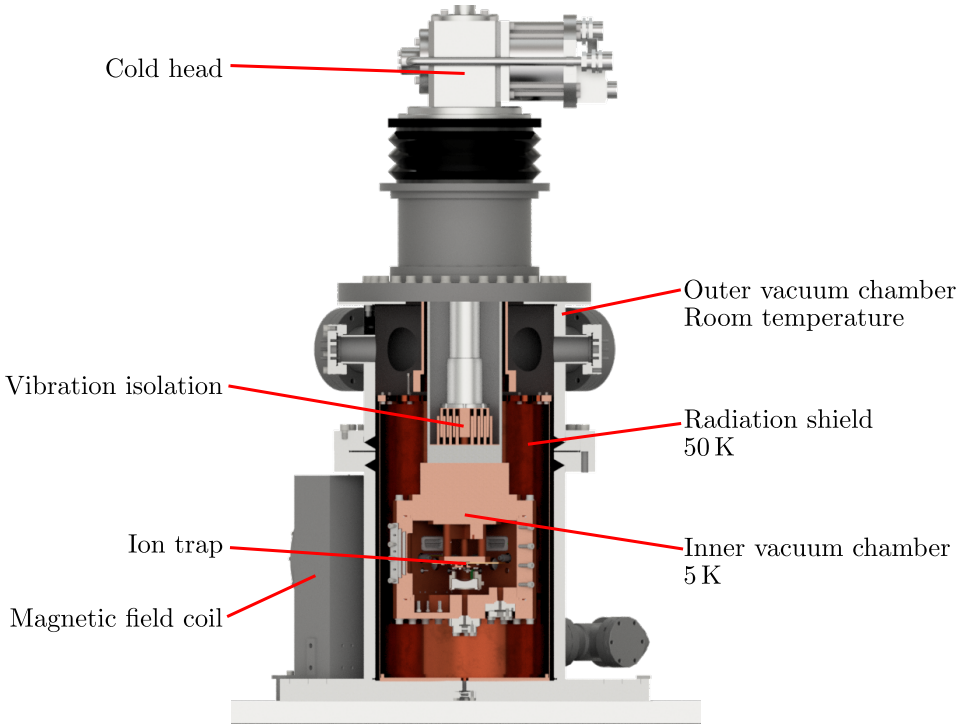

Figure 2.8: Cut view of the vacuum chamber with the different temperature stages. A second magnetic field coil would be located on the right side and is not shown here.

The vibration isolation interface consists of concentric copper rings at the side of the cold head and also at the side of our vacuum chamber. These rings must be aligned with below millimeter precision to prevent them from touching and therefore transmitting vibrations. The alignment can be done by maximizing the inductance between cold head and vacuum chamber or with the help of the interferometer described in section 2.5.5.

The cold head is placed in a supporting structure that can be used to align all necessary degrees of freedom and is mounted to the lab's ceiling. The vacuum chamber is mounted to an optical table that is floating on pressurized air and makes use of positioning control valves that have an accuracy of 0.3 mm to reach the initial position. With this precision, we do not have to realign the cold head after putting heavy objects onto or removing them from the optical table. The situation is different when the optical table lost the pressurized air entirely. In this case, it is not guaranteed that the original position is reached by relying on the valves alone when the pressurized air is reapplied. In such a case, the transport securing devices must the reinstalled before reconnecting the pressurized air in order to prevent possible damage to the cold head or the vibration isolation interface.

The pressurized air for our lab is produced by a compressor in the institute's basement and has occasional malfunctions. Since the supply of pressurized air from this device can be interrupted and restored in principle at any time, we built an interlock circuit based on an Arduino microcontroller that prevents restoring the pressurized air supply to the optical tables after it was interrupted. Losing and restoring the pressurized air for the optical tables also has an influence on the alignment of our laser systems. To reduce the time spent on realigning the laser systems, the interlock system is programmed in a way that it will switch the supply of the optical tables to a cylinder of nitrogen in case the pressurized air supply is interrupted. In this state, the pressure in a nitrogen cylinder with a volume of 50 liters is reduced by approximately 10 bar per day. When the pressurized air supply is restored, the interlock circuit requires manual input to switch back to that source.

2.4 Electronics

The precise control of the applied voltages and currents to the trap is crucial for stable trapping potentials and the realisation of high fidelity operations. In the following, we will briefly present the experiment control system and describe the generation of necessary electrical signals and the magnetic field. A more detailed discussion can be found in [56].

2.4.1 Experiment control system

The experiment control system used for the experiments presented in this thesis was developed by Christopher Langer [58] and was later modified to be able to run under Windows 7 [59]. The system uses a field programmable gate array (FPGA) that coordinates the real-time communication between the computer and the hardware inputs and outputs. The system features 16 digital output ports, up to 32 analog DDS outputs and two digital inputs to count the signals detected by a PMT. The FPGA runs at a clock frequency of 62.5 MHz, which corresponds to a time resolution of 16 ns for the digital signals. The DDS modules run on a 1 GHz reference frequency allowing them to generate high-frequency signals up to 500 MHz.

The software used to operate the experiment control system is called "hfGui 3" and supports a python based scripting language. It can also be used to program the waveform generators described in section 2.4.2. The experiment control system is usually used to run a script a specific amount of times while scanning a variable, e.g. a frequency or a pulse length. When the experiment has finished, a fit can be applied to the measured data points and the fit parameters can be saved into so-called "ion properties", which can later be used by other scripts.

2.4.2 DC voltages

10 low-noise DC-voltages are used to generate the axial trapping potential. To move the trapped ions around above the trap surface, it is important to precisely control the voltages at any time during the transport. In our experiment, we use FPGA-controlled arbitrary waveform generators, which are presented in [60]. These modules can output voltages between $-10\,\mathrm{V}$ and $+10\,\mathrm{V}$ with an update rate of 50 MHz and a resolution of 16 bit, corresponding to a step size of approximately $300\,\mu\mathrm{V}$. Before the voltages are applied to the trap electrodes, they pass two low-pass filter stages. The first filter stage consists of a Mini-Circuits "LPF-B0R3+" for each voltage channel and is located in an aluminium box (called "filter box") attached directly to the vacuum feedthrough. This filter features a steep cutoff in its transfer function starting at 300 kHz. The second filter stage consists of a first-order RC-filter with a 3dB-cutoff-frequency of approximately 200 kHz close to the ion trap. Both filter stages together reduce the electronic noise at the trap frequencies in the MHz range and therefore lead to reduced motional heating.

All trap voltages are referenced to a common ground potential. A good quality ground connection is at least as important as well-filtered DC voltages. In the early stages of operating our experiment, we used a thin copper wire between the DC feedthrough in the outer vacuum chamber and the inner vacuum chamber to deliver electrical ground to the filterboard and the trap. Contrary to the usual approach in electronics to use wires with a large cross section for grounding purposes, the copper wire had to be thin for our application to keep the heat load due to heat conduction on the

cooling stages low. Note that the wires used for the DC voltages are made of constantan which has a low heat conductivity compared to copper, but comes with a higher electrical resistance. Later it turned out that the ground connection with the thin copper wire has a resistance of approximately $0.1\,\Omega$, which is quite high for a ground connection. We have now connected the ground wire of the filter box directly to the outer vacuum chamber that has a conductive path towards the inner vacuum chamber and the filter board. The resistance of this connection is so low that the exact value is hard to determine, but we estimated it to be at least one order of magnitude lower than when using the thin copper wire for the ground connection.

The filter box also features a so-called "tickle"-input. A high-frequency signal applied to this input bypasses the first low-pass filter of DC electrode 2 (c.f. figure 2.6 b)) using an RF-transformer and a capacitor as a bias tee. When a frequency identical to one of the ions' motional frequencies is applied, the motional state of the ions is excited and leads to a drop in fluorescence due to the Doppler effect. This method can be used to determine the trap frequencies of the ions.

2.4.3 RF voltage

For radial confinement of the ions in the trap, a high-frequency electric field is required. Amplitudes on the order of 100 V are needed to operate the trap. To generate this high voltage amplitude, a cryogenic helical resonator is used for impedance matching of the $50\,\Omega$ source impedance to the mostly capacitive load impedance, which is the trap's RF electrode and its feed line. The RF signal with a frequency of $f_{\mathrm{rf}} = 99.380\,\mathrm{MHz}$ is generated by an HP 8640 signal generator and amplified to approximately 24 dBm. This RF power is sent into the resonator and leads to radial trap frequencies of 10.85 MHz and 11.31 MHz. The driving frequency f_{rf} is fine-tuned relative to the resonator's resonance frequency by adjusting f_{rf} so that the radial trap frequencies are maximized. The angular radial trap frequencies ω_{r_i} depend on both the RF gradient E_i' in the direction of the radial mode and the angular frequency of the RF trap drive $\omega_{\mathrm{rf}} = 2\pi f_{\mathrm{rf}}$:

$$\omega_{r_i} = \frac{qE_i'}{\sqrt{2}m\omega_{\mathrm{rf}}}. \tag{2.7}$$

Here, q is the elementary charge and m the mass of a $^9\mathrm{Be}^+$ ion. The electric field gradient scales linearly with the applied voltage, which itself scales with the square root of the RF power, since $P_{\mathrm{rf}} = \eta \cdot U_{\mathrm{rf}}^2/Z$, where Z is the complex impedance of the trap's RF electrode and η is a loss factor that takes into account that not the whole power applied to the resonator will reach the trap. We obtain the relationship

$$\omega_r \propto E' \propto U_{\mathrm{rf}} \propto \sqrt{P_{\mathrm{rf}}}. \tag{2.8}$$

We can investigate the influence of a drifting RF power on the angular radial trap frequencies by calculating the derivative of ω_r with respect to P_{rf}. For reasons of clarity we use a single constant C to represent the proportionality.

$$\omega_r = C \cdot \sqrt{P_{\mathrm{rf}}} \tag{2.9}$$

$$\frac{\mathrm{d}\omega_r}{\mathrm{d}P_{\mathrm{rf}}} = \frac{C}{2\sqrt{P_{\mathrm{rf}}}} \tag{2.10}$$

Now we can use the Taylor expansion around the operation point P_0 and stop after the first order:

$$\begin{aligned} \omega_r &= C \cdot \sqrt{P_0} + \frac{C}{2\sqrt{P_0}} \cdot \Delta P + ... \\ \omega_r &\approx \omega_{r_0} \cdot \left(1 + \frac{1}{2}\frac{\Delta P}{P_0}\right) \end{aligned} \tag{2.11}$$

Here ω_{r_0} is the angular radial mode frequency at the operating point P_0 and ΔP is the deviation from P_0. Assuming a Fourier-limited linewidth of the radial modes and a microwave pulse duration of 1 ms to drive a sideband transition, the radial mode stability has to be better than 1 kHz or 0.01 %, which means that the RF power must have a stability better than 0.02 %. To achieve such high RF power stability we use the RF rectifier presented in [61] together with a temperature stabilized RF amplifier (API technologies BX3110).

The trap frequency does not only depend on the applied voltage, but also on the trap geometry, which can slightly change with temperature. The microwave sideband pulses have a peak power of around 10 W, which heat up the trap. We investigated the effect of microwave heat load on the radial trap frequencies and found an effect in the kilohertz range that depends on the average microwave power applied to the trap. When the duty cycle of the high power microwave drive was kept constant at around 5 %, we could not observe different radial mode shifts depending on the pulse duration.

2.4.4 Microwave currents

At a magnetic field of 22.3 mT, the transition frequencies between two hyperfine states of the $S_{1/2}$ ground state of $^9Be^+$ are in the microwave range around 1 GHz. Our experiment control system uses DDS modules based on the AD9858 chip to generate frequencies up to 500 MHz, which are doubled in frequency twice to reach the required frequency range needed to drive the transitions in $^9Be^+$. The hardware used to generate the microwave frequencies is discussed in more detail in [56, 59, 62].

To drive carrier transitions which just change the internal state of an ion, an oscillating magnetic field at the transition frequency is used. The trap chip features two dedicated electrodes for this purpose for symmetry reasons (see figure 2.6), but one carrier electrode is sufficient to operate the trap. The second carrier electrode is not connected to the outside world because of a bad contact somewhere in the feed line. The microwave power level needed to achieve π-times on the order of microseconds for a carrier transitions on the field-independent qubit is around 250 mW, which can be obtained with a relatively small amplifier (Mini-Circuits ZRL-1150LN+).

Sideband transitions, which simultaneously change the internal and the motional state of an ion in a deterministic way, are driven with an oscillating magnetic field gradient at the sideband transition frequency [20]. The microwave power needed to drive sideband transitions is much higher than for carrier transitions, so that we end up with on the order of 10 Watts to reach π-times in the millisecond range. When two microwave currents of different frequencies are applied simultaneously, it is possible to implement the Mølmer-Sørensen-interaction [53], that can be used for entangling two-qubit gates. To generate a magnetic-field configuration with an oscillating gradient and suppressed amplitude at the ion's position, a meander-shaped electrode is used [63].

The end of the meander electrode is grounded, which leads to the microwave power being reflected back and to an effective doubling of the current amplitude while almost nulling the voltage amplitude. Since a small, but finite, amount of voltage drop over the meander electrode is present and therefore produces an electric field gradient above the trap surface, applying a microwave current does have an effect on the ions' motion. If the microwave current is switched on or off abruptly, the ions' motion is excited by the resulting high-bandwidth electric field pulse.

To prevent this, a simpler form of the pulse shaping technique in [44] is used. We program an arbitrary waveform generator, the same kind as used for the DC trap voltages, to produce a pulse shape $p(t)$, that increases smoothly from 0 V to 10 V following an erf-function, then stays constant, and decreases smoothly from 10 V to 0 V following an inverted erf-function.

$$p(t) = \begin{cases} \frac{10}{2}(1 + \mathrm{Erf}(2.25(t-1))) & ,0 < t \leq 2 \\ 10 & ,2 < t \leq t_p \\ 10 - \frac{10}{2}(1 + \mathrm{Erf}(2.25(t-1-t_p))) & ,t_p < t \leq t_p + 2 \\ 0 & ,\text{else} \end{cases} \tag{2.12}$$

The erf-part in the waveform is 2 µs long, the flat part of the pulse shape ends at t_p, the unit of $p(t)$ is Volt and the unit of t is microseconds. The waveform generator is fed with the voltage of a waveform and its derivatives at certain points in time. An FPGA then takes care of interpolating between those discrete points in a smooth way using splines. For the erf-like parts of the waveform used here, the step size is 200 ns.

An analog multiplication circuit based on the ADL5391 chip [62] is used to multiply the envelope $p(t)$ with a microwave signal $m(t) = U_0 \sin(2\pi f t)$ of frequency f and amplitude U_0. Before the signal $p(t)$ is applied to the analog multiplier's input, it is send through a 1:10 voltage divider to reduce the voltage to an allowed level while maintaining the resolution of the generator. The shaped output signal $s(t)$ of the analog multiplier is then simply $s(t) = \frac{1}{10\,\mathrm{V}} p(t) \cdot m(t)$ (see figure 2.9). Currently there is no active feedback loop installed to stabilize the microwave pulse envelope like in [44].

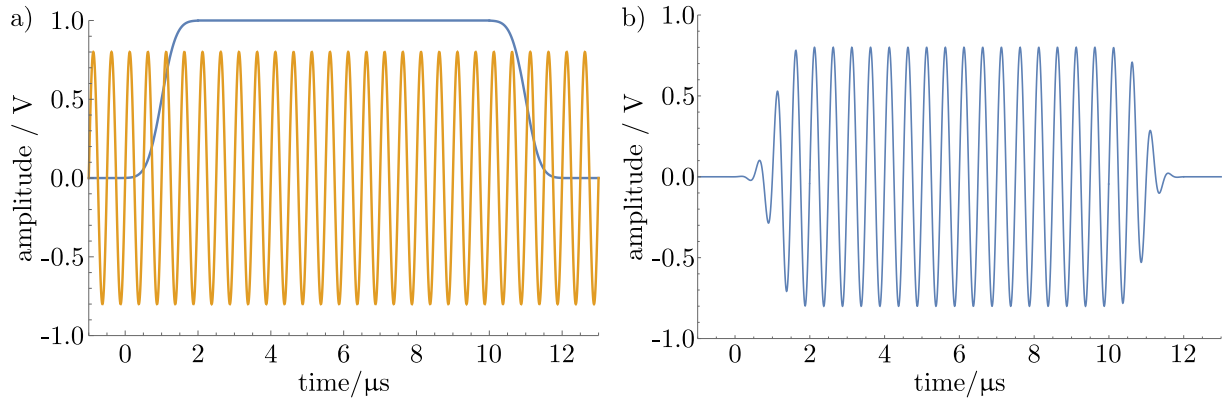

Figure 2.9: Working principle of the pulse shaper. a) The two input signals are the microwave signal (orange) and the envelope signal (blue). b) Shaped pulse. For clarity the frequency of the microwave signal is reduced to 2 MHz.

Because the Mølmer-Sørensen gate requires the simultaneous application of a red and blue sideband, we operate two of the described pulse shaping circuits. After the red and blue sideband pulses have been shaped, they are amplified individually by two cascaded amplifiers (Mini-Circuits ZX60-P-162LN+ and RFHIC RWP15040-H1). Fixed attenuators are used to maintain an allowed input power level. After both sideband pulses were amplified to approximately 50 W, they are each sent through a directional coupler (MECA Electronics 780-20-1.250) to sample 1 % of the pulse power for monitoring purposes and future upgrades towards active envelope stabilization. Afterwards, both sideband pulses are combined in a hybrid coupler (AtlanTecRF AH180-007501500), before the combined pulse is sent to a circulator (Cernex Inc. COCU8010323G1-01) and then towards the trap. The circulator guides the backreflected power from the trap into a termination resistor to prevent standing waves on the cable and damage to the amplifier. After passing all the mentioned components, around 10 Watts of microwave power remain per sideband.

2.4.5 Magnetic field coils

Besides a well-filtered and shielded electrical environment, a stable external magnetic field is also required to achieve a high quality of the performed qubit operations. The external magnetic field at the ions' position defines the quantization axis and shifts the energy levels of the hyperfine states. While the qubit transition itself is insensitive to magnetic field fluctuations to first order at the

chosen field of $B_0 \approx 22.3\,\mathrm{mT}$, the other transitions required for state preparation and shelving change their frequency when the magnetic field changes.

The development process of a set of two magnetic field coils is described in [56]. Since the used copper wire with a diameter of 2.112 mm was pretty hard to handle during winding the coils, we did not manage to produce two perfectly equal coils. In the first coil we managed to wind 24 layers of copper wire and for the second coil only 23 layers could be fitted in the coil's housing. Also each layer has between 26 and 29 windings in both coils. In total over 570 meters of copper wire were used for the magnetic field coils.

Even if the differences between the two coils might sound alarming when looking at the raw numbers, simulations of the magnetic field produced by those different coils looked promising and were later confirmed by measurements with a hall probe. According to the simulations, the local minimum of the magnetic field is shifted by approximately 1 mm towards the coil with 23 layers. We tried to position the two coils as good as possible around the vacuum chamber and did not find any problems with the ions probably not being located at the local magnetic field minimum until now. Note that it would also be very challenging with two perfectly equal coils to get the position right within 1 mm.

The coils are connected in series and are powered by two power supplies in constant current mode (Delta Elektronika SM 70-45 D) that are also connected in series and can deliver up to 70 V and 45 A each. After we trapped the first ions with a coarsely aligned magnetic field, we were able to use an ion as a magnetic field sensor and adjust the coil current to the right value. This was done by scanning the frequency of microwave pulses used to drive the $|2,2\rangle \leftrightarrow |1,1\rangle$ transition and comparing the observed resonance frequency with calculated values for a field of 22.3 mT. We ended up at a current of 37.6 A, which results in a voltage drop of 120.8 V and a power dissipation of around 4.5 kW for both coils combined. The coils are water-cooled to prevent them from melting and a safety circuit is installed that immediately switches off the power supplies when the cooling water flow is below 10 $\frac{\mathrm{L}}{\mathrm{min}}$ per coil or when a sensor detects water on the floor below the coils. With this flow rate, the temperature of the cooling water would increase by approximately 3 Kelvin after it ran through the coils.

To monitor the long-term stability of the magnetic field produced by the coils, we performed a resonance frequency scan of the $|2,0\rangle \leftrightarrow |1,-1\rangle$ transition every 5 minutes over a weekend. For every scan a function of the form

$$f(y_{\min},y_{\max},x,x_0,F_0,t) = y_{\min} + \frac{y_{\max}-y_{\min}}{2} \cdot \left(1 + \frac{\left(\frac{x-x_0}{F_0}\right)^2 + \cos\left(2\pi F_0 t \sqrt{1+\left(\frac{x-x_0}{F_0}\right)^2}\right)}{1+\left(\frac{x-x_0}{F_0}\right)^2} \right) \tag{2.13}$$

is fitted to the datapoints (see figure 2.10 a)). Here $y_{\min}$ and $y_{\max}$ are used to describe amplitude and offset of the function, x is the input variable and describes the microwave frequency at each datapoint, x_0 is the center frequency of the resonance, F_0 is the Rabi-frequency of the driven transition and t is the known length of the microwave pulse and not a fit variable, here $t \approx 7.9\,\mu s$. We determine suitable fit parameters for each of the 783 scans of the resonance frequency, extract the center frequency x_0 and convert it to a magnetic field using the known magnetic field sensitivity of the used transition which is $16.8489\,\frac{kHz}{\mu T}$ around a field of 22.3 mT. The drift of the magnetic field over time is shown in figure 2.10 b). We used a linear fit to determine the average rate of the magnetic field drift to be $35.2(4)\,\frac{nT}{h}$. This drift of the magnetic field generated by our coils is really low compared to the magnetic field generated by permanent magnets that are used in an experiment of our group at PTB that is similar to the one we use in Hannover and has a drift of around $1.7\,\frac{\mu T}{h}$. Such low drift rates allow us to let experimental sequences run for many hours without worrying that the data could be compromised by a drifting magnetic field.

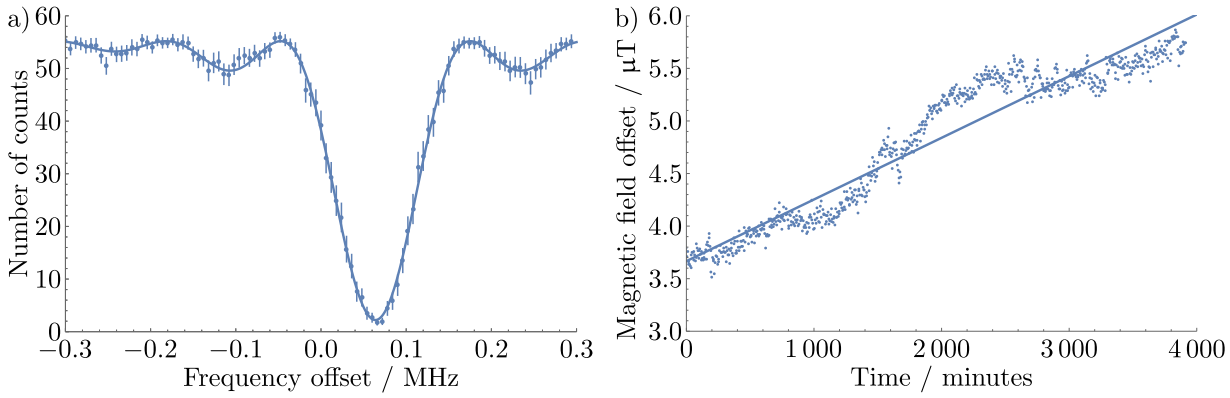

Figure 2.10: Long-term measurement of the magnetic field drift. Points: experimental data, solid line: fit. a) A single scan of the resonance with a fit according to equation 2.13. The error bars indicate the standard deviation. b) Magnetic-field drift over time extracted from 783 measurements of the kind seen in a). The frequency offset is relative to the theoretically calculated transition frequency and the magnetic-field offset is relative to the ideal magnetic field required for the $|2,2\rangle \leftrightarrow |1,1\rangle$ transition to become field independent to first order.

2.5 Laser Systems

While the qubit and shelving operations are carried out purely using microwave pulses, trapping, cooling, state preparation and detection require laser beams. In this section, the different laser systems are presented in the order in which they are used to trap one or more ions. The laser system and its alignment is discussed in greater detail in [56]. A simplified schematic of the laser system is shown in figure 2.12.

2.5.1 Ablation laser

Before the trap can be used to trap Beryllium ions, free Beryllium atoms have to be present close to the trap center. These atoms are generated by firing a focused pulsed laser beam from a "Continuum Minilite 1" onto a Beryllium wire with a pulse energy of around 28 mJ [56] and a wavelength of 1064 nm. The Beryllium wire has a diameter of 0.5 mm and is mounted to the Faraday cage (c.f. section 2.2.2) which has a 1.4 mm wide groove in order to enable Beryllium atoms that are emitted mostly perpendicular from the wire's surface to reach the trap center (see figure 2.11).

2.5.2 Photoionization laser

When a Beryllium atom travels through the trap center, it can be ionized by a resonant two-photon process [64]. The first photon with a wavelength of 235 nm excites the Beryllium atom from the $^1S_0$ ground state to the $^1P_1$ state. A second photon with an energy of $hc/235\,\mathrm{nm}$ can now ionize the excited Beryllium atom. The 235 nm laser light is generated by two frequency doubling stages from 940 nm laser light emitted by an amplified diode laser (TOPTICA TA Pro). To ensure that the photo-ionization laser runs at the correct frequency, we send the light from the monitoring port of the laser head to a wavemeter, which is calibrated to an iodine line (see section 2.5.4). We manually set the laser frequency to $f_{940} = 319.01965\,\mathrm{THz}$ by adjusting voltage, diode current, temperature und grating angle (ordered by how often we change this degree of freedom). When attempting to trap, we set frequencies of $f_{940} \pm 200\,\mathrm{MHz}$ to finetune the ionization laser frequency.

The photoionization laser system was initially set up by Johannes Mielke [65] and was later reoptimized by Fabian Ude [55]. We start with around 1.4 W of infrared laser power at 940 nm, from which around half of the power is coupled into a bow-tie cavity. Inside the cavity, the light is focused into a periodically poled potassium titanyl phosphate (PPKTP) crystal, where part of the 940 nm infrared light is converted to 470 nm blue light with frequency f_{470}. The cavity

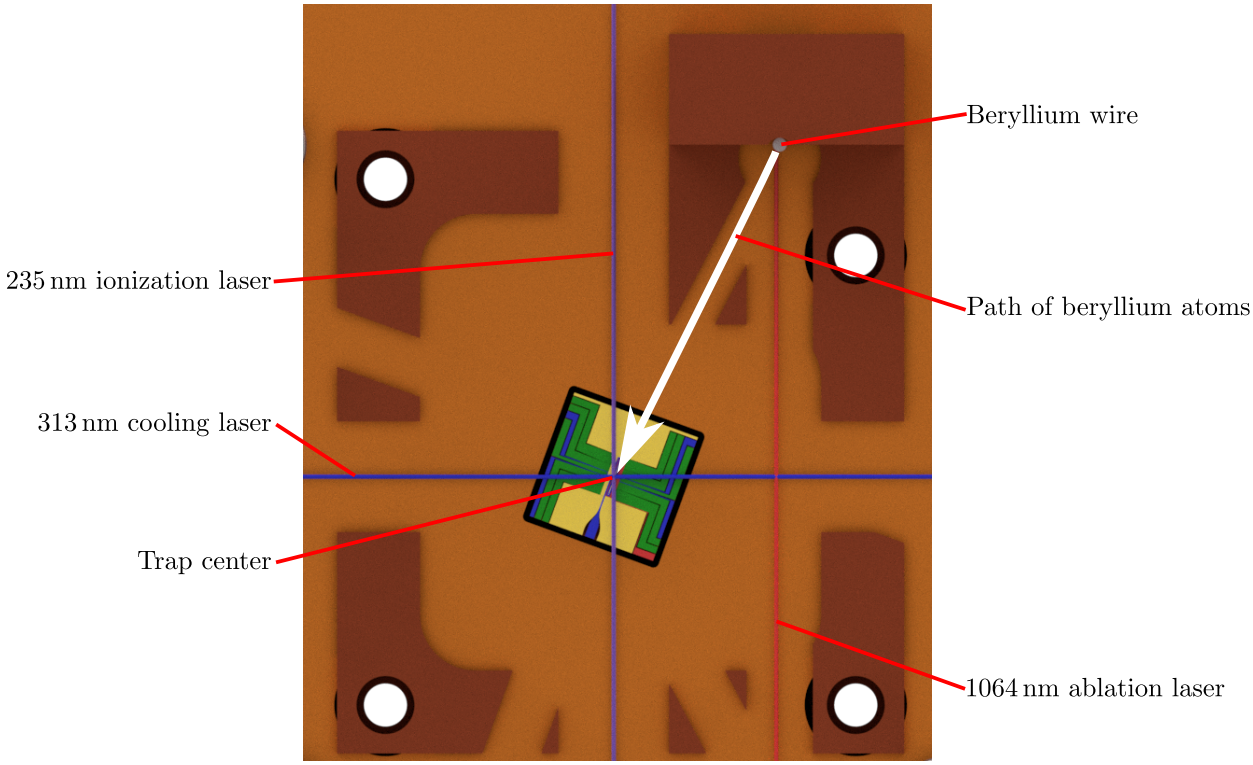

Figure 2.11: CAD view of the trap with surrounding Faraday cage with most of the top parts removed for clarity. Laser beams are illustrated by colored lines for ablation (red), photoionization (purple) and cooling/detection (blue). The white arrow indicates the direction of the ablated beryllium atoms. The trap center is located where the cooling and ionization laser beams intersect each other 70 µm above the surface.

is kept on resonance by adjusting its length with a piezo-driven mirror using the Pound-Drever-Hall (PDH) locking technique [66]. We achieve up to 400 mW of blue laser light out of this cavity.

The blue light with a wavelength of 470 nm is frequency doubled another time to the desired 235 nm UV light with frequency f_{235}. This is done in a second bow-tie cavity which hosts a beta barium borate (BBO) crystal for frequency conversion. As for the first cavity, the second one is kept on resonance using a piezo-mounted mirror and the PDH-technique. Since the alignment for the incoupling mirrors and the cavity itself is very sensitive, it has to be reoptimized around once per week. We usually aim for 2 mW of output power, which enables relatively easy trapping of ions. Trapping also works rarely with power level as low as 0.5 mW, but is not convenient.

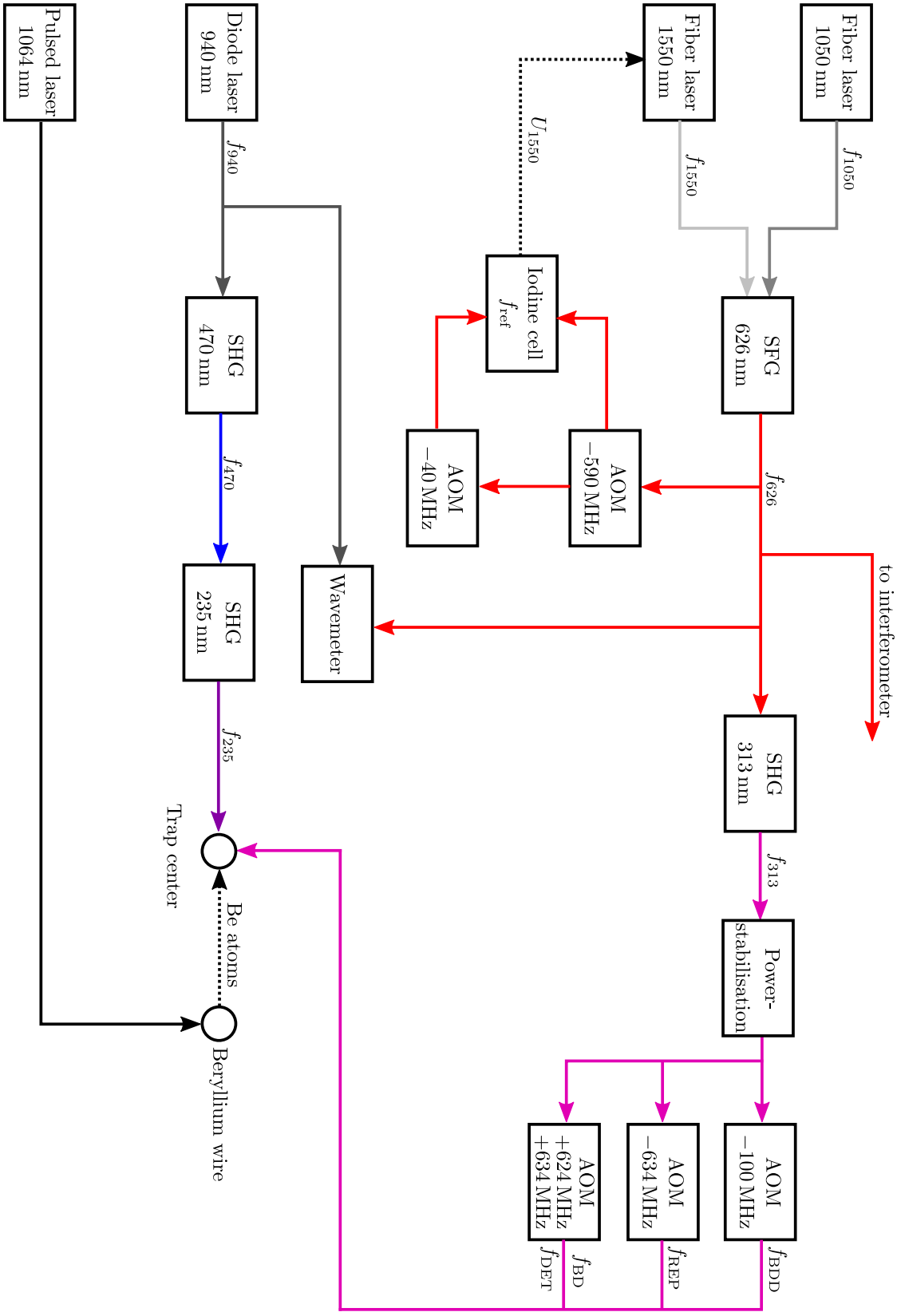

Figure 2.12: Simplified overview of the laser systems used in our experiment. Laser beams are indicated by solid lines. Different frequencies are color-coded and labeled f_i, where i is the denomination of the laser beam. Dashed lines are used to label things that are not laser beams.

2.5.3 Cooling, detection and repumper laser

For Doppler cooling of the ions, detection of their internal states and repumping operations, laser light around 313 nm is needed. Generating light with this wavelength is a two-step process. Our laser system follows the description in [67] and was set up by Kai Voges during his master's thesis [68]. We start with two fiber lasers that run at wavelengths of around 1050 nm and 1550 nm, corresponding to frequencies of f_{1050} and f_{1550}. Both lasers have an output power of 5 W, but only half of the 1050 nm power is used for the purpose discussed here. The other half will be used to set up a Raman laser system in the future together with a second laser at 1550 nm.

Both laser beams are overlapped and focused into a periodically poled lithium niobate (PPLN) crystal in order to produce red light at 626 nm using sum frequency generation (SFG). The frequency of the generated light can be calculated by $f_{626} = f_{1050} + f_{1550}$. We achieve around 1 W of red laser light, which is split into four parts: Second harmonic generation (SHG), frequency stabilization, wavemeter and interferometer.

Most light is sent to a frequency-doubling cavity to generate UV light at 313 nm with frequency f_{313} using an SHG process in a BBO crystal located in a bow-tie cavity, which is kept on resonance using the Hänsch-Couillaud locking technique [69]. The 313 nm light is stabilized in power using a closed control loop consisting of an AOM to diffract a portion of the light, a beam sampler, a photodiode, a PID regulator and a voltage controlled attenuator which is used to adjust the incident RF power to the AOM and therefore adjusting its diffraction efficiency. The non-diffracted beam leaving the AOM, whose power is kept constant, can pass an aperture, while the diffracted beam is blocked.

The power of the 313 nm beam is stabilized to 40...60 mW and then split into three beams using two beam splitters. The first part is used to generate the "blue Doppler detuned"[1] (BDD) beam which is used to cool hot ions directly after they were trapped. It is sent into an AOM in single-pass configuration, which shifts the frequency of the 313 nm beam by −100 MHz to the red, resulting in $f_{\mathrm{BDD}} = f_{313} - 100\,\mathrm{MHz}$.

A second part of the 313 nm beam is sent into an AOM in double-pass configuration, where its frequency is shifted by either 624 MHz or 634 MHz to the blue, producing a beam near-resonant with the transition ${}^2S_{1/2}\,|F = 2m, F = 2\rangle \leftrightarrow {}^2P_{3/2}\,|m_I = 3/2, m_J = 3/2\rangle$. When shifted by 624 MHz, the resulting laser beam is called "blue Doppler" (BD) with a frequency of $f_{\mathrm{BD}} = f_{313} + 624\,\mathrm{MHz}$ and is used to cool ions that were already precooled by the BDD laser beam. When shifted by 634 MHz to $f_{\mathrm{DET}} = f_{313} + 634\,\mathrm{MHz}$, the laser beam is basically resonant with the mentioned transition and is

1 Note that the cooling laser beam is red detuned relative to the ion's cooling transition and this nomenclature has grown historically. The "blue Doppler" beams were initially used to address the ${}^2P_{3/2}$ manifold and the "red Doppler" beams were used to address the ${}^2P_{1/2}$ manifold.

used to detect the internal state of the ion using fluorescence detection [70]. Since Doppler cooling and detection beam are never active at the same time and are really close in frequency, a single AOM can be used to generate both frequencies.

The third part of the 313 nm beam is shifted by −634 MHz to the red using an AOM in double-pass configuration, resulting in a frequency of $f_{\mathrm{REP}} = f_{313} - 634\,\mathrm{MHz}$. This beam is resonant with the $|^2S_{1/2},F=1,m_F=1\rangle \leftrightarrow |^2P_{3/2},m_I=3/2,m_J=1/2\rangle$ transition and is meant for repumping operations during sideband cooling, but also improves the state preparation by helping to depopulate the $|^2S_{1/2},F=1\rangle$ states (c.f. section 4.1.1).

The three laser beams BDD, BD/DET and REP are combined using beam splitters and are coupled into a fiber. At the other end of the fiber these beams are perfectly overlapped. The polarization is cleaned using a Glan-Laser-Polarizer, before it is sent through a $\lambda/2$ and $\lambda/4$ waveplate to generate σ^+ polarized light which is then focused into the trap center using a lens mounted on a three-axis translation stage for alignment purposes.

2.5.4 Frequency stabilization

The frequency stabilization setup used in our experiment was set up by Mariia Stepanova and is discussed in [71]. Part of the red light with frequency f_{626} generated in the SFG process is shifted in frequency to $f_{626} - 590\,\mathrm{MHz}$ using an AOM in double-pass configuration. Part of this light is then shifted again by another AOM to $f_{626} - 630\,\mathrm{MHz}$. This AOM is also used to imprint sidebands with a frequency of 20 kHz onto the laser beam. These two laser beams that are detuned by 40 MHz with respect to each other are overlapped in a counterpropagating way and sent into an iodine cell. Only a specific velocity class of iodine molecules that have a Doppler-shift of +20 MHz for one beam and −20 MHz for the other beam can be addressed by both laser beams. The Doppler-free spectroscopic signal obtained in this way is fed into a lock-in detector to demodulate the 20 kHz sidebands and then into a custom build PI regulator which adjusts the wavelength of the 1550 nm laser to ensure that the shifted 626 nm light is always resonant with the iodine transition at a frequency of $f_{\mathrm{ref}} = f_{626} - 610\,\mathrm{MHz} = 478.69779\,\mathrm{THz}$. The frequency-stabilized light at $f_{626} = 478.69838\,\mathrm{THz}$ is coupled into a fiber and guided to one of the ports of our wavemeter (HighFinesse WS7 with MC8 switch), where it acts as a reference frequency to recalibrate the wavemeter when needed.

2.5.5 Interferometer

A few milliwatts of the 626 nm light are sent to a Michelson interferometer, which is used to detect and quantify vibrations of the experimental apparatus. When the vibration isolation stage of the cryostat is misaligned, the ion trap vibrates relative to the optical table and therefore to the

interferometer's reference mirror. The probe mirror is mounted to the inner vacuum chamber which hosts the ion trap.

There are multiple reasons why the vibrations have to stay at a low level. First of all, the doubling cavities are sensitive to vibrations. The vibrations of the cold head would periodically unlock the cavities once per second, the working frequency of the cryostat. This does not lead to ion loss, but corrupts all the measurements which rely on the number of detected photons. The second reason will be important in the future when we operate with Raman laser beams. The light field at the ion's position has to be phase-stable in order to drive meaningful Raman-transitions. The third reason is that the ion trap does not only vibrate relative to the optical table, but also relative to the EMCCD camera that is used for individual-ion state detection. When vibrating, the images of each ion are blurred and can have a significant overlap with the image of neighboring ions which would lead to a high amount of crosstalk (c.f. section 4.3.1).

2.6 Imaging and detection system

The imaging system used to collect the fluorescence light of the ions and to focus it onto a detector consists of three parts and is described in detail in [56]. The first part is a cryogenic Schwarzschild objective located approximately 8 mm close to the trapped ions (see figure 2.13) inside the inner vacuum chamber. The Schwarzschild-objective is placed on a three-axis translation stage which can be used to scan almost the entire trap chip and to focus the image of the ions onto the detector. The objective has a magnification of 40 and consists of five pieces made of glass that are optically bonded [72] or glued together, respectively. The surfaces of the primary and secondary mirrors are coated with aluminium as a reflective layer and a protective coating. The backside of the beam holding the secondary mirror and the outer ring next to the primary mirror are painted black with *Aquadag* to reduce stray light. A fraction of the light emitted from the ions falls onto the primary mirror and is reflected onto the secondary mirror from where the light is focused through a hole in the primary mirror to a spot approximately 180 mm behind the objective and forms an intermediate image.

The second part of the imaging system consists of a so-called "relay-optics" box (see figure 2.14) that begins at the position of the intermediate image. At this place a motorized aperture is designated to cut away stray light, but it is currently not installed. It was removed for one of the last modifications of the relay optics box and was not reinstalled afterwards because this is a quite tedious process and the slit is currently not needed. Inside the relay optics box, two lenses are placed in tiltable mounts on an optical rail. The overall magnification factor of the imaging system can be adjusted when these lenses are moved along the optical rail. The relay optics box also has the option to install optical filters, which can be useful in future experiments with different ion species.

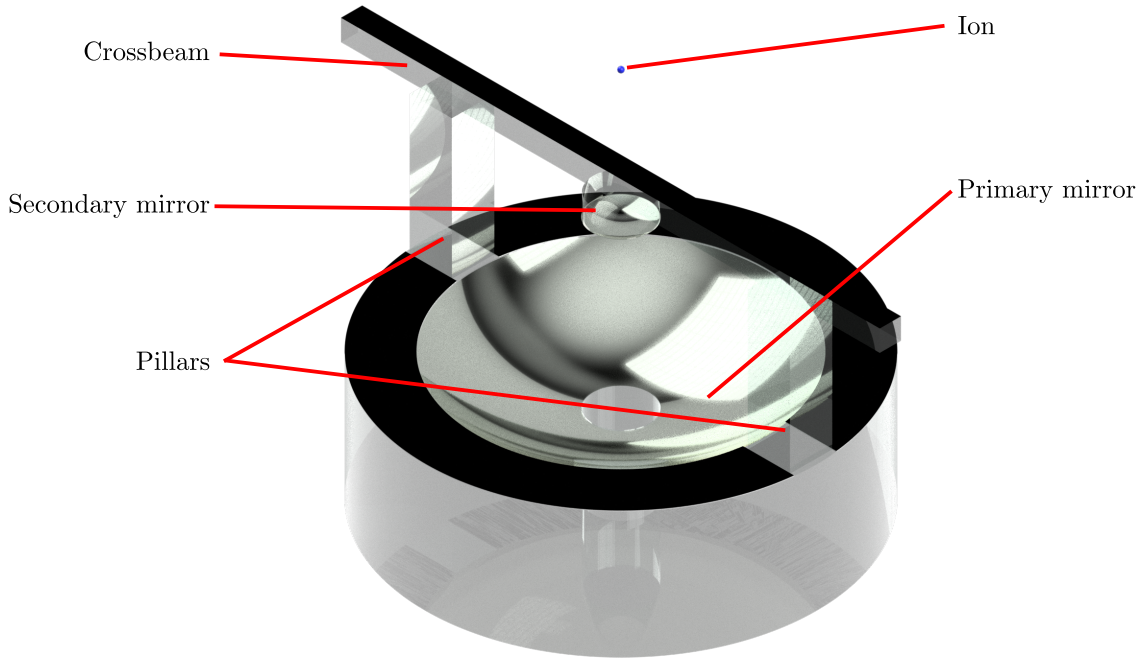

Figure 2.13: CAD view of the cryogenic Schwarzschild objective. The outer diameter of the bottom part is 37 mm, the glass crossbeam has a length of 51 mm and the whole objective has a height of approximately 27.2 mm. The ion's distance to the objective is approximately 8 mm and true to scale, but the ion's size was exaggerated for clarity.

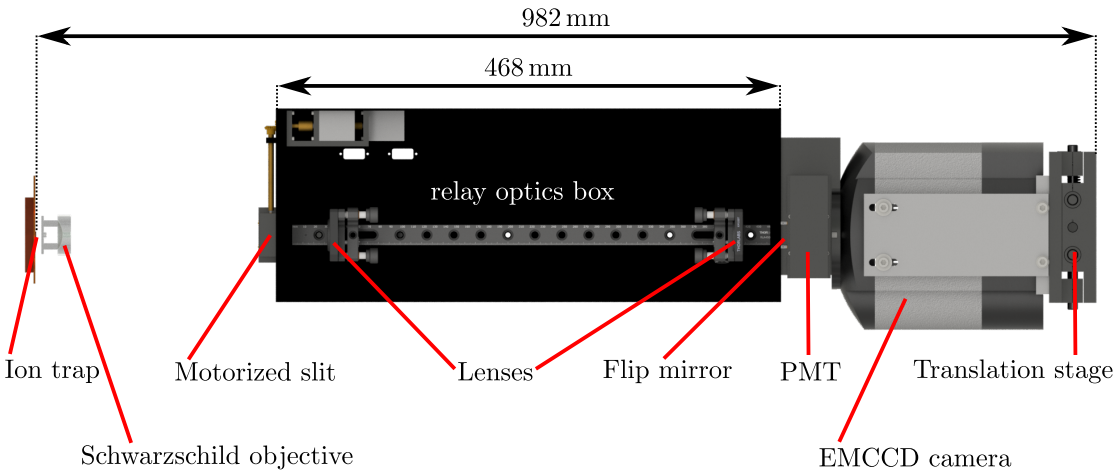

Figure 2.14: Schematic view of the imaging system scaled 1:7. The ion trap and the Schwarzschild objective are at a cryogenic temperature of 5 K. The other components are in air at room temperature. The image is tilted by 90° compared to reality, where the ion trap is at the top and the camera at the bottom.

The third part of the imaging system is the detection unit. A motorized flip-mirror is used to direct the light to either a photomultiplier tube or to an EMCCD camera. The whole structure consisting of the relay optics box and the detectors is placed on a two-axes translation stage for alignment purposes. Great efforts were made to make all parts lightproof to shield the detectors from the room light. Getting everything absolutely lightproof is tedious and has to be redone every time when the relay optics box was opened to move or align the lenses. To avoid this problem, we installed two layers of black curtain around the relay optics box and the detectors which can be removed and reinstalled quickly and easily.

2.6.1 Imaging quality

In [56] the Schwarzschild objective was characterized using a USAF 1951 target and the modulation transfer function (MTF) was measured for two perpendicular axes. Since we obtained the ability to experiment with single ions in the meantime, we were able to investigate the imaging quality of the Schwarzschild objective together with the imaging and detection system by measuring the point spread function (PSF) of a single ion which acts as a point-like source of light. The ion was illuminated with a 313 nm laser beam and imaged onto the EMCCD camera. We took 101 images with 1 second exposure time each, discarded the first image and averaged over the remaining 100 images, leading to a total exposure time of 100 seconds. We noticed during our work with the EMCCD camera that the first image of a data series is sometimes different from all of the following images, therefore we take this precaution. The file generated by the EMCCD camera contains a 16-bit number for each of its 1024×1024 pixels. For the averaged image, the darkest pixel has 375.4 counts and the brightest pixel has 31 117.5 counts. This whole range of numbers was mapped into a grayscale image and is shown in figure 2.15 a). Here we can already see that the PSF does not look like a dot, but rather like a mirrored “c”. Since the Schwarzschild objective used in our experiment once broke at the glass crossbeam and was glued together later, we attribute this image defect to an incorrect alignment between primary and secondary mirror. We performed simulations using Zemax OpticStudio and were able to reproduce the “c”-shape by tilting the secondary mirror.

More details of the PSF can be seen when we reduce the dynamic range of the generated image by reducing the number of counts needed for a pixel to become white. This leads to the imaged ion seeming brighter and the “c”-shape becomes thicker as shown in figure 2.15 b). When we further adjust the brightness and contrast of the image, we end up at figure 2.15 c) and can see several interesting features that were previously invisible and that are highlighted by colored dotted lines. Note that several pixels all over the image are displayed white. On the one hand this can be caused by not all pixels having the exact same sensitivity to light and on the other hand by cosmic radiation that leads to the generation of charges in a few pixels.

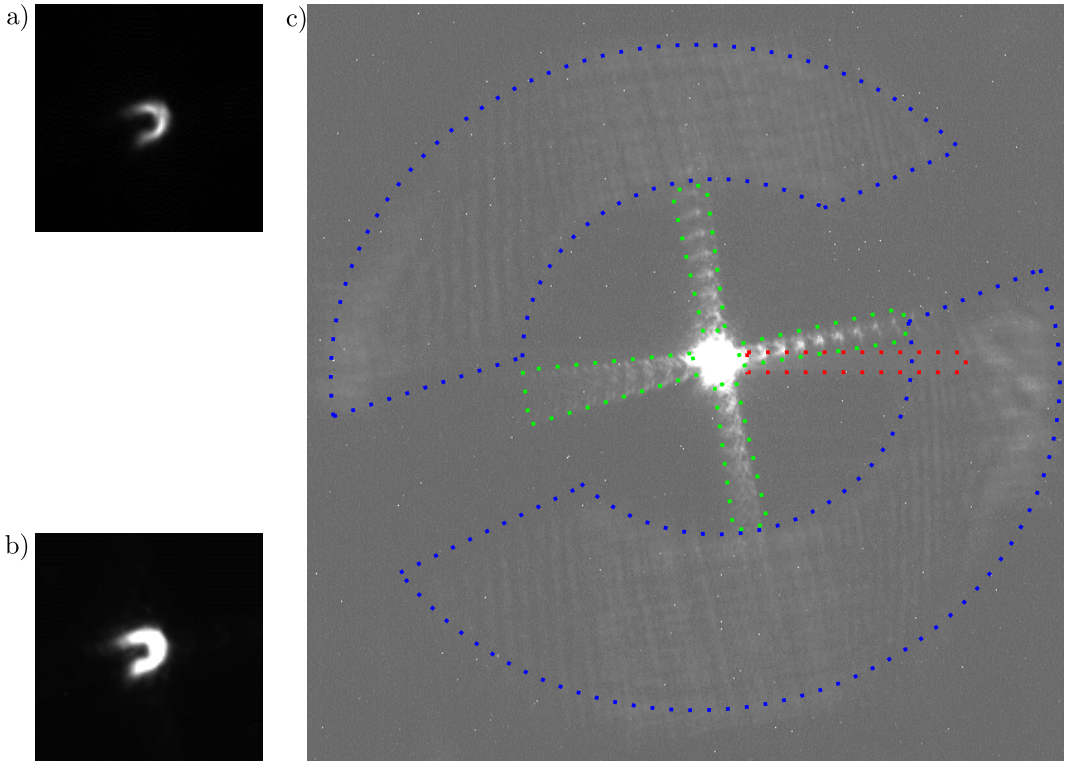

Figure 2.15: Images of a single ion for different contrast and brightness setting. a) Full dynamic range, b) number of counts for white pixel reduced to half, c) heavily adjusted brightness and contrast. In c), image defects are encircled with colored dotted lines. Blue: shape of primary mirror shaded by the glass crossbeam and secondary mirror, green: diffraction spikes, red: CCD related smearing

The areas encircled by blue dotted lines reproduce the shape of the primary mirror which is shaded by the black-painted glass crossbeam and the secondary mirror. The light detected in these pixels need not originate from the ion, but it could be stray light from the trap surface instead. The four areas encircled by green dotted lines can be attributed to diffraction spikes that emerge perpendicular to apertures. Since we observe perpendicular diffraction spikes, these have to be caused by perpendicular apertures. We can attribute these to diffraction at the gold mesh that covers the Faraday cage (c.f. section 2.2.2). Encircled by the red dotted line is a rectangular area of pixels at the right side of the ion's image that is slightly brighter than the surrounding pixels. Since the lowest pixel number in the horizontal direction is on the left side, we know that the CCD sensor is read out from left to right (and bottom to top in the vertical direction). The mentioned area of pixels is therefore read out right after the brightest pixels of the image have been read out. If some charges were not transferred completely, this could lead to some "latecomers" that are detected in the following pixels.

2.6.2 Photon count composition

In the following, we give an overview of the estimated number of measured counts during the detection interval and compare this to the measured value. The upper state of the closed-cycle transition used for Doppler cooling and detection has an average lifetime of $\tau = 8.1(4)\,\mathrm{ns}$ [73] which corresponds to a linewidth of $\Gamma = 2\pi \cdot 19.6(1.0)\,\mathrm{MHz}$. The maximum scattering rate R_{scat} for this transition is $R_{\mathrm{scat}} = \frac{\Gamma}{2} \approx 10^7\,\mathrm{s}^{-1}$ [74]. These photons are spontaneously emitted into a 4π solid angle.

The objective has a numerical aperture of 0.5, which is equivalent to a photon collection efficiency of $\eta_{\mathrm{obj}} \approx 6.7\,\%$. This number of photons is reduced by $34.7\,\% = 1 - \eta_{\mathrm{shad}}$ due to shadowing from the secondary mirror and its holding structure. The gold mesh (Precision Eforming "MG17" [75]) that is part of the Faraday cage (c.f. section 2.2.2) has a transmission of $\eta_{\mathrm{mesh}} = 0.9$ and therefore reduces the amount of light that reaches the objective. The quantum efficiency of both PMT and EMCCD camera at 313 nm is $\eta_{\mathrm{det}} \approx 33\,\%$ [76, 77]. When we now consider a detection interval of $t_{\mathrm{det}} = 400\,\mu\mathrm{s}$, we find a maximum number of detection events of

$$C_{\mathrm{max}} = \frac{\Gamma}{2} \cdot \eta_{\mathrm{obj}} \cdot \eta_{\mathrm{mesh}} \cdot \eta_{\mathrm{shad}} \cdot \eta_{\mathrm{det}} \cdot t_{\mathrm{det}} \approx 50.9. \tag{2.14}$$

During the detection interval t_{det}, the number of counts should converge to C_{max} for increasing laser power after correcting for background counts. In the experiment, we observe a maximum count rate for a single ion of around 87 counts (see figure 2.16) during the detection interval after correcting for background counts. This is 70 % above the predicted value.

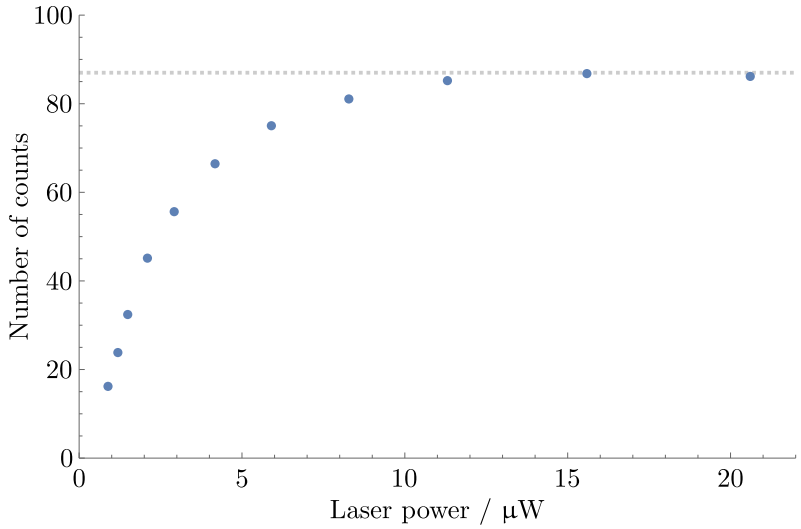

Figure 2.16: Measured saturation curve of a single ion corrected for background counts. For increasing power of the detection laser, the number of counts detected in 400 µs approaches 87 (grey dotted line).

To explain this discrepancy, we have to look into the different paths the light can take to reach the detector (see figure 2.17). The simple calculation leading to equation 2.14 only accounts for the light that takes the direct path to the primary mirror of the Schwarzschild objective (figure 2.17 a)). The scattered light of the ion can also travel in the opposite direction, directly onto the trap surface. Most of the trap surface is made of gold which has a reflectivity of $R_{\mathrm{Au}} = 29.4\,\%$ for light at the detection wavelength of 313 nm [78]. Since the light collection angles α and β (figure 2.17 a) & b)) are almost equal due to the small ion-to-surface distance (relative to the ion-to-objective distance), we can say that reflected light from the trap surface increases the number of counts to $C'_{\mathrm{max}} = C_{\mathrm{max}} \cdot (1 + R_{\mathrm{Au}}) \approx 65.9$.

In addition to reflection at the gold surface, diffuse scattering also takes place which is described by Lambert's cosine law [79]. Most of the light is scattered perpendicular to the trap surface, which is the direction directly towards the Schwarzschild objective. It is obvious that neither the reflected light nor the diffusely scattered light are focused onto the detector. Nevertheless, a portion of these photons does reach the detector according to simulations performed with Zemax OpticStudio. We account the remaining discrepancy between $C'_{\mathrm{max}} \approx 65.9$ and the experimentally measured value of 87 to diffuse scattering at the trap surface and to inaccuracies of the numbers used to calculate C_{max}.

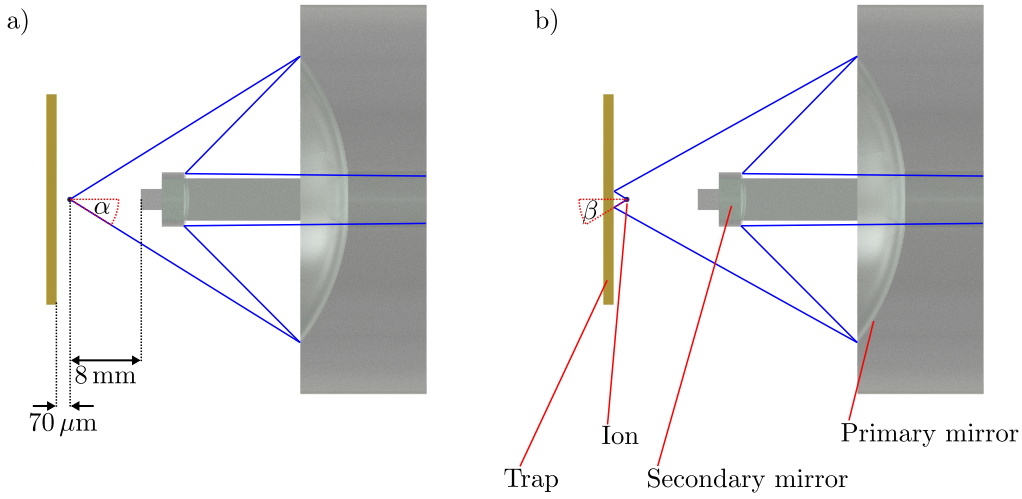

Figure 2.17: Illustration of a trapped ion and the Schwarzschild objective with the outermost possible light path indicated by blue lines. The trap dimensions and the ion-to-surface distance are exaggerated for clarity.
a) Direct path with $\alpha = 29.9999°$, b) indirect path with $\beta = 29.9911°$.

2.6.3 State discrimination

When we apply the detection laser beam, the internal state of the ion is translated into a number of counts by the PMT or the EMCCD camera. This number is then used to determine the qubit state.

For an ion in the dark state, we expect a low number of counts while for an ion in the bright state, we expect a high number of counts. We set a threshold value and interpret all detected numbers of counts below that threshold as an ion in the dark state. If the detected number of counts is at least the threshold value, we interpret the ion as being in the bright state. For any threshold value $t \in \mathbb{N}$, we calculate the resulting relative state preparation and measurement (SPAM) error $\epsilon(t)$ by summing over all wrongly assigned detection events and dividing by the total number of detection events.

$$\epsilon(t) = \left(\sum_{i=0}^{t-1} N_B(i) + \sum_{i=t}^{\infty} N_D(i)\right) / \left(\sum_{i=0}^{\infty} N_B(i) + N_D(i)\right) \tag{2.15}$$

Here $N_{B/D}(i)$ is the number of occurrences to measure the number of counts i for an ion prepared in the bright/dark state.

There are several error sources that are all condensed in the SPAM error. First of all, an imperfect circular polarization of the laser beams leads to an imperfect preparation of the $|2,2\rangle$ state, because the ion can be excited to unwanted states in the $P_{3/2}$ manifold, which then decay to a state different from the $|2,2\rangle$ state. The second and most likely smallest error source is an imperfect transfer between the qubit states and the dark and bright states, which could happen when using the incorrect microwave frequency or pulse duration. As a third error source, there is a finite chance for the detection laser beam to excite the population in the $|1,-1\rangle$ state, which then leads to so-called optical depumping to the bright state, resulting in a high count rate despite the ion initially being in the dark state. Note that in case of a mismatch, it is impossible to tell if the preparation or the detection was imperfect.

3 Characterization of the EMCCD camera

In this chapter, we will explain what the basic working principles of an electron multiplying charge-coupled device (EMCCD) camera are and how we will make use of the camera to implement individual-ion state detection. We characterize the basic properties and functions of the camera and discuss the influence of different parameters on the SPAM error. All settings and measurements discussed in the following are made within the provided software *Andor Solis*. The data taken is saved in the *Flexible Image Transport System* (FITS) format [80] and evaluated in postprocessing using Wolfram Mathematica.

3.1 EMCCD

An EMCCD camera is an advancement to the well-known CCD architecture that was awarded with the Nobel Prize in Physics 2009. In a CCD, information is stored in the amount of electric charges in a potential well and can be moved around to neighbouring potential wells by the application of suitable voltage waveforms to certain electrodes [81, 82]. For a CCD sensor in a camera, the amount of charges in a pixel corresponds to the amount of incident light. These charges are then transferred line by line and column by column towards a readout circuit (see figure 3.1).

The *Andor iXon Ultra 888 UVB* EMCCD camera used for the experiments in this thesis has 1024×1024 pixels in both the image area and the storage area. The image area is exposed to light whereas the storage area is covered with an opaque mask. After illumination of the image area for the desired exposure time, the charges in all pixels are shifted in vertical direction 1024 times, so that the whole image is now in the storage area. While the information in the storage area is read out, the next image can already be taken. It is important to note that the vertical shift operations in the image area and the storage area are independent from each other. The speed of the vertical shift operations can be set in Andor Solis to 4.3 µs, 2.2 µs, 1.13 µs or 0.6 µs. Since we want to implement fast qubit state detection, we choose the fastest possible setting, which is 0.6 µs.

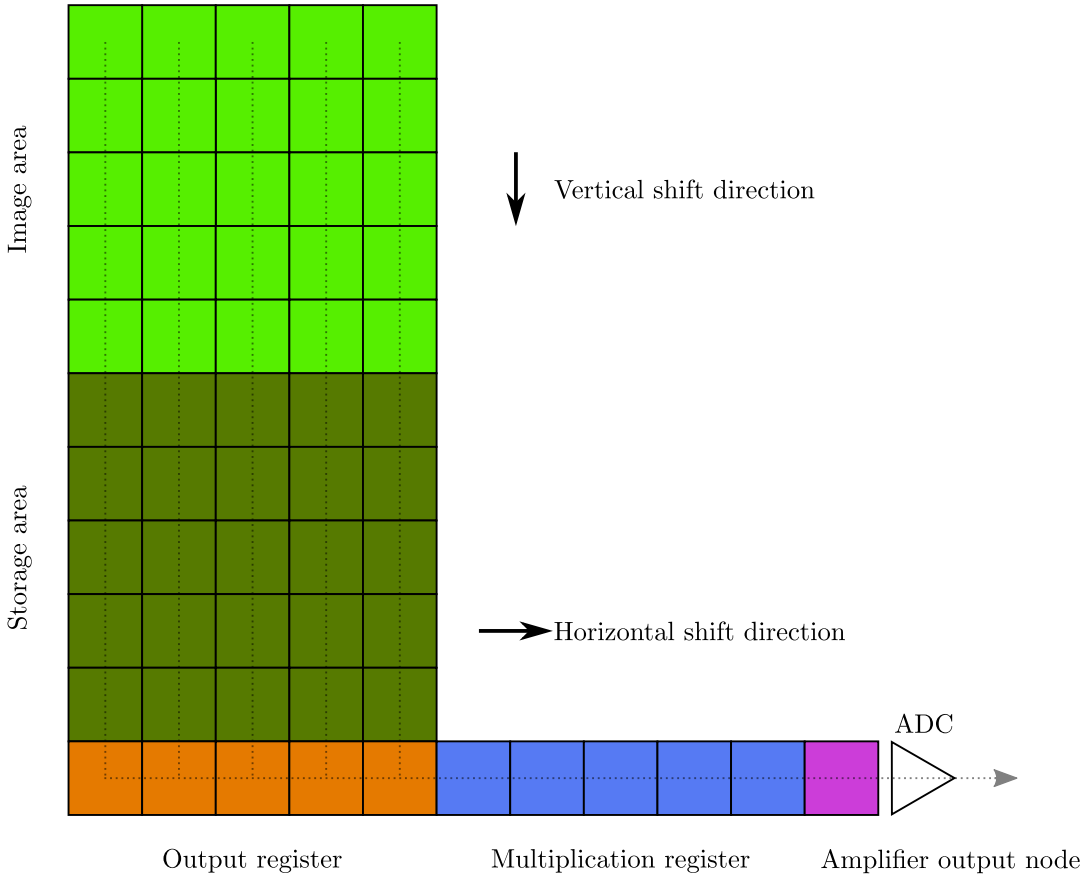

Figure 3.1: Schematic readout sequence in an EMCCD camera with 5×5 pixels. The direction of the flow of information is indicated by the dotted lines. The purposes of the different parts are color-coded. Bright-green: image area, dark-green: storage area, orange: output register, blue: multiplication register, purple: amplifier output node.

From the pixels in the storage area, the charges are shifted into an output register line by line. Starting from here, the shift operations change direction from vertical to horizontal. The horizontal shift speed is the rate at which the charges are shifted through the multiplication register and into the readout circuit, which is depicted as an analog-to-digital converter (ADC) in figure 3.1. The horizontal shift speed - or readout rate - can be set to 1, 10, 20 or 30 MHz. We operate the camera at the fastest possible speed, which is 30 MHz. It is important to note that the readout rate is not the number of images taken per second. To prevent confusion, in this thesis the readout rate is stated in the unit MHz and the number of images per second is referred to as *trigger rate* in the unit s^{-1}.

From the output register, the charges are shifted horizontally into the multiplication register where the amount of charges is multiplied by impact ionization [83]. The electron multiplying (EM) gain can be set between 1 and 1000 in Andor Solis. This method of amplifying the signal can reach noise levels of less than 1 electron per pixel, which is far better than a conventional amplifier could

reach [77]. The amplified signal is shifted into an output node from where an ADC can convert it into a 16-bit binary number.

3.1.1 Clock voltage

For the fastest vertical shift speed - which we plan to use in order to implement fast ion state detection - an increase of the voltages for the shift operations is necessary to ensure a complete charge transfer [84]. This is done by changing the clock voltage setting in Andor Solis from "normal" to a value between "+1" and "+4" (arbitrary unit). The effect of different clock voltage settings on the histograms and on the SPAM-error is shown in figure 3.2.

For this measurement, the ion was prepared 10^4 times in the dark state and in the bright state before the detection laser was applied. The vertical shift speed is 0.6 µs, the readout rate is 30 MHz, the temperature of the CCD chip is set to −60 °C (c.f. section 3.4), the EM gain is set to 300 (c.f. section 3.1.2), the binning areas (c.f. section 3.2) are 38 pixels in the horizontal direction and 32 pixels in the vertical direction with one dummy area (c.f. section 3.2.1) above and one below the binning area of the ion. In these measurements, we did not take into account the temperature transients (c.f. section 3.4.1).

In figure 3.2 a), we see that using a "normal" clock voltage does not work for ion state detection and always yields the same data independent of the qubit's state. We refrain from determining a threshold value since in this case the error would be 50 % for any threshold value. When we apply a higher clock voltage, the histograms become distinguishable (figure 3.2 b) - e)). The resulting SPAM errors are approximately 0.4 % for a clock voltage setting of "+1", "+2" and "+3" with threshold values of 2460, 2056 and 501 counts. For a clock voltage setting of "+4", the threshold is also 501, but with a resulting error of 44 % due to the pronounced peak at 500 counts in both histograms.

From a perspective purely focused on the SPAM error, clock voltages of "+1", "+2" or "+3" would work for single-ion state detection. We decided to use the "+2" settings for future experiments, because it is the middle one of the three working values. We assume that changes to other parameters that could maybe also have an influence on the clock voltage are so small that "+2" remains a good setting, even when "+1" or "+3" would become unusable.

3.1.2 EM Gain

The main task of the electron multiplying (EM) amplifier of the EMCCD camera is to multiply the number of photoelectrons, so that we can overcome the noise of the readout circuit and distinguish between ions in the dark state and in the bright state. To achieve this, the *EM Gain* setting of the

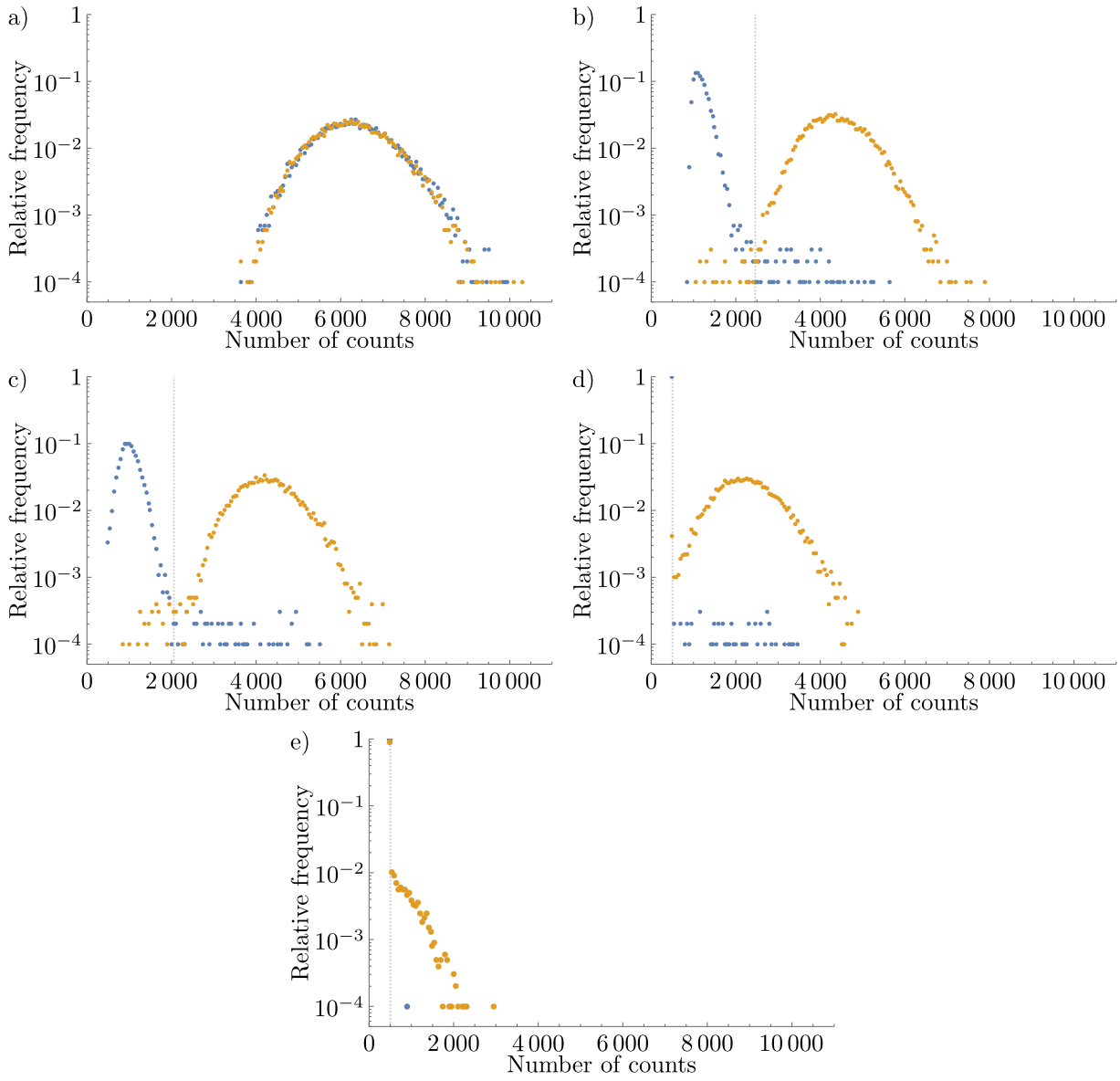

Figure 3.2: Histograms for ions prepared in the dark state (blue) and in the bright state (orange) for different vertical clock voltage amplitudes. 50 data points are binned together horizontally for reasons of clarity. a) Normal, b) +1, c) +2, d) +3, e) +4. The vertical dashed line indicates the threshold value to decide between dark state and bright state.

camera has to be set to the right value. If the gain is too low, the ions in the bright state will yield only a low number of counts during the detection and are easily confused with ions in the dark state. In the histogram representation of the probability distributions of the number of counts for ions in the bright state and in the dark state, the indistinguishability manifests itself in the overlap of the two histograms. If the gain is set too high, it could in principle happen that the ADC is driven out of its input range. Also the EM gain can suffer from long-term aging when operated with high gain.

In figure 3.3, the photon count distributions are shown for ions prepared in the dark state and in the bright state for different EM gain settings. For this measurement, the ion was prepared 10^4 times in the dark state and in the bright state before the detection laser was applied. The vertical shift speed is 0.6 µs, the readout rate is 30 MHz, the temperature of the CCD chip is set to $-35\,^{\circ}\mathrm{C}$ (c.f. section 3.4), the binning areas (c.f. section 3.2) are 33 pixels in the horizontal direction and 32 pixels in the vertical direction with one dummy area (c.f. section 3.2.1) above and one below the binning area of the ion. In these measurements, we did not take into account the temperature transients (c.f. section 3.4.1).

For each EM gain setting, the resulting SPAM error ϵ is determined. We aim for a SPAM error as low as possible not only by setting the EM gain but by optimizing every parameter discussed in this chapter. For every experiment, we check if the detected number of counts matches the expectation for the prepared state.

For a relatively low gain of 200, the overlap between the two histograms is substantial, which results in a SPAM error of around 4 %. The separation of the histograms becomes better with increasing EM gain and the SPAM error decreases. We can see that there is a big jump in ϵ from $G = 200$ to $G = 400$ and only small differences for $G > 400$. We conclude that the effect of increasing EM gain on the SPAM error becomes quite small after surpassing a certain value somewhere between 200 and 400. According to Andor [84], it is recommended to operate the EMCCD camera with an EM gain setting as low as possible. For the characterization of the camera for this thesis, we operated the camera at $G = 1000$ in most of the experiments to determine the best possible results. When the camera is later used in quantum simulation or quantum computation experiments, it is advisable to reduce the EM gain setting if one can afford for the slightly increased SPAM error.

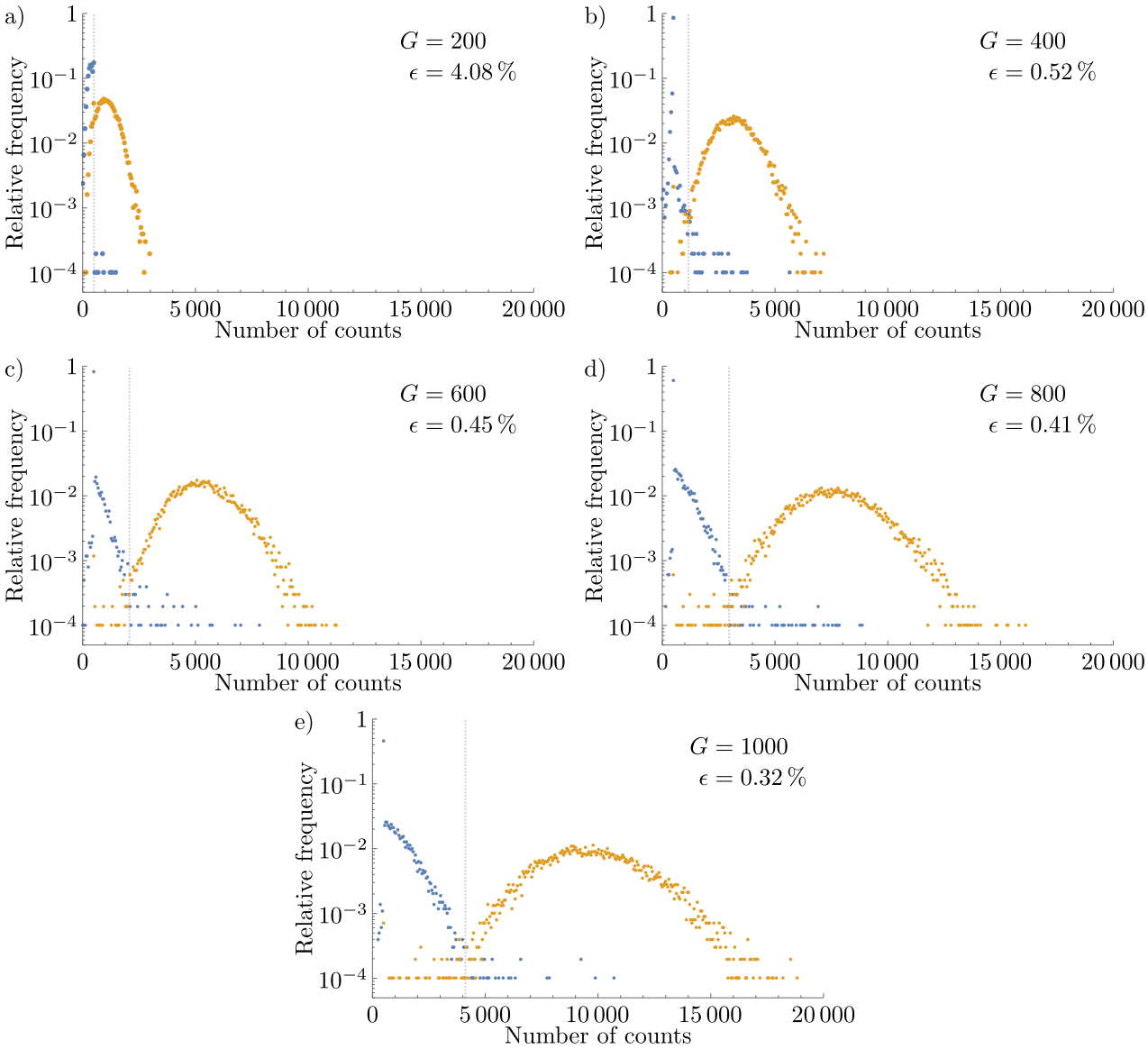

Figure 3.3: Histograms for detection of a single ion prepared in the dark state (blue) and in the bright state (orange). 50 data points are binned together horizontally for reasons of clarity. The dashed grey lines indicate the threshold value to decide between the dark state and the bright state. The EM gain G and the SPAM error ϵ for that gain are stated in each figure a) - e).

3.2 Binning

The detection of the internal state of an ion makes use of fluorescence detection [70]. Two internal states - the bright state and the dark state - are chosen, so that the fluorescence light of the ion is maximal when in the bright state and minimal when in the dark state. With our currently used imaging system, the fluorescence light of one ion is imaged onto several hundred pixels of the camera. Assuming that we cannot change the imaging system in a way that the light from one ion hits exactly one pixel, there are in principle two ways to condense the detected light of several pixels into a single number which corresponds to the amount of fluorescence light emitted by one ion.

The first way is to read out all of these pixels individually and add up the counts in software, called *Software binning*. An advantage of software binning is that arbitrarily shaped patters of pixels, which could even be disjunct, can be added up. Although we use software binning during alignment with a high exposure time on the order of seconds, it is impractical for the short exposure time of 400 µs during a real experiment. Using the number of photons reaching the detector from section 2.6.2, we can estimate that each pixel received less than one photon on average during the detection interval. In this case the readout noise would add up several hundred times and therefore dominate the signal.

Another way to add up the information of different pixels is to make use of the operating principle of the CCD. It is possible to shift several rows of the storage area into the output register before these are shifted into the multiplication register. This technique is called *vertical binning* and accumulates the charges of multiple rows of pixels into a single row. After passing the multiplication register, the charges can be accumulated in the amplifier output node before they are shifted into the readout circuit all at once. This is called *horizontal binning*. In the following the vertical and horizontal binning directly in the CCD is called *Hardware binning*. Since the CCD can only shift a complete row at once, the shape of binning areas using hardware binning is restricted to rectangles.

In Andor Solis we can choose from three different readout modes:

Image
In this mode, all pixels are read out individually by default. It is possible to set how many pixels should be binned together in the horizontal and the vertical direction. Since the binning options in this mode are very inflexible, we use this mode only during alignment and to find suitable binning areas for other readout modes.

Full vertical binning
In this mode a rectangular area of the CCD can be specified in which all pixels are binned together in the vertical direction. The horizontal binning can also be used to combine several of these

vertically binned lines together. This mode is never used for reasons that we discuss in section 3.3.

Multi-track

This mode has the highest flexibility to specify the binning areas and is used to read out the internal state of individual ions. A binning pattern is shown in figure 3.4.

In this mode, an arbitrary number of disjunct tracks can be set up by stating the start row and end row of each track. The number of rows in each track as well as the gaps between two tracks can be arbitrarily set. In the horizontal direction, the flexibility of setting binning areas is reduced. Here we can set the start and end column as well as the number of pixels that should be binned together horizontally which is labeled *HBin* in figure 3.4. In contrast to the vertical binning settings, arbitrary widths and gaps are not possible in the horizontal direction. Because of the limited flexibility in the horizontal direction, we chose to align the camera relative to the ion trap, so that the imaged ions are lined up vertically on the CCD sensor. We use only one binning area in the horizontal direction and one track per ion in the vertical direction. Typical sizes of the binning areas are around 30×30 pixels with small gaps of around 3 to 10 pixels in between to reduce crosstalk (c.f. section 4.3.1).

Binning areas for a two-ion crystal are shown in figure 3.5. This picture was taken using the

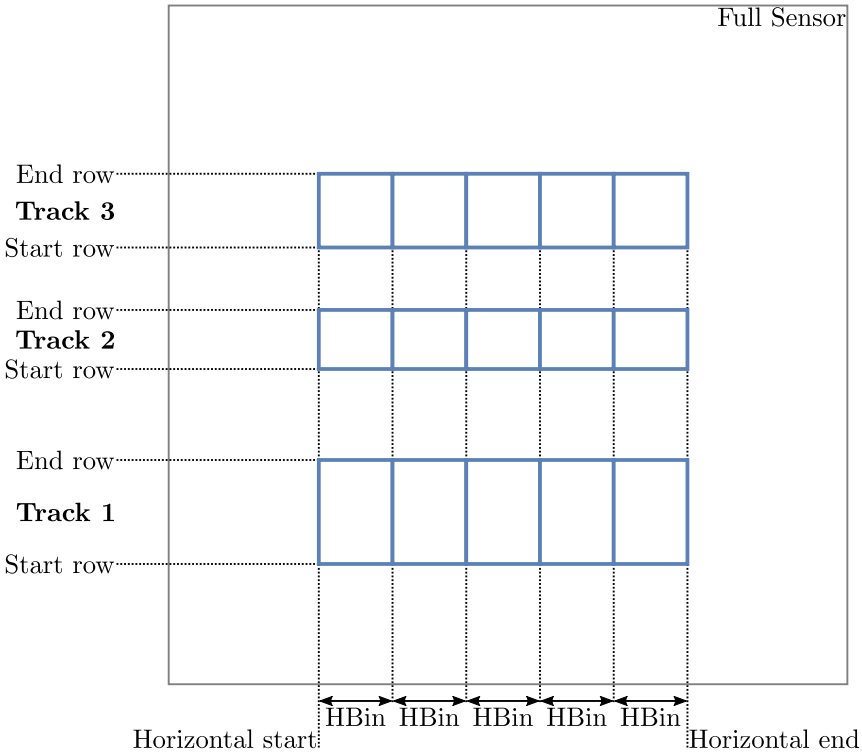

Figure 3.4: Exemplary pattern of binning areas in multi-track mode. Here, three tracks are depicted with five binning areas (blue rectangles) in the horizontal direction.

image-mode without any binning. We use the *Region of Interest* (ROI) feature in Andor Solis to determine suitable borders for the two binning areas. This technique uses software binning and is typically used with an exposure time of around 1 s. We use the video mode to get a live view of the ions and set a ROI around each of the two ions. We can finetune the borders of the two ROIs and also move the illuminating laser beam around until the total amount of light in both ROIs is roughly the same. The coordinates determined in this way are then used to specify the binning areas in multi-track mode.

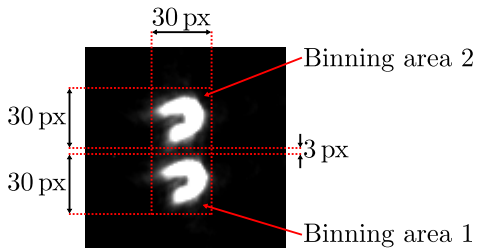

Figure 3.5: Binning areas around two ions with a size of 30 × 30 pixels and a gap of 3 pixels in between are shown.

3.2.1 Effect of additional binning areas

During the early stages of understanding how to operate the EMCCD camera for individual-ion state readout, we started to define additional binning areas adjacent to the binning area of the ion(s). These additional binning areas were meant for debugging purposes since they would have no light-generated charges in them when the timing of the camera trigger and the detection laser were correct and when the camera settings were adjusted to the right values. In case of the detection laser beam being switched on while shift operations are taking place in the CCD, these empty binning areas would have a non-zero number of charges in them. We call these additional binning areas *dummy areas* since they are usually empty. During further experiments with the camera, it turned out that dummy areas are necessary in order to acquire meaningful data (see figure 3.6).

We found that the binning area with the lowest pixel number has a reduced photon count rate. This can lead to a dominant peak at a number of counts of 500 which arises from the nonlinear detection characteristic of the EMCCD camera (see section 3.3). We aim for settings that result in a non-pronounced peak at 500 counts in the histograms to ensure that we operate in the linear regime of the camera's characteristic.

To characterize the effect of dummy areas on the ions' fluorescence histograms, we trapped two ions and prepared them alternatingly in the bright state and in the dark state before applying the detection laser. For this measurement, we used a binning area size of 26 pixels in the horizontal direction and 30 pixels in the vertical direction. The EM gain was set to 1000, the vertical shift

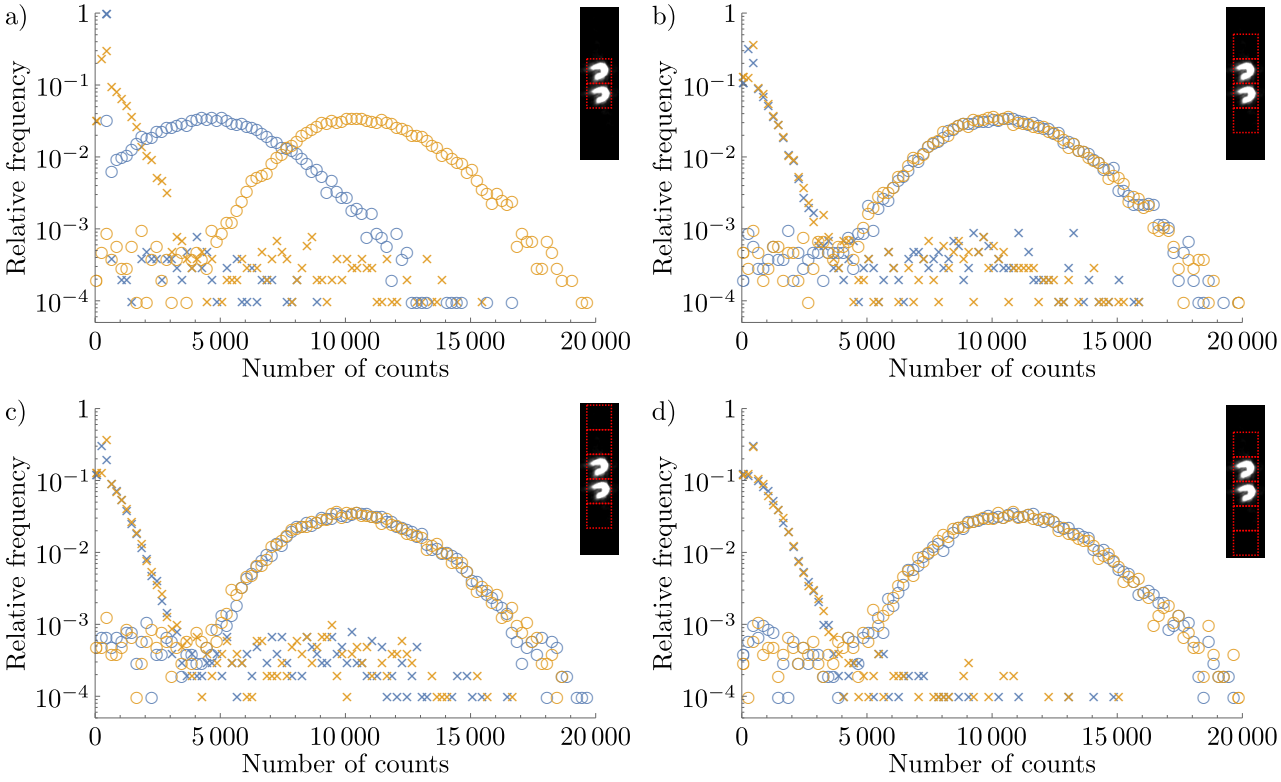

Figure 3.6: Effect of different numbers and positions of dummy areas on the fluorescence histograms. 200 data points are binned together horizontally for reasons of clarity. The ions were prepared in the bright state (circles) and in the dark state (crosses) 10^4 times each. Blue: Ion 1, Orange: Ion 2. a) No dummy areas, b) one dummy area below the ions and one above, c) one dummy area below the ions and two above, d) two dummy areas below the ions and one above.

speed is 0.6 µs, the readout rate is 30 MHz, the temperature of the CCD chip is set to −35 °C and we did not take into account the temperature transient (see section 3.4.1). We repeat the experiment 10^4 times and calculate the average number of counts for preparation in the bright state and in the dark state for each ion independently (see table 3.1). Ideally, the histograms of the fluorescence counts of both ions would be the same for identical preparation.

Without any dummy areas (figure 3.6 a)), it is clearly visible that ion 1 has a lower number of

Dummy area configuration	Ion 1 dark	Ion 2 dark	Ion 1 bright	Ion 2 bright
no dummy areas	532(4)	842(11)	4 735(23)	10 727(24)
1 below, 1 above	765(13)	778(12)	10 516(24)	10 441(24)
1 below, 2 above	746(12)	797(12)	10 456(24)	10 400(24)
2 below, 1 above	762(7)	768(7)	10 990(24)	10 895(24)

Table 3.1: Average number of counts for different numbers of dummy areas below and above the ions' binning areas. Two ions in the trap were globally prepared either in the bright state or in the dark state 10^4 times. Numbers in brackets indicate the standard deviation.

counts. The peak for the preparation in the bright state is around 6000 counts lower for ion 1 than for ion 2. While the Poissonian distribution (with an additional spike at 500) is recognizable for ion 2 in case of preparation in the dark state, ion 1 yields 500 counts in over 99 % of the experiments for the same preparation.

When adding one dummy area below the ions' binning areas and one or two dummy areas above (figure 3.6 b) & c)), the discrepancy of the fluorescence histograms of the two ions vanishes almost everywhere except around 500. It is possible to work with this configuration without any disadvantages since 500 is way below the threshold value to decide between the dark state and the bright state.

When we introduce two dummy areas below the ions' binning areas and one dummy area above, we find perfect agreement of the number of counts for preparation in the dark state for the two ions within the uncertainty limits. For preparation in the bright state, the number of counts differ by around 1 % but still coincide within a $2\,\sigma$ interval. This could be due to statistical fluctuation or because of a slightly imperfect alignment of the detection laser beam, so that the two ions experience a different laser intensity. Another explanation would be that the two ions undergo a different amount of micromotion in the direction of the detection laser beam which would result in a different amount of fluorescence light of the two ions.

The exact reason why the presence of dummy areas affects the number of counts measured in other binning areas is not fully understood. Since the binning area with the lowest pixel number is affected the most and is read out first, the observed phenomenon could be a temporal effect. This could be for example an electrical or thermal transient in the CCD or the readout electronics. Another explanation could be a strange behaviour of the camera's firmware, which we also use to explain the measurements described in section 3.4.2.

We conclude that two dummy areas below and one dummy area above the ions' binning areas is the best configuration to ensure equal characteristics for the detection of both ions' fluorescence light. However, it is sufficient to work with only one dummy area below and one dummy area above the ions' binning areas to perform individual-ion state detection experiments. This is the binning area configuration for most of the experiments that are presented in this thesis.

3.3 Count linearity

The fluorescence detection used to readout the ions' internal state yields a certain number of counts during the detection interval that depends on the internal state in which the ion has been. An ideal detector would be able to detect every incident photon. As already discussed in section 2.6.2, not all photons reach the detector and the quantum efficiency is smaller than 1. Therefore, the number of detected photons is always smaller than the number of incident photons, but the ratio between

the two quantities would still be constant for any amount of incident light. Both the PMT and the EMCCD technology suffer from different effects that lead to a nonlinear characteristic of the number of measured counts depending on the amount of incident light.

The finite pulse-pair resolution of a PMT results in a reduction of the measured number of counts due to dead time. For the PMT used for the measurements presented in this thesis, the pulse-pair resolution is $t = 20\,\text{ns}$ [76]. The datasheet provides an equation to calculate the real count rate N from the measured count rate M and the pulse pair resolution t as follows:

$$N = \frac{M}{1 - Mt} \tag{3.1}$$

We find that the correction is on the order of 0.2 % in the case of 45 counts detected in 400 µs for a single ion in the bright state. We refrain from correcting for the PMT nonlinearity during this thesis since such a small deviation has no noticeable effect in any of the performed measurements.

In case of a detection using the EMCCD camera, dead time between two arriving photons does not play a role. However, several effects are conceivable which would result in an upper limit for the measured number of counts. The potential wells in which the electrons are stored in the CCD have a maximum amount of electrons which they can hold. This would result in a nonlinear characteristic for a very high amount of incident light. Since the currently used imaging setup leads to < 1 photon per pixel on average, we do not have to consider this source of nonlinearity.

The final step of the readout circuit of the EMCCD camera is an analog-to-digital converter (ADC). Especially when using high EM gain settings as we do for our experiments, the maximum output value of the ADC can easily be reached and therefore leads to a nonlinear characteristic for high count numbers. The upper limit of the ADC in the EMCCD camera is $2^{16} - 1 = 65\,535$. This number has to be compared with the typical number of counts for a bright ion, which is around 20 000 at the right end of the measured histograms. Therefore, we can safely assume that our measurements do not suffer from nonlinear effects in the regime of a high number of counts.

However, we still have to consider the case of a very low number of incident photons as it is the case for ions in the dark state or for empty binning areas. As already seen in figure 3.6, the histograms experience an unphysical spike at 500 counts which is the *baseline clamp level*. This offset is applied to the signal, so that a perfectly dark pixel would be measured as 500 counts instead of 0 counts. We know from an email correspondence with Andor that the signal can be outside of the ADC range in multi-track readout mode when using high vertical shift speeds. This behaviour originates from the camera being optimized in image mode. Andor offered us to reprogram the camera's EEPROM in a way that the readout is optimized for the mode of operation which we are currently

using. The downside of this reversible change would be that the ADC range is reduced in image mode. Up to now, we did not try the modified EEPROM, but it is very likely that we will try it in the future when we want to use the EMCCD camera for quantum simulation and quantum computation experiments.

We determined the characteristic of the EMCCD camera and compared it with the PMT. For this measurement, a single ion was illuminated with the detection laser beam for a varying duration. The length of the illumination was scanned from 1 µs to 1981 µs in steps of 20 µs. For every illumination duration, the experiment was repeated 1000 times. The average number of counts for every illumination duration is shown in figure 3.7 for detection with the PMT and with the EMCCD camera. For this measurement we used a binning area size of 31×31 pixels and one dummy area below and one above the ion's binning area. The vertical shift speed was 0.6 µs, the readout rate was 30 MHz, the temperature of the CCD chip was set to −35 °C (c.f. section 3.4) and we did account for the temperature transient (c.f. section 3.4.1) by running the measurement twice in a row. It is important to note that we had some issues with the amount of fluorescence light we could get from the ion on the day of this measurement. Therefore, the commonly used detection time of 400 µs only yields around 10 counts on the PMT instead of around 45. The functional description of this section has therefore only a qualitative character.

The illumination time is proportional to the total amount of light arriving at the detector during the detection interval. The expected characteristic of the detector is a line through the origin in case of detection with the PMT. For detection with the camera the line should be shifted upwards by 500 counts due to the baseline clamping. In figure 3.7 a), it is clearly evident that the expectation is fulfilled for the PMT. The number of counts $C_{\mathrm{PMT}}(t)$ measured with the PMT for an illumination time t can be described with a linear function of the form $C_{\mathrm{PMT}}(t) = \alpha \cdot t$ with $\alpha = 0.024537(24)\,\mu\mathrm{s}^{-1}$, resulting in a coefficient of determination $R^2 = 0.9999$.

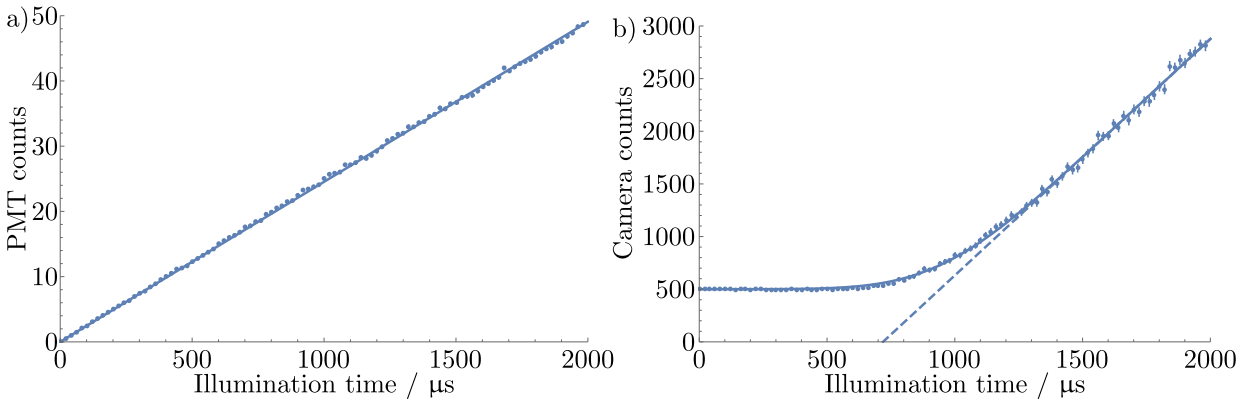

Figure 3.7: Measured number of counts depending on the duration of illumination with the detection laser beam. a) Detection with PMT, b) detection with EMCCD camera. Points: Experimental data, solid line: fit, dashed line: asymptote. The error bars indicate the standard deviation in b). In a), the error bars are smaller than the data points.

Unlike the PMT, the measured characteristic of the EMCCD camera clearly does not follow a linear function (figure 3.7 b)). For a small amount of light arriving at the camera during the detection interval, the reading is always 500 because the ADC is operated outside of its range. Starting at around 500 µs of illumination time, the reading begins to increase in an accelerated way until it reaches its asymptote at around 1300 µs of illumination time. We found an empiric description of the camera's characteristic by integrating the error function $\mathrm{erf}(t)$ and applying suitable shifts and scale factors. This function was chosen because it features two different finite limits for $t \to \pm\infty$ and a smooth transition between the two limits. Other functions like $\arctan(t)$ also have this features but are much harder to motivate since the trigonometric functions are usually related to angles and circles which are both absent in this experiment. The error-function on the other hand is closely related to the probability distributions which are used to describe the data in our experiments. We shift the error-function upwards by 1, so it starts at zero and approaches a final value of 2 for $t \to \infty$. Starting at zero and approaching a final non-zero value is exactly what we want for the *derivative* of the function that describes the camera's characteristic. Therefore, we have to integrate the shifted error-function and obtain

$$\int_{-\infty}^{t} 1 + \mathrm{erf}(\tau)\mathrm{d}\tau = \frac{e^{-t^2}}{\sqrt{\pi}} + t(1 + \mathrm{erf}(t)). \tag{3.2}$$

We shift this function by t_0 and scale it by a in the horizontal direction and shift it upwards by the baseline clamp level of 500 and scale it vertically by a factor b. We obtain an expression for the camera's characteristic $C_{\mathrm{Cam}}(t)$ of the form

$$C_{\mathrm{Cam}}(t) = 500 + b\left(\frac{e^{-(\frac{t-t_0}{a})^2}}{\sqrt{\pi}} + \frac{t-t_0}{a}\left(1 + \mathrm{erf}\left(\frac{t-t_0}{a}\right)\right)\right). \tag{3.3}$$

The best fit yields $t_0 = 942(8)\,\mu\mathrm{s}$, $a = 360(16)\,\mu\mathrm{s}$ and $b = 404(22)$ with a coefficient of determination $R^2 = 0.9996$. The linear part of the function for high illumination time has a slope of $\frac{2b}{a} = 2.25(16)\,\mu\mathrm{s}^{-1}$ and is indicated in figure 3.7 b) by the asymptote.

From our experiences with the camera, we know that the qualitative shape of $C_{\mathrm{Cam}}(t)$ is always the same. Depending on the exact camera settings, the flat part with a constant number of counts of 500 can be stretched out more or less. When we apply suitable shifts and scaling factors to equation 3.3, every characteristic between a perfect linear slope and a flat line can be described.

Settings have to be used that result in fluorescence histograms which have a threshold value to decide between the dark state and the bright state way above 500 counts in order to keep the SPAM error low. We found that the size of the binning areas around the imaged ions can have a significant influence on the camera's characteristic. Choosing the binning areas either too small or

too large both result in a dominating spike at 500 counts in the fluorescence histograms for ions in the dark state and in the bright state. This effect goes all the way up to exclusively reading 500 counts independent of the ion's internal state for very large binning areas. This was especially observed when we tried out the *full vertical binning* readout mode with a binning area size of 32×1024 pixels.

3.4 Cooling

The *Andor iXon Ultra 888 UVB* features thermoelectric cooling of the CCD sensor. One effect of cooling the sensor is a reduced amount of dark counts in the CCD. This is especially relevant for applications with very long exposure times. Due to the short exposure time of 400 µs in our experiments, dark counts are no issue for us. The reason for cooling the chip is the lower resulting SPAM error in our measurements and the reduced appearance of the spike at 500 counts in the histograms. A possible explanation for this observations is a reduced amount of electronic noise in the CCD and the readout circuit at lower temperatures. Lower noise leads to less broadened histograms and therefore less overlap between the count distributions of ions in the dark state and in the bright state. The reduced overlap directly results in a lower SPAM error. To explain exactly how the observed temperature dependence of the spike at 500 counts works, we would have to know how the camera's firmware works, therefore we can only take it as granted.

Another observation that we cannot explain without knowing about the camera's internal operating principle is that the count reading does not only depend on the current temperature but also on the temperature setpoint. This means that we get different results for measurements performed at an equilibrium temperature of e.g. $-35\,^{\circ}\mathrm{C}$ with a setpoint of $-60\,^{\circ}\mathrm{C}$ than for a measurement performed at the same temperature but with a setpoint of $-120\,^{\circ}\mathrm{C}$. This observation emphasizes that it is absolutely crucial to always operate the camera at a stable temperature.

In Andor Solis we can set the temperature setpoint of the CCD. The current temperature is displayed in steps of $5\,^{\circ}\mathrm{C}$ and the background color of the temperature indicator shows if the temperature is stable (blue) or not (red). What limits the lowest achievable temperature of the CCD is the heat load in the chip which highly depends on the camera settings and the trigger rate. Since thermoelectric coolers generate a temperature difference between the cooled object and some sort of reservoir, the type and temperature of the refrigerant also plays a role for the achievable temperature. To determine this temperature for a certain set of camera settings and trigger rate, we let the camera run while the target temperature is set to the lowest possible setting ($-120\,^{\circ}\mathrm{C}$) to ensure that the cooler always runs on its full power since this temperature can never be reached with the cooling methods we use. When the temperature indicator has reached a stable value after several minutes, we set the temperature setpoint to a value $5\,^{\circ}\mathrm{C}$ higher than the measured lowest

achievable temperature. This ensures that the CCD temperature can maintain a stable value during the following experiments.

The amount of heat load on the CCD can be divided into a static part which only depends on the camera settings and a dynamic part that depends on the trigger rate. According to the Andor iXon Ultra 888 hardware guide [84], the settings with a strong influence on the cooling performance are vertical binning, fast vertical shift speed and an increased vertical clock amplitude as well as the size of the regions of interest. In our experiments we noticed that the horizontal shift speed (or readout rate) also has an effect on the cooling performance. The lowest stable camera temperature we have ever achieved is $-100\,°\mathrm{C}$ for a horizontal shift speed of 1 MHz, which is the slowest possible setting.

Since the goal of the experiments is to perform *fast* individual-ion state detection, considering only the static heat load is not useful. With every trigger signal, a series of shift operations in the CCD followed by amplification and readout is released. Every operation in the camera generates heat and the total amount of heat load therefore depends on the rate of trigger events per unit of time. The camera's temperature is stable when the heat load and the cooling power are equal. Since the dynamic heat load is proportional to the trigger rate and the cooling power decreases for lower temperatures, higher trigger rates come with a higher temperature (see figure 3.8).

In that plot, the effect of different readout rates on the achievable temperature is evident. For 1 MHz readout rate, the maximum achievable trigger rate is limited; therefore, the datapoints end at $50\,\mathrm{s}^{-1}$. Note that the data points for a readout rate of 10 MHz do not end at a trigger rate of $160\,\mathrm{s}^{-1}$ due to a speed limitation but because we did not want to overheat the camera. For the measurements in figure 3.8, the camera was connected to the lab's cooling water system. This system contains a closed circulation of a mixture of around 30 % *Antifrogen N* by volume and water. This refrigerant

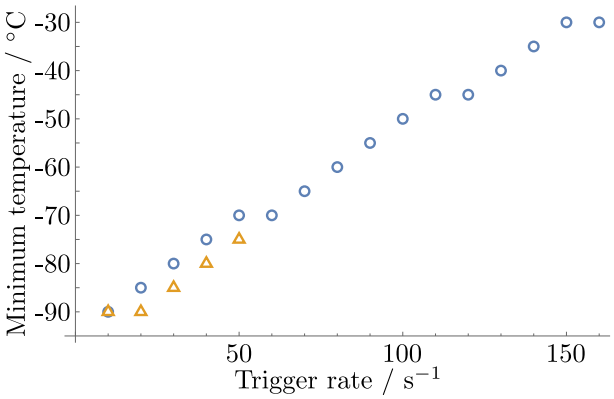

Figure 3.8: Lowest achievable temperature depending on the trigger rate plotted for a readout rate of 10 MHz (blue circles) and 1 MHz (orange triangles). The camera is cooled with a mixture of Antifrogen N and water at a temperature of 21 °C.

is temperature stabilized to 21 °C and is also used to cool the magnetic-field coils used in our experiment and a cryo compressor in a neighbouring lab. The main reason why Antifrogen N is mixed into the cooling water is its anticorrosive property.

The reason why we changed to water cooling of the camera is that we hoped to achieve a lower temperature compared to using air cooling with the fan integrated in the camera housing. The effect in achievable temperature was barely measureable. Most of the time, no change in temperature was observed and only under certain conditions 5 °C lower temperatures were reached, which is also the resolution of the temperature indicator and therefore to be treated with caution. One should note that the air cooling of the camera was still active when the cooling water was applied. Since we did not observe any significant improvement of the cooling performance, we were afraid that the two cooling methods interfere with each other. As a result, we switched off the fan responsible for air cooling of the camera, so it runs explicitly on water cooling. Disabling the fan can be done within Andor Solis. This had no effect on the temperature but surely on the data that we read from the camera. We assume that the camera's fan does not only cool the CCD but also other parts of the electronics. Since we did not want the camera electronics to overheat, we switched the fan back on.

In a next step, we installed a heat exchange unit (called *chiller*) between the lab's cooling water supply and the camera. As refrigerant for the chiller's cooling cycle, we use again a mixture of Antifrogen N and water. The chiller allows us to set a lower temperature of the refrigerant for the camera than for the rest of the lab. We aim for a temperature of the refrigerant as low as possible in order to achieve the lowest possible CCD temperature.

The lower limit for the temperature of the camera's refrigerant is given by the dew point in our lab which depends on the lab's air temperature and the relative humidity. If the refrigerant were cooled below the dew point, water vapor from the air would condense on the hoses running between chiller and camera. This problem could be solved by using some isolating material around the hoses. Another issue is that water would also condense inside of the camera's housing where it could damage the electronics. Therefore, the refrigerant's temperature must be above the dew point at any time.

Andor Solis has a built-in dew point calculator that can help to find a safe temperature for the refrigerant. At the time when we installed the chiller, the relative humidity of the air in the lab was around 50 %. Together with the lab's air temperature which is stabilized to 22 °C with residual fluctuations on the order of 0.2 °C, the dew point is calculated to be around 11 °C. The calculator within Andor Solis adds 2 °C to the dew point, resulting in 13 °C, and claims that this is a safe working temperature. We regularly check the humidity in our lab so we could change the temperature of the refrigerant if needed.

Lowering the refrigerant's temperature had a significant effect on the camera's cooling performance. With a flow of around $1.5\,\frac{\mathrm{L}}{\mathrm{min}}$ of 13 °C cold refrigerant, we are able to maintain a stable camera temperature of −35 °C at a trigger rate of $200\,\mathrm{s}^{-1}$. We estimate that we would be able to achieve even higher trigger rates at a maintained camera temperature of −35 °C when we reduce the refrigerant's temperature even further. To be able to do this, a low humidity atmosphere must be present around the camera to lower the dew point. This atmosphere must be kept inside some sort of container around the camera. The container must have several feedthroughs for cables and hoses which would make it pretty hard to get it absolutely air tight. Assuming that we will always have a finite rate of air and humidity going into the container, we need a way to permanently remove water from that container. We have thought of three basic principles how this could be achieved:

- Attach a vacuum pump to the container to remove as much of the humid air as possible from the container.
- Use a dehumidifier to remove the water from the container's atmosphere.
- Apply a flow of dry air or any inert gas (like nitrogen) to the container, so that a slight overpressure inside the container emerges which keeps the wet air from the lab outside of the container.

None of these ideas have been further pursued since they require nontrivial changes to the imaging system.

With the addition of Antifrogen N to the refrigerant, temperatures below 0 °C become accessible, since its main ingredient is monoethylene glycol which is used as an antifreeze. To make use of this capability and be able to potentially reach higher trigger rates of the camera, a suitable chiller with sufficient cooling power has to be used as well as the mentioned container for the camera has to be employed.

3.4.1 Transients

A sudden change in the heat load of the camera's cooling circuit leads to a transient response of the temperature controller. Before an acquisition is started, we let the camera run in video mode with the desired trigger rate to check if a stable temperature settles or not. To change from this mode to the data acquisition mode both the camera and the trigger pulses coming from the experiment control system have to be stopped for a short time. Then we first have to start the camera acquisition followed by the experiment that we want to run. This usually takes a few seconds. The temperature indicator in Andor Solis is not sensitive enough to resolve the temperature fluctuation during this short time interval. However, we can tell from the measurements that the camera's

temperature is undergoing a transient response after a new measurement is started (see figure 3.9).

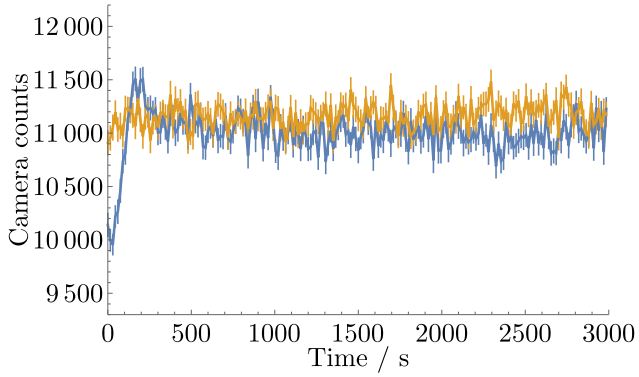

Figure 3.9: Time development of the number of counts after a readout sequence is started. Blue: First run, orange: second run. One datapoint corresponds to the average value of 500 measurements. The datapoints are connected by thick lines to guide the eye. The thin vertical lines indicate the standard deviation for that datapoint.

The presented data is extracted from a measurement during which two ions were alternatingly prepared in the bright state, in the dark state and in a superposition state between the former two. For the following evaluation, we only look at the fluorescence of the first ion when it was prepared in the bright state. The experiment control system was set up in a way that it runs the experiment 10^5 times two times in a row, which took 6000 s in total. The readout rate was 30 MHz, the vertical shift speed was 0.6 µs, the EM gain was 1000, the camera temperature was set to −35 °C and we used two dummy areas below the ion of interest and one dummy area above the other ion. For the presentation in figure 3.9, we average over 500 measurements each and distinguish between the first and the second run of the identical measurement sequence. A transient response during the first few hundred seconds of the first run is clearly visible. During the second run, the measured number of counts does not show this behaviour. It seems that the number of counts is slightly higher in the second run than in the first run, which could be caused by long-term drift in the laser power.

For most of the measurements presented in this thesis, the experimental sequence was run two times in a row and the first run was discarded. It is highly recommended to wait for at least 5 minutes after every change in the camera's heat load or the temperature setpoint even when Andor Solis indicates a stable temperature.

3.4.2 Effect of different temperatures

The temperature of the camera affects the photon count distributions for ions prepared in the bright state and in the dark state, respectively. In figure 3.10, the photon count distributions are depicted for camera temperatures between −80 °C and −20 °C. For each temperature, a single

ion was prepared 10^4 times in the dark state and in the bright state to obtain the distributions shown in the histograms. For this measurement, the camera was operated with a readout rate of 30 MHz, a vertical shift speed of 0.6 µs and an EM gain of 300. The binning area size is 38 pixels in the horizontal direction and 32 pixels in the vertical direction. One dummy area is used below and one above the binning area of the ion. The measurement was performed before we knew about the presence of the temperature transient described in section 3.4.1 and therefore the data may suffer from this effect. Since the measurements only took around 7 minutes to complete (except the one at −80 °C), we cannot afford discarding the first few minutes during postprocessing.

The SPAM error ε stated in figure 3.10 a) - h) is determined by the threshold method described in section 2.6.3. From the plots, we can tell that all of the histograms are shifted to a lower number of counts for an increasing camera temperature. The threshold value indicated by the grey line is located where the two histograms intersect each other for $T \leq -30\,°\mathrm{C}$ (estimated by eye). For temperatures of −40 °C and above, the spike at 500 counts is clearly visible. We see that the SPAM error ε is almost constant with a value of around 0.3 % as long as the two histograms intersect at a number of counts greater than 500 which is the case for temperatures of −30 °C and below. For temperatures of −25 °C and above, the intersection of the two histograms is below 500 counts and ε starts to increase.

It is counterintuitive that all histograms shift to the left for higher temperatures. A shift to the right could be explained by additional dark counts generated by thermal noise which are more likely to appear at higher temperatures. Since we already know that the temperature setpoint has an influence on the camera's characteristic, we presume that the observed shift is dominated by the camera's firmware and not by any physical effect.

The histogram for the preparation in the dark state looks different in figure 3.10 c) than in the other figures. It seems that there is a jump at around 500 counts instead of a spike like in most of the other histograms. Also the SPAM error is slightly higher for this measurement performed at a temperature of −50 °C compared to measurements at nearby temperatures. A possible explanation could be the fact that we did not account for the temperature transient and the controller underwent some overshoots or similar. This could be caused by a different time sequence when starting the measurement compared to all the other measurements.

Since we thought that the increase of the SPAM error for temperatures of −25 °C and above could be related to the spike at 500 counts, we tried out a workaround. We reallocated all the events at 500 counts to 0 counts and recalculated the best threshold value and the resulting SPAM error. With this technique, the threshold value for $T = -20\,°\mathrm{C}$ moved from 501 to 186 and the SPAM error ε could be reduced from 0.81 % to 0.53 %. This shows that the unphysical spike at 500 counts has some effect on the SPAM error, but is not exclusively responsible for the increase of ε.

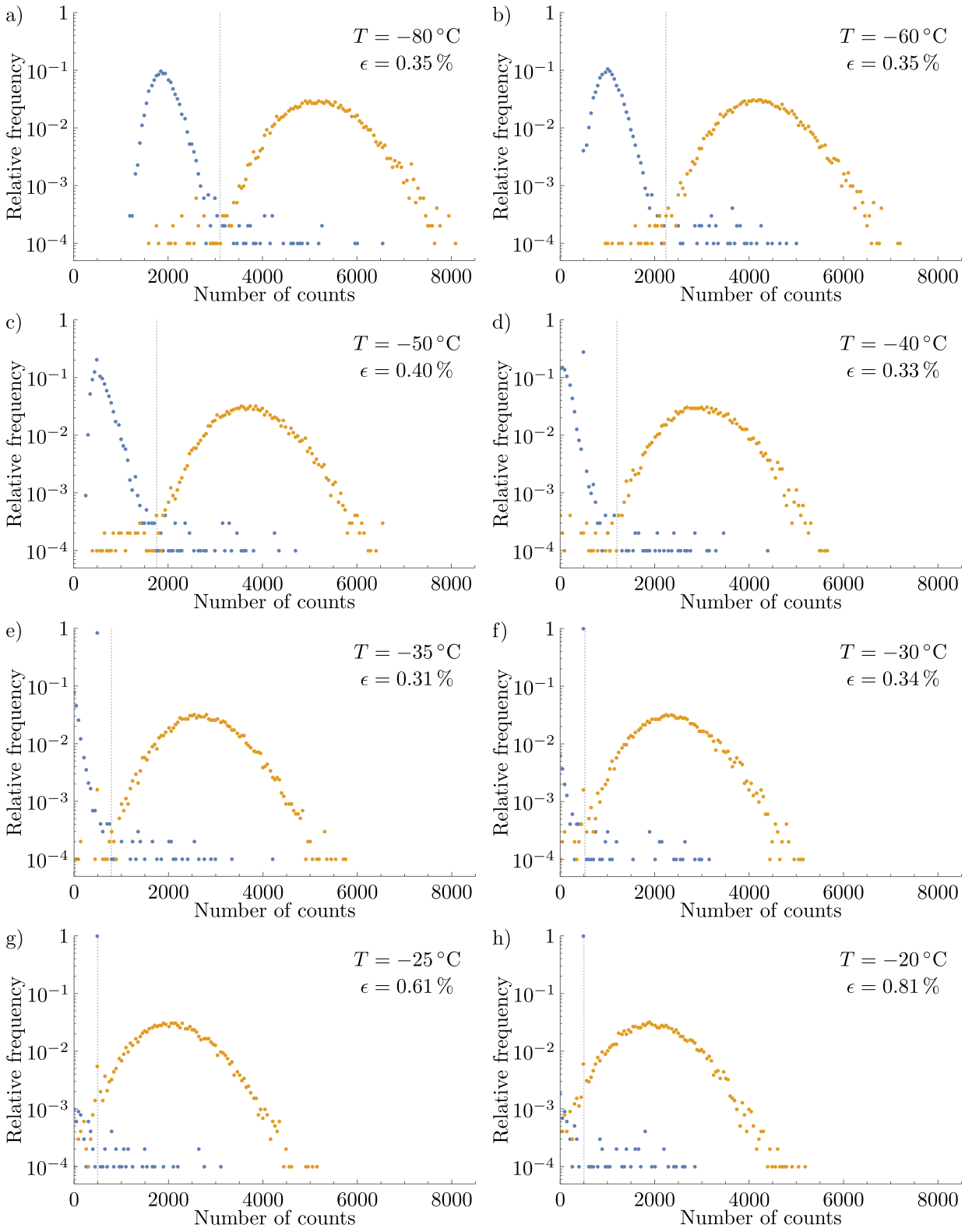

Figure 3.10: Histograms for the detection of a single ion prepared in the dark state (blue) and in the bright state (orange). 50 data points are binned together horizontally for reasons of clarity. The dashed grey lines indicate the threshold value to decide between the dark state and the bright state. The temperature T of the camera and the SPAM error ϵ at that temperature are stated in each figure a) - h).

The measurement campaign presented here was the reason why we aimed for a camera temperature of $-35\,^{\circ}\mathrm{C}$ in all of the following measurements. Although the SPAM error is almost identical for $T = -35\,^{\circ}\mathrm{C}$ and $T = -30\,^{\circ}\mathrm{C}$, we were afraid that the threshold value is too close to 500 counts for $T = -30\,^{\circ}\mathrm{C}$, so it could cause problems at some point. At a camera temperature of $-35\,^{\circ}\mathrm{C}$, we are able to achieve a SPAM error $\varepsilon \approx 0.3\,\%$ comparable to a state detection using a PMT. We find the achievable trigger rate of $200\,\mathrm{s}^{-1}$ reasonably fast. If we are willing to endure a higher SPAM error in the future, it is absolutely possible to operate the camera at a higher temperature with a higher trigger rate.

It is important to note that some of the camera's parameters such as the EM gain and binning area size are different in this measurement compared to other measurements presented in this thesis. Also we did not account for the temperature transient. It could very well be that with a higher EM gain, a different binning area size and taking into account the temperature transients, the achievable trigger rate could be raised far above $200\,\mathrm{s}^{-1}$, especially when we were to allow for a higher SPAM-error.

3.5 Sensor cleaning

In a CCD image sensor, incident photons are converted into electrons which are stored in potential wells until they are shifted into an adjacent potential well or into the input stage of a readout circuit. This makes it possible to implement techniques such as hardware binning that are of great use for our experiments. The downside of this operating principle is that unwanted charges that were generated for example by noise processes or cosmic radiation also stay in the individual pixels until they are read out. Especially important for our experiment is that during cooling and state preparation, the ions scatter light which falls onto the CCD sensor and generates charges. When the charges generated during the preparation process are superimposed with the charges collected during the detection interval, it is very hard or impossible to tell in which state the ion has been. It is therefore crucial to exclusively read out the charges that were generated during the detection interval.

There are two basic principles available that fulfill this requirement:

- Block the light during state preparation using a mechanical shutter.
- Remove all the charges from the sensor before starting the detection process.

The *Andor iXon Ultra 888 UVB* has a built-in mechanical shutter that can be operated using an external TTL signal. If we were to use this shutter to block the light scattered during state preparation, the requirements would be to open 200 times per second for $400\,\mu\mathrm{s}$ each, over a million times every day. Furthermore, the delays for opening and closing the shutter must be constant for

every trigger signal. We thought these requirements to be unreachable and have never tried out to what extent the camera could fulfill them. Even if the timing requirements could be fulfilled, we would still be afraid that the shutter introduces vibrations to the experimental setup and would break after a short period of time due to the high number of releases.

For the reasons states above, we do not use a mechanical shutter but instead remove the charges from the CCD sensor before shining in the detection laser beam. The camera has a built-in feature that runs so-called *keep clean cycles* when the camera is in idle state or waiting for a trigger signal (c.f. [84]). The keep clean cycles make sure that all the charges in the CCD sensor are shifted gradually into the readout circuit. One of these cycles consists of one or more shifts in the vertical direction followed by 1024 shifts in the horizontal direction. When a trigger signal arrives at the camera while a keep clean cycle is running, that cycle is completed before the image is taken. Since we do not know at what moment the keep clean cycle has started relative to the trigger signal, a random delay is introduced between the trigger signal and the begin of reading out the image (see figure 3.11). We measured the minimum and maximum delay between the rising edge of the trigger signal and the fire signal using an oscilloscope. The results are shown in table 3.2.

The *Fire* output of the camera tells us when the image is taken and the vertical shift operations stand still. We have to make sure that the ion is exposed to the detection laser beam during this time slot. If the ion is illuminated while vertical shift operations take place, the generated charges would end up shifted by one or more rows and end up in a binning area of a different ion in the worst case.

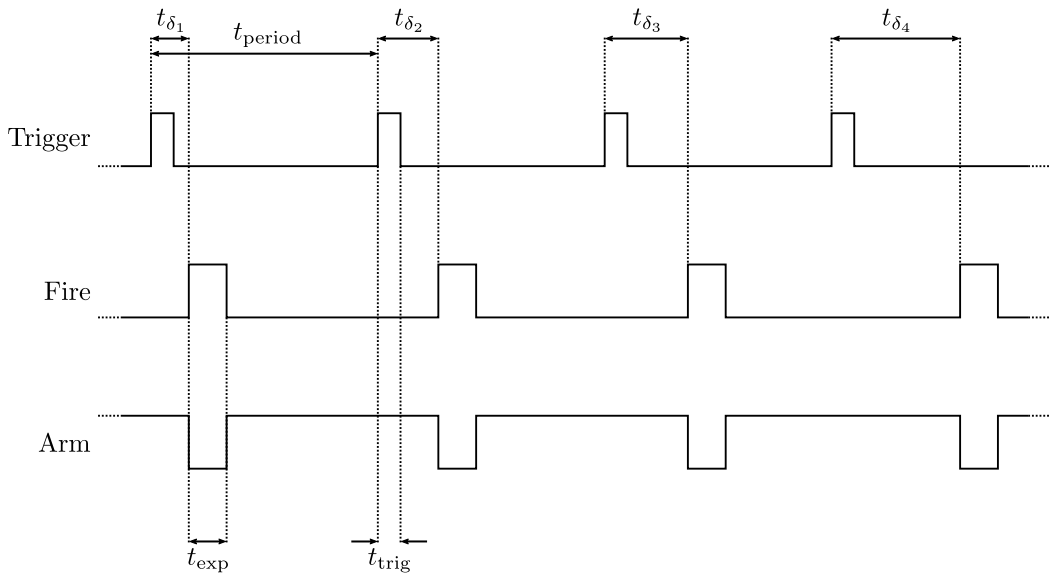

Figure 3.11: Schematic illustration of variable delays t_{δ_i} between trigger pulses of length t_{trig} and the start of the exposure of duration t_{exp}. The time between two trigger pulses is t_{period} and constant.

Readout rate	Minimum delay	Maximum delay
1 MHz	1.09 ms	2.56 ms
10 MHz	110 µs	240 µs
20 MHz	57 µs	131 µs
30 MHz	38 µs	95 µs

Table 3.2: Minimum and maximum delay between trigger pulse and start of the exposure for different readout rates.

For the following considerations, we will name the minimum delay between trigger and fire pulse $t_{\delta_{\min}}$ and the maximum delay $t_{\delta_{\max}}$. The detection time $t_{\text{det}} = 400\,\mu\text{s}$ is the length of the time slot during which the detection laser beam is applied to the ions. In order to ensure that the ions are only illuminated while the fire-output is high, we have to wait at least for $t_{\delta_{\max}}$ after the trigger pulse before we apply the detection laser beam. To prevent the readout process from starting while the detection laser beam is still on, the exposure time setting in Andor Solis must be extended to $t_{\text{det}} + t_{\delta_{\max}} - t_{\delta_{\min}}$. In addition to the previously discussed delays, we also have to take into account that a certain amount of keep clean cycles have to be completed to ensure that all of the charges generated during state preparation are shifted outside of all the relevant binning areas. The exact amount of time needed to achieve this depends on the positions and sizes of the binning areas and is also subject to the variation discussed in the context of trigger delay. When not enough time is spent for the keep clean cycles to empty the relevant pixels, the measured data is shifted towards a higher number of counts (see figure 3.12).

For this measurement, the size of the binning areas was 31×31 pixels. Only one dummy area was used above the ion to determine the baseline. The EM gain was set to 300. The vertical shift speed was 1.13 µs and the readout rate was 10 MHz. The camera temperature was set to $-80\,^{\circ}\text{C}$ and the temperature transient was not taken into account.

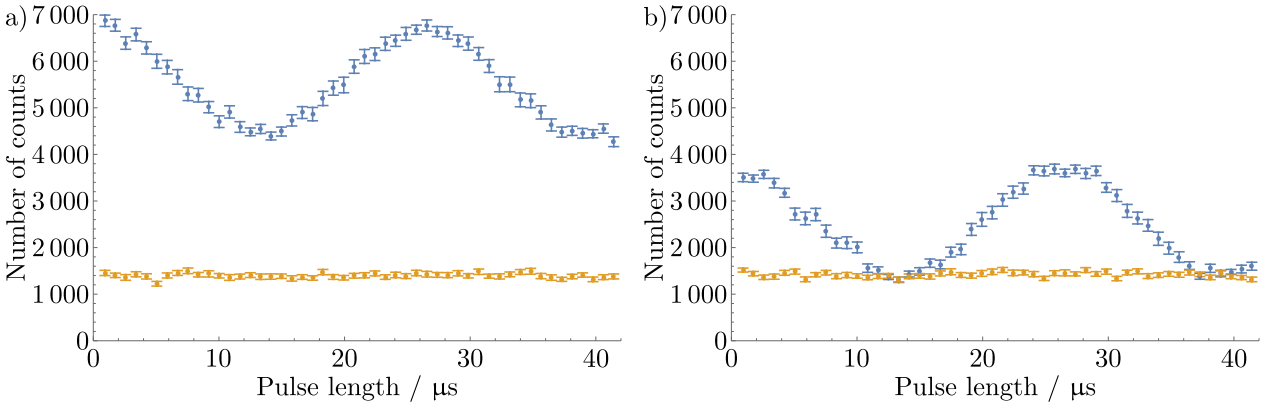

Figure 3.12: Rabi oscillations on the $|2,0\rangle \leftrightarrow |1,-1\rangle$ transition. a) No delay between state preparation and trigger pulse, b) 3 ms delay. Blue: binning area with ion, orange: empty binning area for baseline. Error bars indicate the standard deviation.

The gap between the oscillating signal and the baseline in figure 3.12 a) is caused by residual charges from the state preparation. When waiting for around 3 ms (figure 3.12 b)), enough keep clean cycles have completed to empty the binning area of the ion, so that the gap vanishes and the oscillating signal goes down to the baseline level.

In a simple model, one could argue that the measured number of counts is just shifted by a constant value which can be subtracted afterwards. Here, we briefly want to give reasons why this would not work. While it seems as if the shift were constant when the measured number of counts is averaged over 100 experiments as in figure 3.12, this shift is not constant from shot to shot for multiple reasons.

First of all, both the number of photons scattered during state preparation and during detection have a probability distribution. This alone would increase the overlap between the histograms for ions in the dark state and in the bright state, which by consequence would result in an increased SPAM error.

Another reason why simply subtracting an offset does not work is that the shift quantitatively depends on the number of scattered photons during the state preparation of the ions, which in turn depends on the state in which the ion was previously. If the ion has been found in the bright state during the previous detection, the shift during the next state preparation sequence can be maximal. However, if the ion has been found in the dark state, it has to be optically pumped into the bright state during the next state preparation. It is completely random how long this pumping process takes for a single preparation event. Therefore, we cannot tell with certainty how many photons will be detected when the state preparation laser beam is switched on for a given time.

The previously discussed behaviour of the keep clean cycles apply only when the *Frame Transfer* option is disabled in Andor Solis. When frame transfer is enabled, the camera takes care that the keep clean cycles remove all the charges from the sensor once before the first trigger pulse is accepted. After that, the keep clean cycles only work on the readout register to keep it free of charges. No vertical shifts are applied to the image or storage area of the CCD sensor. This results in an exposure time that is equal to the time between two trigger signals. In this mode of operation, the delay between trigger pulse and fire pulse is found to be much smaller and with less variation than when the frame transfer option is disabled. We measured the delay to be between 160 ns and 220 ns. We can now precisely control when the sensor should be cleaned by triggering the camera. This generates an image that can later be discarded. After this first image is read out, we shine in the detection laser and trigger the camera a second time to read the actual image of interest.

3.6 Timing

Although the *Frame Transfer* mode comes with small and deterministic delays, caution still has to be paid when triggering the camera. In the following, we will discuss the correct triggering procedure in frame transfer mode. The *Andor iXon Ultra 888 UVB* has several inputs and outputs available. Among these are the *trigger* input and the *arm* and *fire* outputs. In figure 3.13, a simplified timing diagram is shown.

In the diagram, the time between two trigger pulses is t_{period} and constant. The length t_{trig} of the trigger pulse does not matter since the camera reacts to the rising edge of the trigger pulse. For convenience, we usually set $t_{\text{trig}} = t_{\text{det}}$ to simplify troubleshooting. The detection time t_{det} specifies the delay after the camera receives the trigger signal and before the readout process is started. The *fire* output being high indicates this waiting period. This is the time when the detection laser beam is switched on. When a valid trigger signal is received, the *arm* output becomes low and stays this way until the waiting period and the subsequent readout have finished. While the arm output is low, incoming trigger signal will have no effect. It is highly recommended to check the logic levels of *trigger*, *fire* and *arm* with an oscilloscope after every change in the timings of the experiment or in the camera settings.

Getting the timing of the trigger signals right is not the only thing to do before starting a measurement. The total amount of trigger pulses in the following measurement sequence also has to be stated in advance. To run a measurement sequence with the camera, the acquisition mode is set to *Kinetic*. The *Delay of Exposure Period* is set to t_{det} and the *Kinetic Series Length* is set to the number of expected trigger signals. For most of the measurements discussed in this thesis, the

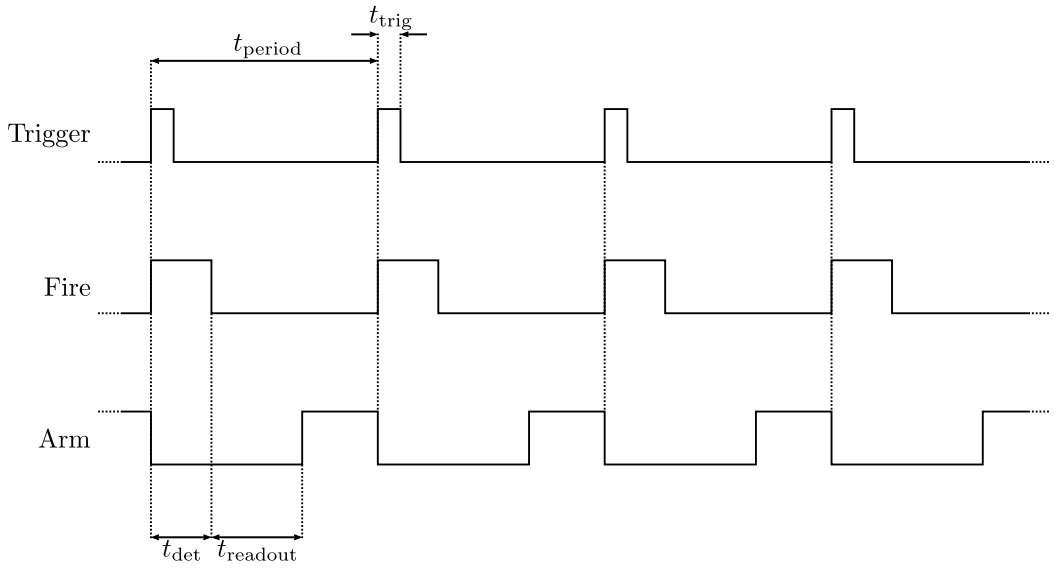

Figure 3.13: Schematic illustration of a trigger sequence in frame transfer mode.

kinetic series length is two times the number of experiments, because every other image is only used to clean the sensor and discarded later.

When the kinetic series length is set too low, the camera would stop taking data too early, resulting in incomplete measurements and data loss. When the kinetic series length is set too high, the camera would still expect more trigger pulses after the experiment has completed. The data taken during a kinetic series measurement is saved into a file only after the whole kinetic series has completed. When the series length is set correctly but the trigger pulses arrive too fast, it can happen that the arm output is still low when a trigger pulse arrives. This results in the camera expecting further trigger pulses after the experiment has completed. These considerations make it obvious that the correct kinetic series length as well as the correct trigger timing have to be used.

4 Measurements with ions

In this chapter, we will present experiments that were performed to compare the performance of ion state detection between a PMT and an EMCCD camera. We will compare the results for the two different detectors used and discuss possible error sources.

4.1 State discrimination of a single ion

Since the implementation of quantum algorithms requires the detection of an ion's state within a single detection event, we will quantify the single-shot detection efficiency by determining the fluorescence count distributions when using a PMT or an EMCCD camera for detection and compare the SPAM errors achieved by the different techniques as a measure of the quality of the detection method.

For the measurement with the EMCCD camera as the detector, we used an EM gain of 1000, a vertical shift speed of 0.6 µs, a readout rate of 30 MHz, a horizontal binning of 33 pixels, a vertical binning of 32 pixels and one dummy area below and one above the ion's binning area. The camera temperature was set to $-35\,^{\circ}\mathrm{C}$ and for the data shown in figure 4.1 b), the temperature transient was not taken into account.

We prepared a single ion 10^5 times in the dark state and in the bright state before applying the detection laser beam. The histogram representation of the measurements is shown in figure 4.1. The fitted lines are described by a Poissonian distribution (expected value λ, number of occurrences k) of the form

$$P_\lambda(k) = \frac{\lambda^k}{k!} e^{-\lambda} \tag{4.1}$$

for detection with the PMT, which is slightly modified to account for the EM gain G and the binning of datapoints b for detection with the EMCCD camera, resulting in

$$P_{\lambda,b,G}(k) = \frac{b}{G} \frac{\lambda^{k/G}}{(k/G)!} e^{-\lambda}, \tag{4.2}$$

where the prefactor $\frac{b}{G}$ is required for normalization. The best fits for the histograms measured with the PMT yield $\lambda_{\mathrm{PMT,bright}} = 45.838(13)$ and $\lambda_{\mathrm{PMT,dark}} = 1.5301(20)$ with a coefficient of

determination $R^2_{\mathrm{PMT,bright}} = 0.9996$ and $R^2_{\mathrm{PMT,dark}} = 0.9997$. The fitted parameters for the data taken with the EMCCD camera are $\lambda_{\mathrm{Cam,bright}} = 19.85(10)$, $G_{\mathrm{bright}} = 479.0(2.4)$, $\lambda_{\mathrm{Cam,dark}} = 0.856(6)$ and $G_{\mathrm{dark}} = 897(5)$ with a binning value $b = 100$ fixed. The resulting coefficients of determination are $R^2_{\mathrm{Cam,bright}} = 0.999$ and $R^2_{\mathrm{Cam,dark}} = 0.9995$. For fitting the camera data, the counts at and below 500 were removed.

We notice that the fit values for the EM gain G are different for ions in the bright state and in the dark state and also both values do not match the set value of 1000. This is a result of the relatively simple model that we used to obtain equation 4.2 and which consists only of a linear gain factor G and binning of datapoints b. The nonlinear characteristic of the EMCCD camera was not taken into account. Therefore, the fitted parameter G is to be interpreted as an effective gain averaged over the histogram.

For the detection with the PMT, we find a minimal SPAM error of $\epsilon_{\mathrm{PMT}} = 0.28\,\%$ for a threshold value of 10. For the detection with the EMCCD camera, we find a minimal SPAM error of $\epsilon_{\mathrm{Camera}} = 0.36\,\%$ for a threshold value of 4284. The camera has a slightly higher SPAM error, but it is still on the same order of magnitude as the PMT. Compared to the room-temperature experiment that our group operates at PTB and which has a SPAM-error of 1.5 % [22], both detection methods used here perform much better.

Some differences are obvious between figure 4.1 a) and b). The detected number of counts is much lower for detection with the PMT than for detection with the EMCCD camera. For an ion prepared in the bright state, we obtain 45.642(23) counts for detection with the PMT and 9568(7) counts for detection with the EMCCD camera. For an ion prepared in the dark state, we obtain 1.635(7)

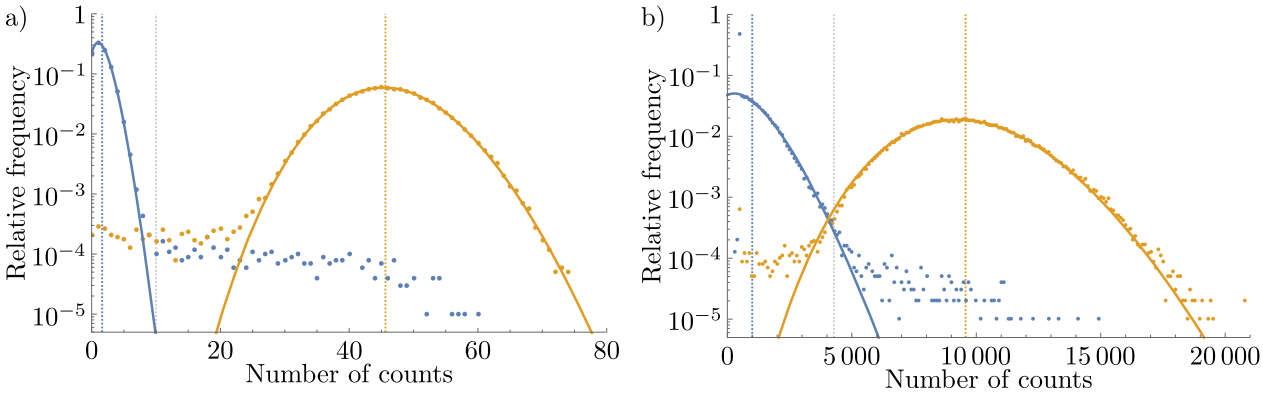

Figure 4.1: Histograms for the detection of a single ion prepared in the dark state (blue) and in the bright state (orange). The dashed grey lines indicate the threshold value to decide between the dark state and the bright state. The blue and orange dashed lines indicate the average number of counts for preparation in the dark and bright state, respectively. Detection with a) PMT, b) EMCCD camera (100 counts binned together horizontally for clarity). Points: experimental data, solid line: Poissonian fit.

counts for detection with the PMT and 998.9(2.4) counts for detection with the EMCCD camera. Here the numbers in brackets indicate the standard deviation.

A photon hitting the PMT produces one count with a probability given by its quantum efficiency. We operate with a laser power of around the ion's saturation intensity which results in half of the counts that can maximally be achieved (c.f. section 2.6.2). In contrast to the PMT, the number of counts measured with the EMCCD camera is given by a nonlinear characteristic (c.f. section 3.3). Therefore, and due to the high EM gain setting, the measured number of counts is much higher for the EMCCD camera than for the PMT.

When we look at the histograms measured with the PMT (figure 4.1 a)), we see that there is a region between approximately 10 and 20 counts where both of the histograms for ions in the dark state and in the bright state are flat. When we compare that with the data taken with the EMCCD camera (figure 4.1 b)), we notice that such a region where both histograms are flat is nonexistent. Instead, the falling slope of the histogram for ions in the dark state intersects the rising slope of the histogram for ions in the bright state. This means that the count distributions are broadened for the detection with the EMCCD camera compared to a detection with a PMT. We associate this broadening with electronic noise processes in the camera. This noise is the reason why we need the EM gain in the first place to separate the two histograms. Without any additional noise (compared to the PMT) and without any EM gain, it is expected that the data taken with the EMCCD camera should look like the data taken with the PMT since both detectors have roughly the same quantum efficiency.

Why the flat parts of the histograms are present at all can have different reasons. The flat part on the left side of the histogram for an ion in the bright state is most likely due to imperfect circular polarization of the cooling and detection laser beams (c.f. section 4.1.1). When a finite amount of linear polarization is present in those laser beams, the ion can be off-resonantly excited to states that are not part of the closed-cycle cooling and detection transition. From these excited states, the ion can then decay into a state different from the bright state, therefore reducing the measured number of counts.

The relatively long flat tail on the right side of the histogram for an ion in the dark state results from off-resonant excitation of the dark state which is called optical depumping. Even with perfectly aligned polarization, this effect is unavoidable. Also, the population that was not correctly prepared to the bright state could end up in an undesired state when the microwave transfer pulses (c.f. figure 2.2) are applied to the trap.

4.1.1 Imperfect polarization

Here, we briefly provide evidence for the imperfect polarization of the cooling and detection laser beams as a major contribution to the SPAM error. When we assume that the polarization of our laser beams has a linear component, the ion can leave the closed-cycle transition used for Doppler cooling and detection. After absorbing a linearly polarized photon and spontaneously emitting a circularly polarized photon, the ion can end up in either the $|2,1\rangle$ or $|1,1\rangle$ state. When the ion decays to the $|2,1\rangle$ state, it can still be off-resonantly excited by the cooling laser beam. However, the probability to excite the $|1,1\rangle$ state with the cooling laser beam is relatively low, so the ion can get stuck in this state for some time and therefore lead to a reduced number of counts on the detector. To depopulate the $|1,1\rangle$ state faster, we can shine in the repumper laser beam. The repumper transition does not feature a closed cycle and always allows the ion to decay back to either the $|1,1\rangle$ state or the $|2,1\rangle$ or $|2,2\rangle$ state.

The experiment consists of three parts with different laser beams present at different times. Each experiment was repeated 10^5 times. In the first experiment, we only use the Doppler cooling laser during the state preparation and only the detection laser during detection. This gives us a basis for the next experiments. For a second experiment, we also apply the repumper laser beam during preparation, but leave the detection process as before. We expect that this results in fewer events with a low number of counts. For the final experiment, we apply the repumper laser beam both during preparation and during detection. This allows the ion to almost always scatter photons independent of its state and should result in an almost perfect Poissonian distribution. The results of the three measurements are shown in figure 4.2.

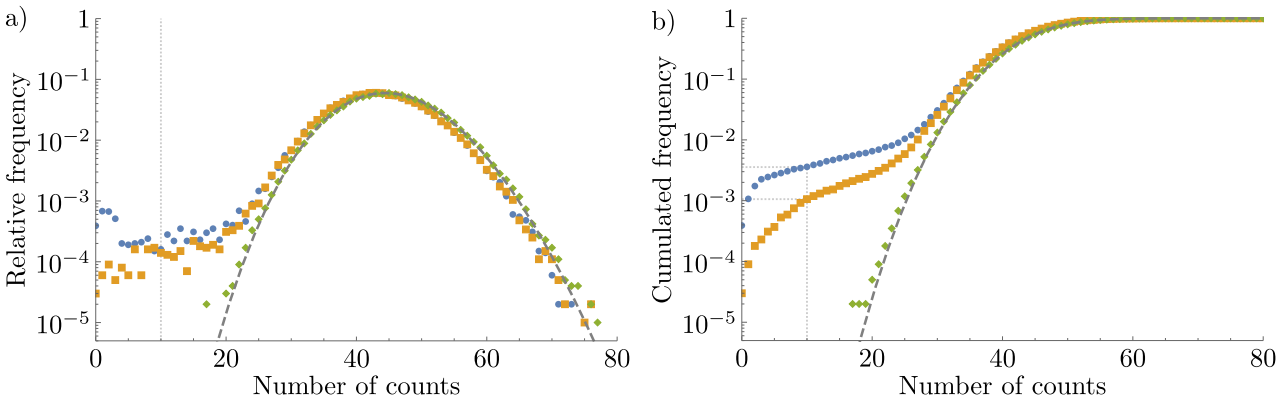

Figure 4.2: Count distributions for a single ion prepared in the bright state with subsequent detection. The different colors indicate different laser beams being switched on during preparation and detection. a) Probability distribution, b) integrated probability distribution. Blue: no repumper at any time, orange: repumper on during preparation, green: repumper on during preparation and detection. An ideal Poissonian distribution is indicated in grey for comparison. The vertical lines at 10 counts indicate the threshold value to decide between the dark state and the bright state.

With only the Doppler cooling laser on during the preparation, we see a peak in figure 4.2 a) at a low number of counts. This points out that the ion is far from being perfectly prepared to the bright state. To quantify the quality of the preparation, we proceed similar to the SPAM-error estimation. We set a threshold value, so that all detection events with ≤ 10 counts are interpreted as a dark ion (see figure 4.2 b)). For comparison, we included a perfect Poissonian distribution in figure 4.2. The estimated value of this distribution is set to the average number of counts for the experiment performed with the repumper laser beam being on permanently, which is approximately 44.9. Note that the green histogram is shifted approximately 1.5 counts to the right with respect to the orange histogram, because the repumper beam being switched on during the detection process leads to an increased amount of fluorescence photons from the ion and to a larger amount of stray light from the trap surface. We determine the number of experiments that would be interpreted as detection of a dark ion for the three different preparation schemes and compare with the theoretical value for a perfect Poissonian distribution (see table 4.1).

From these values we conclude that the ion sometimes decays to a state that does not effectively scatter photons from the cooling and detection laser beam. The preparation can be improved by a factor of three to four in terms of the SPAM error when we apply the repumper laser beam during the preparation process to depopulate the $|F = 1\rangle$ states. The remaining 0.1 % originate from the ion leaving the closed-cycle transition during the detection process. If we shine in the repumper laser beam also during the detection process, we basically enforce the ion to always scatter photons, either from the detection laser or from the repumper. Deviations from the ideal distribution can be caused by the $626 \rightarrow 313$ nm cavity going out-of-lock or higher order effects where the ion gets excited by the linear part of the polarization and decays by emitting a σ^- polarized photon multiple times in a row. Shining in the repumper laser beam during the detection has no practical meaning for real experiments. It was done here to quantify the baseline error resulting from our laser system and it turned out it is smaller than we need to take care about.

We compare this value with a synthetic dataset which represents an ion with a perfect Poissonian count distribution. We set the average value of this distribution to the average value of the previous measurement which is $\lambda = 44.9$. We can calculate that for a perfectly prepared ion with an average number of counts of 44.9, the SPAM error would be in the 10^{-10} range, which explains why we did not detect any event with less than 10 counts in 10^5 experiments. We conclude that the SPAM error in our experiment could be improved if we spend some time in getting

Preparation scheme	**SPAM error**
No repumper	0.36 %
Repumper during preparation	0.1 %
Repumper always on	0 %
Theoretical optimum	$4 \cdot 10^{-8}$ %

Table 4.1: Error rate when detecting an ion after preparation in the bright state.

the polarization of our laser beams right which would lead to a better state preparation. In the present experimental setup, the cooling and detection laser beam passes through a polarizer and waveplates placed on rotatable and tiltable mounts that should allow us the set any polarization. We presume that spatially inhomogeneous dichroic effects on the cryogenic viewports could change the polarization of the laser beam in a way which we cannot compensate from outside the vacuum chamber.

Note that in this section, we only considered the error in preparing and detecting the bright state. When detecting an ion in the dark state, the optical depumping effects are unavoidable and would result in a SPAM error worse than when only considering ions in the bright state. All in all, we assign 0.1 % SPAM error to the imperfect polarization and 0.2 % to optical depumping effects when detecting with the PMT. When the EMCCD camera is used for detection, additional errors due to electronic noise processes are also present and increase the SPAM error.

4.1.2 Detection time

Another important factor for the SPAM error is the time during which the detection laser beam illuminates the ion. On the one hand, if the detection time is chosen too low, not enough photons will be detected to separate the histograms of ions in the dark state and in the bright state. On the other hand, if the detection time is too high, depumping effects change the ion's state from dark to bright or vice versa. We have to find a compromise of the detection time that results in a minimal SPAM error. This measurement was performed with a single ion prepared in the bright state and in the dark state alternatingly 10^4 times each before applying the detection laser beam. The fluorescence light was detected with the EMCCD camera with a readout rate of 30 MHz, a vertical shift speed of 0.6 µs, an EM gain of 300, a binning area size of 38 pixels in the horizontal direction and 32 pixels in the vertical direction and with one dummy area below and one above the ion's binning area. The camera temperature was set to −60 °C and we did not account for the temperature transient. In figure 4.3, the histograms and the resulting SPAM error are shown for different detection times. It is clearly visible how the separation of the two probability distributions increases for increasing detection times, but the "tails" on the sides of the main peaks are also growing due to depumping effects. The lowest SPAM error can be achieved with detection times in the range of 350 to 400 µs. It is hard to tell what the uncertainty of the determined SPAM error is. When we run the same measurement multiple times, we usually get SPAM errors that do not differ by more than 0.05 %. We decide to use a detection time of $t_{\mathrm{det}} = 400\,\mu\mathrm{s}$ for the experiments presented in this thesis.

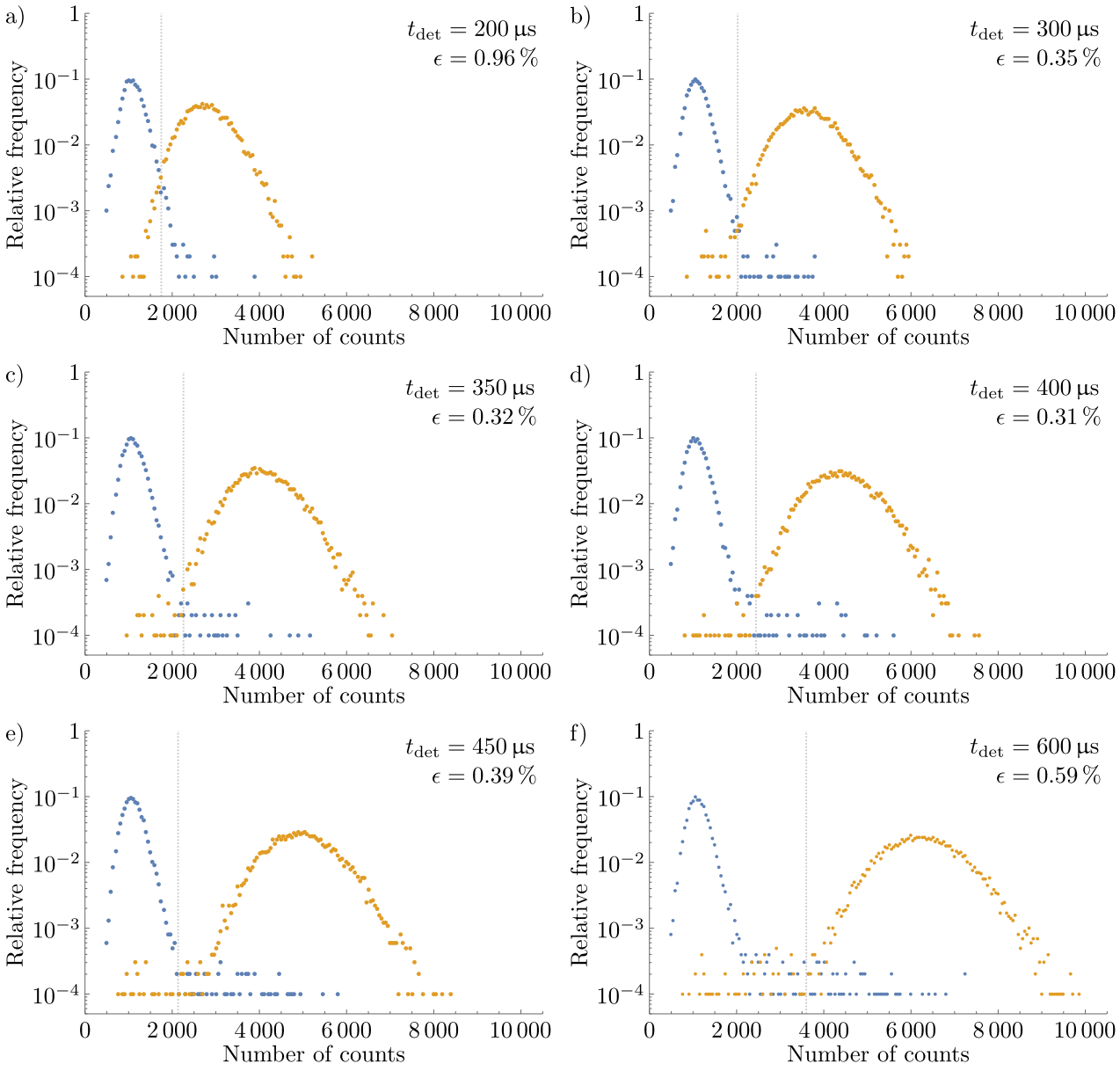

Figure 4.3: Histograms for the detection of a single ion prepared in the dark state (blue) and in the bright state (orange). 50 data points are binned together horizontally for reasons of clarity. The dashed grey lines indicate the threshold values to decide between the dark state and the bright state. The detection time t_{det} and the resulting SPAM error ϵ are stated in each figure a) - f).

4.2 Single-ion Rabi oscillations

In this section, we demonstrate that the contrast of the fluorescence signal of an ion in the dark state and in the bright state depends on the used detector. A PMT cannot distinguish where a photon arrives on its active area, making it sensitive to stray light from the trap surface. Binning on the EMCCD detector allows us to define which parts of the detector should be evaluated and therefore can help to suppress all stray light that fell on pixels outside of the ions' binning areas. The suppression of counts originating from stray light can be seen in figure 4.4.

In this experiment, we prepared an ion in the bright state and transferred it to $|\uparrow\rangle$ using a microwave π-pulse. We then apply a microwave pulse resonant with the field-independent qubit transition for a variable time t. Afterwards, we apply a series of microwave π-pulses to transfer the population in $|\uparrow\rangle$ to the bright state and the population in $|\downarrow\rangle$ to the dark state. Finally, we apply the detection laser beam. We repeat the experiment 500 times for each pulse length. We probe 100 different pulse lengths between 0.05 µs and 10.05 µs. The whole experiment was performed one time with the PMT (figure 4.4 a)) and one time with the EMCCD camera (figure 4.4 b)) as the detector. For the detection with the EMCCD camera, we used a readout rate of 30 MHz, a vertical shift speed of 0.6 µs, binning areas with 33 pixels in the horizontal direction and 30 pixels in the vertical direction, one dummy area below and one above the ion's binning area, a camera temperature of −35 °C and we took care of the temperature transient by running the experiment twice in a row.

When no light is falling on the PMT, the measured number of counts is basically zero. In the datasheet [76] the typical dark count rate is given to be $50\,\mathrm{s}^{-1}$, meaning that only 0.02 counts

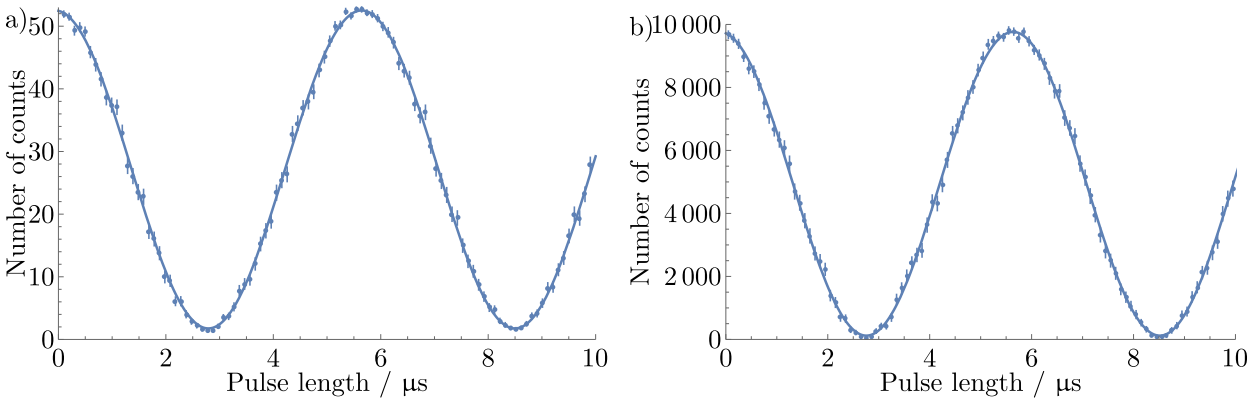

Figure 4.4: Rabi oscillations of a single ion on the field-independent qubit transition with different detectors used. a) PMT, b) EMCCD camera. The datapoints with error bars indicate the average value of 500 measurements and the standard deviation. The solid line represents a sinusoidal fit. For detection with the camera, the average number of counts measured with the shutter closed was subtracted.

are measured on average during the detection interval. In contrast to the PMT, the EMCCD camera always reads a finite number of counts even in complete darkness (c.f. section 3.3). For a fair comparison, we measure these background counts to be 925.0(2.8) while the camera's shutter is closed. This value is subtracted from the counts measured with the camera during the real experiment.

We fit a sinusoidal function of the form

$$N(t) = A \cdot \sin\left(\frac{\pi}{t_\pi}t + \varphi\right) + B \tag{4.3}$$

to the data taken with the PMT and with the EMCCD camera. For the PMT data, the best fit yields $A_{\mathrm{PMT}} = 25.38(12)$, $B_{\mathrm{PMT}} = 27.13(9)$, $t_{\pi,\mathrm{PMT}} = 2.854(4)\,\mu\mathrm{s}$ and $\varphi_{\mathrm{PMT}} = 1.640(10)$. After subtracting the background counts, the best fit for the camera data yields $A_{\mathrm{Cam}} = 4822(21)$, $B_{\mathrm{Cam}} = 4941(15)$, $t_{\pi,\mathrm{Cam}} = 2.880(4)\,\mu\mathrm{s}$ and $\varphi_{\mathrm{Cam}} = 1.704(9)$. We calculate the contrast K of the oscillation signal using $K = \frac{\mathrm{Max}-\mathrm{Min}}{\mathrm{Max}+\mathrm{Min}} = \frac{A}{B}$, where we used the fit parameters to calculate the maximum and minimum values. We find the contrast to be $K_{\mathrm{PMT}} = 0.935(5)$ for the PMT and $K_{\mathrm{Cam}} = 0.976(5)$ for the EMCCD camera, respectively.

We see already by looking at figure 4.4 that the lowest datapoints are much closer to zero for detection with the EMCCD camera than with the PMT. This observation was quantitatively confirmed by calculating the contrast K. The improved contrast is a consequence of the EMCCD camera using hardware binning and could help in the future to achieve lower error rates.

4.3 State discrimination of two ions

In this section, we present the performance differences in determining the ions' state with a PMT and an EMCCD camera, respectively. Starting at two ions, it is expected that the EMCCD camera can unleash its potential by detecting the fluorescence light of each ion independently. To determine the single-shot detection performance for two ions with the EMCCD camera and compare it to a PMT, we conducted a series of experiments. We prepared the two ions 10^5 times in three different ways before we apply the detection laser beam. All experiments start by optical pumping the ions in the bright state $|2,2\rangle$. From here on we apply one out of three different microwave pulse sequences:

1. transfer the population from $|2,2\rangle$ to $|\uparrow\rangle$.
2. transfer the population from $|2,2\rangle$ over $|\uparrow\rangle$ to $|\downarrow\rangle$.

3. transfer the population from $|2,2\rangle$ to $|\uparrow\rangle$ and apply a $\frac{\pi}{2}$ pulse resonant with the qubit transition to prepare a superposition state $\frac{1}{\sqrt{2}}(|\uparrow\rangle + |\downarrow\rangle)$.

After the preparation sequence, a series of shelving pulses is applied to transfer the population from $|\uparrow\rangle$ to the bright state and the population from $|\downarrow\rangle$ to the dark state.

For each of the three preparation schemes described above, the experiment was conducted using different detection methods as follows:

a) using the PMT to detect the collective fluorescence light of both ions.

b) using the EMCCD camera with a large binning area for both ions together as a direct comparison to the PMT.

c) using the EMCCD camera with separate binning areas for each ion.

For the detection methods with the EMCCD camera, we used a readout rate of 30 MHz, a vertical shift speed of 0.6 µs, two dummy areas below and one above the ions' binning areas, a camera temperature of −35 °C and we took care of the temperature transient by running the experiment twice in a row. The binning area size was set to 30×30 pixels for the dummy areas and for the ions' binning areas in c). For method b), the large binning area for both ions together has 63 pixels in the vertical direction, which is the height of two normal binning area plus the gap of 3 pixels in between.

The results of the different detection methods are shown in figure 4.5. In the histograms in figure 4.5 a) and b), we can clearly recognize peaks at three distinct positions. These peaks are the photon count distributions to find 0, 1 or 2 ions in the bright state. When the ions are prepared in the superposition state $\frac{1}{\sqrt{2}}(|\uparrow\rangle + |\downarrow\rangle)$, the wavefunction of each ion will collapse independently during the detection. We then expect to find "0 ions bright" in 25 %, "1 ion bright" in 50 % and "2 ions bright" in 25 % of the measurements. We set threshold values at $t_1 = 20$ and $t_2 = 80$ counts for the detection with the PMT. From the number of counts C we conclude the number of bright ions using the threshold values. Here $0 \leq C \leq t_1$ is interpreted as "0 ions bright", $t_1 < C \leq t_2$ is interpreted as "1 ion bright" and $C > t_2$ is interpreted as "2 ions bright". For the detection with the EMCCD camera using a single large binning area, the threshold values are set to $t_1 = 6\,000$ and $t_2 = 18\,000$. The frequency of detecting 0, 1 or 2 ions bright is shown in table 4.2 for detection with the PMT and in table 4.3 for detection with the EMCCD camera using a single binning area.

The error ϵ_P for a given preparation scheme P stated in the tables in calculated by

$$\epsilon_P = \frac{1}{2}\sum_{i=0}^{2} |M(i,P) - T(i,P)|\,, \tag{4.4}$$

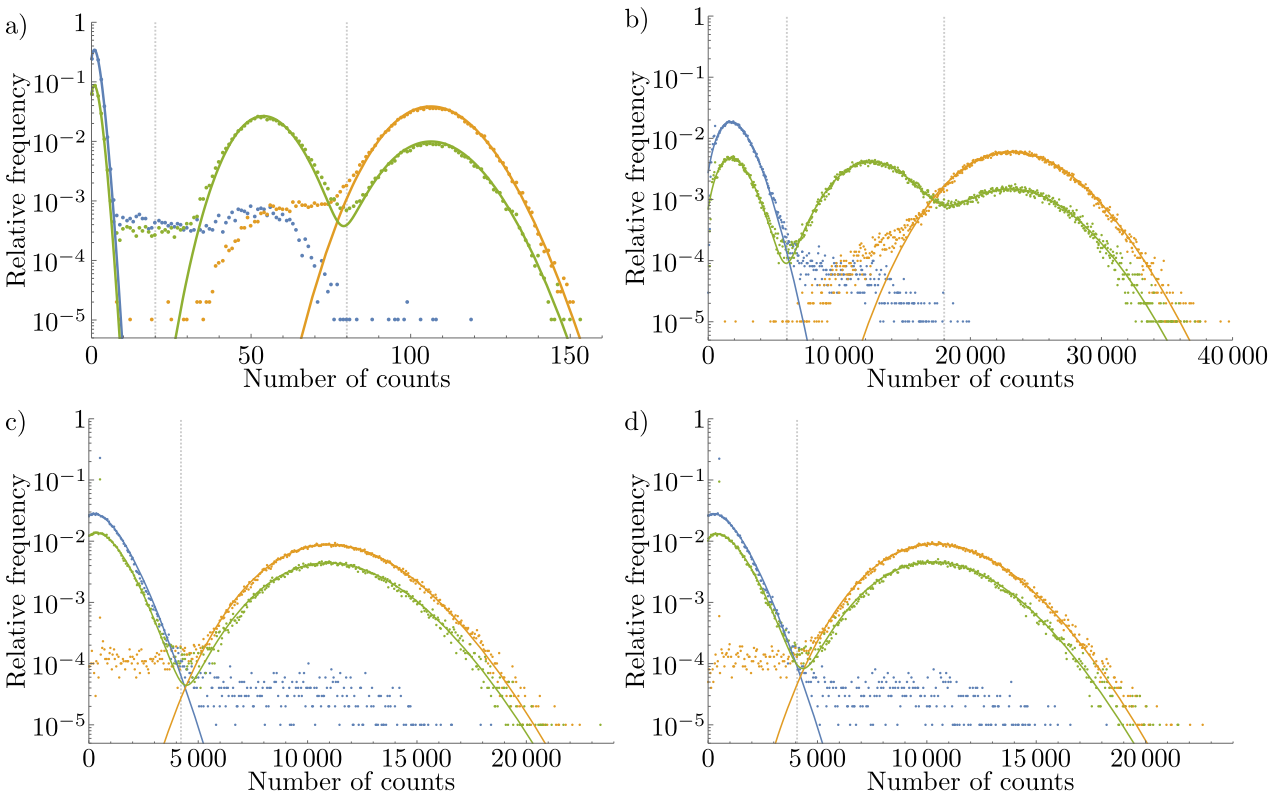

Figure 4.5: Histograms for two ions prepared in the bright (orange), dark (blue) or in a superposition (green) state detected three different ways. a) Detection with PMT, b) detection with EMCCD camera using a single large binning area, c) + d) detection with EMCCD camera using individual binning areas for each ion. c) First ion, d) second ion. The points represent the experimental data. In b) - d), 50 counts are binned together for clarity. Solid lines: Poissonian fit (datapoint at 500 counts was removed for fitting camera data). The vertical dashed lines indicate the threshold values to decide how many ions are interpreted as bright during detection.

where $P \in \{D,S,B\}$ stands for a preparation in the dark state (D), the superposition state (S) or the bright state (B) and $M(i,P)$ is the measured value to find i ions bright for preparation scheme P while $T(i,P)$ is the theoretically expected value to find i ions bright for preparation scheme P without regarding any depumping effects. The factor $\frac{1}{2}$ is a normalisation factor to prevent errors from being counted twice.

Preparation	0 bright	1 bright	2 bright	Error
Dark	97 642	2 344	14	2.358 %
Superposition	25 469	50 219	24 312	0.688 %
Bright	5	2 769	97 226	2.774 %

Table 4.2: Occurrence of detecting 0, 1 or 2 ions bright using the PMT for different preparation schemes. The ions were prepared 10^5 times in the dark state, in the bright state and in the superposition state. The stated error is the deviation from the expected count distribution.

Preparation	0 bright	1 bright	2 bright	Error
Dark	98 708	1 285	7	1.292 %
Superpostion	25 668	50 144	24 188	0.812 %
Bright	10	6 294	93 696	6.304 %

Table 4.3: Occurrence of detecting 0, 1 or 2 ions bright using the EMCCD camera with a single binning area for different preparation schemes. The ions were prepared 10^5 times in the dark state, in the bright state and in the superposition state. The stated error is the deviation from the expected count distribution.

From the measurement with the PMT, we can determine that the overlap and therefore the SPAM error is higher when detecting two ions than when only one ion is detected. We can think of at least two effects that cause a higher error in the two-ion case. The first effect is the significant overlap between the histograms of "1 ion bright" and "2 ions bright". When we look at the fitted lines which represent perfect Poissonian distributions, it is evident that the overlap between "1 ion bright" and "2 ions bright" will always be much higher than the overlap of "0 ions bright" and "1 ion bright". The overlap in this ideal case could be decreased if the average number of photons detected could be increased. Since the histograms for "1 ion bright" and "2 ions bright" are already overlapping without any errors present during preparation and detection, any additional error has a tremendous effect on the resulting SPAM error. In figure 4.5 a), we can see that a significant portion of the orange datapoints are on the left side of the threshold value at 80 counts, therefore increasing the error for both ions prepared in the bright state.

The second effect that results in an increased error is the overlap between the "0 ions bright" and the "1 ion bright" histograms. This overlap should theoretically be twice as high as in the experiments with only one ion, since there are now two ions that can independently suffer from dark-to-bright depumping. However, in this experiment the overlap is much higher than expected. If we look carefully at the blue datapoints in figure 4.5 a), we see that there is a tiny peak exactly at the position of the "1 ion bright" peak for the green datapoints. This indicates that one ion remains bright from time to time although both ions should be transferred to the dark state (c.f. section 4.4).

When we now look at the data taken with the EMCCD in a "PMT-like" configuration (figure 4.5 b) and table 4.3) with only a single binning area for both ions together, we notice some differences in the error contributions compared to the previously discussed detection with the PMT. A remarkable difference is that the error for the preparation of both ions in the dark state is approximately half of the value when using the PMT for detection and a small peak for "1 ion bright" cannot even be guessed in the histogram. This could be due to the nonlinear characteristic of the camera (c.f. section 3.3) that causes the datapoints on the left side to be squeezed together. Contrary to the error for ions prepared in the dark state, the error for ions prepared in the bright state is much higher in figure 4.5 b). This is a consequence of the broadened peaks when

detecting with the EMCCD, as already discussed in experiments with only one ion (c.f. section 4.1).

We have seen that both detection methods - the PMT and the EMCCD camera with a single binning area for both ions - suffer from SPAM error rates much higher than in experiments with only one ion. To overcome this problem, we now investigate the camera's performance when we set individual binning areas for each ion, which basically reduces the problem to the detection of a single ion. The histograms for this configuration are shown in figure 4.5 c) for the first ion and in figure 4.5 d) for the second ion. The photon count distributions are qualitatively equal to the experiments with only one ion. We can determine a threshold value to decide between the dark state and the bright state for each ion individually. For the first ion, we use a threshold value of $t_1 = 4211$ and for the second ion $t_2 = 4068$. The resulting SPAM error is approximately 0.9 % for both ions, which is almost three times higher than in the experiments with a single ion. We presume that this increased error is related to the imperfect transfer to the dark state present in this measurement campaign as seen in figure 4.5 a). Usually, the SPAM error when detecting a single ion with the EMCCD camera is the same as when individually detecting two ions, as we will also see in section 4.3.1.

From the measurements after preparing the ions in the superposition state we can further investigate the 50 % probability of one ion being bright. The probabilities for finding the ions in the dark or in the bright state are given in table 4.4. Ideally each of the four combination would have a probability of 25 % and each ion has a probability of 50 % to be found in the bright state. From the table we can see that the first ion is found in the bright state in 49.2 % of the cases and the second ion is found in the bright state in 49.8 % of the cases. Two aspects are peculiar in this measurement. The first aspect is that the probability to find each ion in the bright state is below 50 %, which indicates that the calibration of the microwave pulses is not perfect. A recalibration can be necessary when the magnetic field at the ions' positions or the temperature of the microwave amplifier which delivers the transfer pulses changes. The second aspect is that both values differ by 0.6 % which is a significant deviation given the high number of repetitions (10^5). This difference is most likely be caused by different Rabi frequencies of the two ions (c.f. section 4.4).

Detected state		
Ion 1	**Ion 2**	**Relative occurrence**
dark	dark	25.4 %
dark	bright	25.3 %
bright	dark	24.7 %
bright	bright	24.5 %

Table 4.4: Individual detection of two ions after a global $\pi/2$ pulse to prepare a superposition between $|\uparrow\rangle$ and $|\downarrow\rangle$ for each ion. Ideally all four measurement outcomes should have the same probability of 25 %. The deviation from 100 % is due to rounding.

From the measurements presented in this section, we infer that the EMCCD camera can be of great use to detect the state of individual ions with an error rate that is lower than when using a PMT to detect the state of two ions. Also the ability to detect small differences between the two ions can help to calibrate the operating parameters of the trap better than with a PMT, which basically detects the average value of the two ions. Furthermore, the detection of the state of each individual ion allows us to measure which specific ion was bright. For quantum simulations and quantum computation with many ions, it is mandatory to read out the state of each ion and not only the total number of bright ions.

4.3.1 Crosstalk

Although using individual binning areas for each ion is a promising method to reduce the SPAM error, it comes with its own error source, namely crosstalk. Crosstalk means that light emitted by one ion arrives at a pixel in a binning area of another ion, therefore producing a detection error. The amount of crosstalk generally depends on the distance between the two ions and the point spread function (PSF) of a single ion (c.f. section 2.6.1). For the reasons stated in section 3.2, the images of the ions are aligned in the vertical direction in the images taken by the camera. We now further investigate the PSF in the vertical direction. We took an image of a single ion without any hardware binning and with an exposure time of 1 second, an EM gain of 1000, a readout rate of 30 MHz, a vertical shift speed of 0.6 µs and a camera temperature of −35 °C. We then started to add up the counts measured in the individual pixels in software. In the horizontal direction, we condensed 33 pixels into one number. The vertical direction is the control variable and we investigate 151 pixels in the vertical pixel direction around the ion's position. In figure 4.6 a), the number of counts found for a given vertical pixel number is shown. Two peaks are clearly visible, originating from the "c"-shape of the ion's image. From this data we took the 30 outermost pixels on each side to calculate the background value to be 20 520. We then subtracted the background from the data, normalized it and summed over the counts in vertical direction. The cumulative number of counts in the vertical direction is then shown in figure 4.6 b).

We determined the pixel at which half of the counts are reached (indicated by the 50 % line) and define this to be the center of the ion y_0. The area of pixels which are responsible for 90 % of the counts is indicated by the lines at 5 % and 95 %. This area extends 8 pixels to the right and 12 pixels to the left with respect to y_0, meaning that 21 lines of pixels cause 90 % of the counts. This asymmetry is a consequence of the "c"-shaped ion being brighter in the top half than in the bottom half, which can also be seen in the different heights of the two peaks in figure 4.6 a). We also marked the borders of a 31 pixels high area as this is closer to the binning area size that we used in our experiments. While almost 50 % larger in size, this area has only approximately 7 % more counts in it than the smaller area previously discussed and accounts for 96.5 % of the overall counts. For larger sizes of the binning areas in the vertical direction, the benefits from

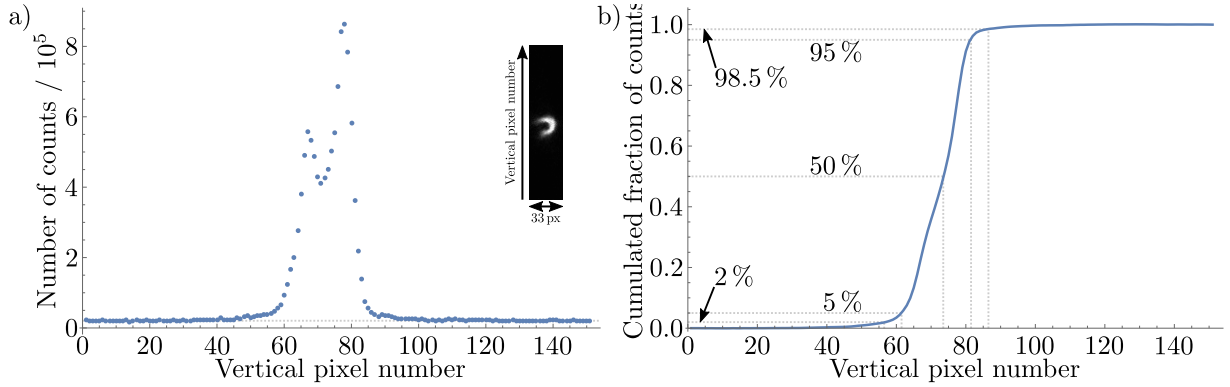

Figure 4.6: Point spread function of a single ion. a) spread in vertical direction, b) fraction of counts found in a given area in the vertical direction.

collecting more light are marginal and in addition, the risk of collecting light from a neighbouring ion increases.

The count distribution in the vertical direction for a two-ion crystal is shown in figure 4.7 for two different inter-ion distances. For this measurement, we used an exposure time of 3 seconds, an EM gain of 100, a readout rate of 30 MHz, a vertical shift speed of 0.6 µs and a camera temperature of −35 °C. The analysis of the data was done in the same way as for figure 4.6 a). To change the separation of the ions, we lowered the axial trapping potential, in this case to 20 % of its initial value.

From the plot we can tell that the minimum between the spatial count distributions of the two ions broadens and deepens when we decrease the axial trapping potential. We also notice that the height of the peaks decreases when we lower the axial trapping potential, likely caused by moving the ion(s) into a region with a lower intensity of the detection laser beam. This decreased number of counts could be compensated by moving the laser beam or by increasing the laser power to a value that

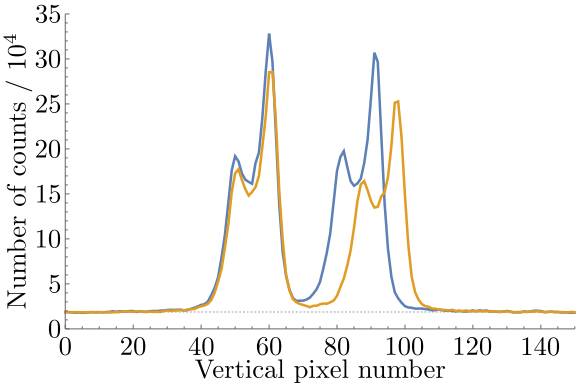

Figure 4.7: Spatial count distribution of a two-ion crystal for different ion spacing. Blue: 32 pixels separation, orange: 37 pixels separation. The gray dashed line indicates the background calculated from the outermost pixels.

results in the same number of counts that was previously reached with the smaller separation of the ions. For the measurement discussed here, we did not compensate for the mentioned effect and we will later see that this does not make a big difference in the end.

As groundwork for the following experiments, we take an image of the two-ion crystal with 100 seconds of total exposure time (see figure 4.8 a)), following the same procedure as in section 2.6.1. The image of the two-ion crystal is used as a reference for the next steps. We remove one ion from the trap and apply a suitable electric field in the axial direction on top of the trapping potential to shift the remaining ion to the position where it would be located in the two-ion crystal. By comparing the image of the ion with the two-ion reference image, we can locate the ion at the right position to better than one pixel precision, corresponding to less than 0.28(3) µm in the trap. The image of the single ion is shown in figure 4.8 b) in the lower position and in figure 4.8 c) in the upper position. The red rectangles indicate the binning areas that are used during the following experiments. We use binning areas with 33 pixels in the horizontal direction and 32 pixels in the vertical direction, spaced by a gap of 10 pixels, and one dummy area below and one above the binning areas of the ions. The described process of localizing a single ion is repeated for both inter-ion distances. Unfortunately, we forgot to change the binning area settings after changing the trapping potential; therefore, the measurement with the higher trapping potential was performed with binning area settings that were off by a few pixels. Nevertheless, the results for SPAM error and crosstalk for this configuration are remarkable.

In figure 4.8 d), the main reason for the crosstalk observed in our experiments is shown. This image uses the same raw data as figure 4.8 a), but we adjusted brightness and contrast settings to highlight the diffraction spikes, a well-known phenomenon from photography [85]. The diffraction spikes originate from the ions and extend into directions slightly tilted counterclockwise towards the horizontal and the vertical axis of the image. The observed pattern can be explained by diffraction

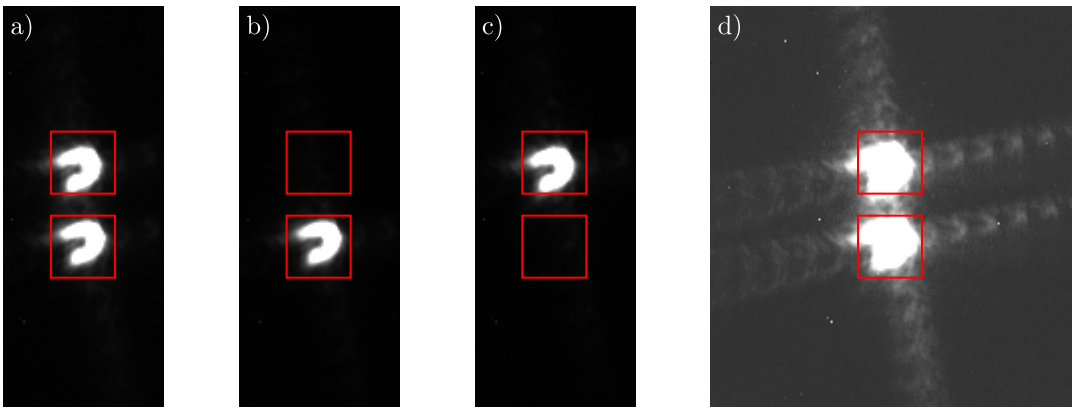

Figure 4.8: Binning area settings for a) two ions, b) one ion in the lower position, c) one ion in the upper position. d) shows the same image as a) but with adjusted brightness and contrast to make the diffraction spikes visible. All images were taken with the lowered axial trapping potential.

at two perpendicular apertures which are most likely the wires of the gold mesh that we use to shield the ions from stray charges (c.f. section 2.2.2). The direction of the observed diffraction spikes coincices with the direction of the wires of the gold mesh. We have thought of two ways to reduce the amount of crosstalk due to diffraction spikes. The mesh can be rotated, so that the diffraction spikes would not align with the axial direction of the ions, but would be tilted by 45° instead, therefore reducing the overlap between diffraction spikes and neighbouring ions. In addition to rotating the mesh, it could also be replaced by a coarser one that promises to cause weaker diffraction spikes. In another experiment in our group, a similar diffraction related problem could be solved by exchanging the mesh [86]. We have already ordered a mesh of the type "MG8" [75] from *precision Eforming* to replace the "MG17" type mesh that is currently used in our experiment and plan to exchange the mesh when we have to open the inner vacuum chamber the next time.

For the investigation of the amount of crosstalk, we prepare the ion 10^5 times alternatingly in the bright state and in the dark state each before applying the detection laser beam and repeat the process for both ion positions and for both ion separations. The measurements are performed with a readout rate of 30 MHz, a vertical shift speed of 0.6 µs, an EM gain of 1000 and camera temperature of −35 °C without regarding the temperature transient. We measure the number of counts in the binning areas of both ions with respect to the preparation scheme and the ion position which is shown in table 4.5 subdivided for both ion separations.

To calculate the amount of crosstalk, we assume that the number of counts measured in the binning area without any ion is much smaller than the number of counts measured in the binning area with an ion. Since we already know from previous measurements that an ion in the dark state produces only a very small number of counts on top of the camera's baseline (c.f. section 4.2), we conclude that an ion in the dark state will produce basically no counts at all in the empty binning area which can then be used to determine a baseline. The relative amount of counts due to crosstalk ξ generated by an ion in area i is then given by the counts above the baseline in the *wrong* area divided by the counts above the baseline in *both* areas. It can be calculated

	Global bright preparation		**Global dark preparation**		
Ion position	Area 1 counts	Area 2 counts	Area 1 counts	Area 2 counts	Crosstalk
Large separation					
Area 1	7764(6)	1259.7(2.6)	1196.5(2.7)	1166.3(2.5)	1.39(5) %
Area 2	1239.8(2.6)	7705(6)	1157.9(2.6)	1201.7(2.6)	1.24(6) %
Small separation					
Area 1	9833(7)	1295.9(2.6)	1168.9(2.7)	1182.2(2.5)	1.75(4) %
Area 2	1284.3(2.7)	9984(7)	1127.5(2.5)	1235(2.8)	1.29(4) %

Table 4.5: Results of the crosstalk measurement. The numbers indicate the average number of counts detected in the two binning areas for global preparation in the bright state or in the dark state. Numbers in brackets indicate the standard deviation.

by

$$\xi(i) = \frac{N_B(i,\bar{i}) - N_D(i,\bar{i})}{N_B(i,i) - N_D(\bar{i},i) + N_B(i,\bar{i}) - N_D(i,\bar{i})}, \tag{4.5}$$

where $N_{B/D}(j,k)$ describes the number of counts detected in area k for an ion located in binning area j and for preparation in the bright(B)/dark(D) state, and $\bar{j}$ is the *other* binning area or simply $\bar{j} = 3 - j$. The number of measured counts related to crosstalk is then 82(4) for the ion in the upper position and 93(4) for the ion in the lower position for the larger ion separation. For the smaller ion separation, the number of additional counts due to crosstalk is found to be 157(4) for an ion in the upper position and 114(4) in the bottom position. Note that area 1 is the bottom binning area.

To judge the effect of crosstalk on the order of 1 %, we have a look at the relationship between the SPAM error and the threshold value to decide between the dark state and the bright state. When a bright ion is responsible for χ additional counts in the binning area of a neighbouring ion and when we assume that an ion is in the bright state in 50 % of the detection events, it will account for $\frac{\chi}{2}$ counts due to crosstalk on average. We can therefore shift the threshold value up by $\frac{\chi}{2}$ and work with this new threshold value to determine the ion's state. In figure 4.9, the relationship between SPAM error and threshold value is shown. On the left side, the full graph of the SPAM error depending on the threshold value is shown and on the right side, the region around the minimum of the graph is enlarged. On this zoom level, the graph looks quite noisy because only very few events occur close to the minimum.

We see that the SPAM error is lower for the smaller separation of the ions. This can mainly be attributed to the laser power not being compensated after the trapping potential was changed. The relative amount of crosstalk is almost identical for both ion separations (c.f. table 4.5). This can also be seen in figure 4.8 d), where the diffraction spikes extend quite far in the vertical direction without losing strength, meaning that the amount of crosstalk is not influenced by the ion separation on the length scale investigated here. We therefore conclude that the SPAM error is dominated by the amount of detected fluorescence light and that the SPAM error would be the same for both ion separations if the laser power were compensated after changing the trapping potential. Note that the outlier at 1.75(4) % of crosstalk is caused by the incorrectly set binning areas and it will most likely be lower when the binning areas are set correctly. When we compare both ion separations with an ion in area 2, we see that the relative amount of crosstalk is identical within the uncertainty limits. The movement of the bottom ion was only marginal when reducing the axial confinement (c.f. figure 4.7), which leads to the crosstalk being almost unaffected in this case.

We see that in each of our configurations shifting the threshold value up by 100 counts only increases the SPAM error by approximately 0.01 %. We conclude that a high number of counts for an ion in the bright state is the most important parameter to achieve a low SPAM error. The higher number

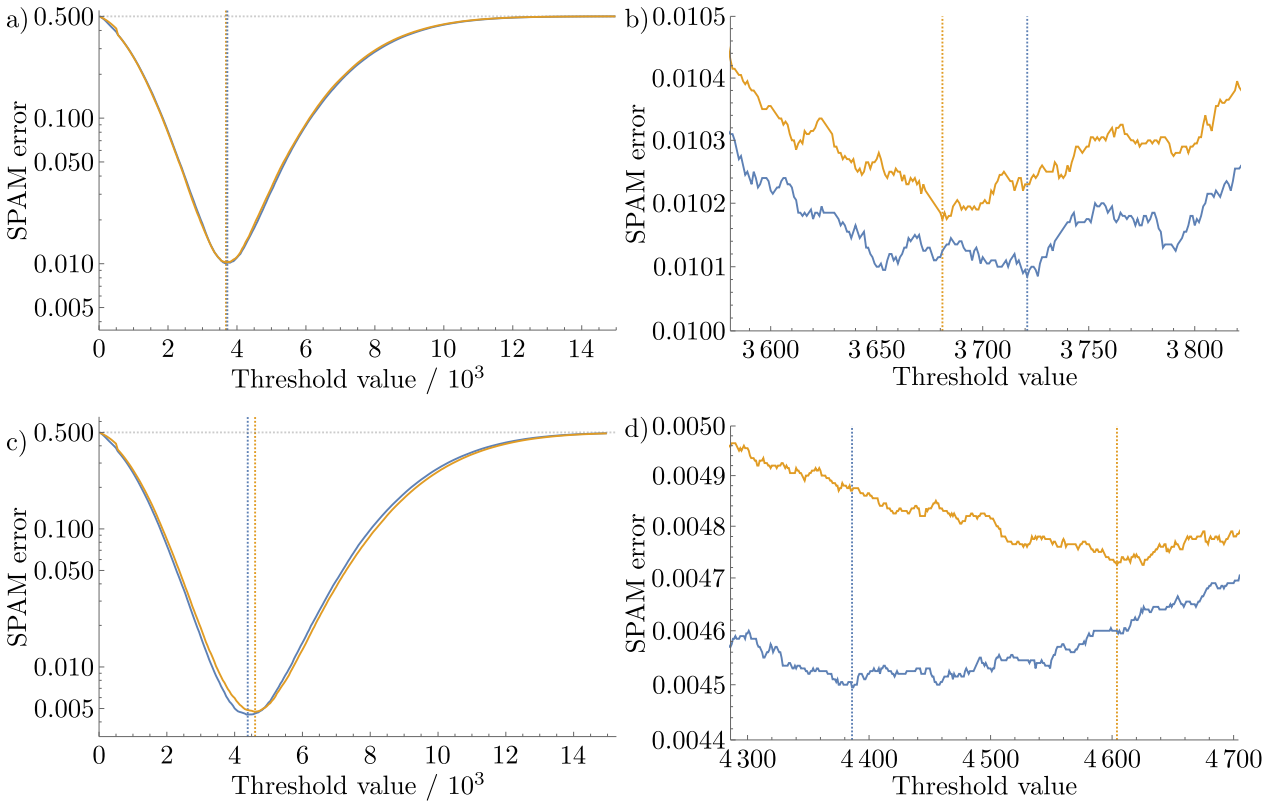

Figure 4.9: SPAM error as a function of the threshold value for the two ions. First row: larger ion separation, second row: smaller ion separation. Blue: first ion, orange: second ion. a, c) Full view; b, d) zoom-in ±100 counts around the threshold values. The vertical colored dashed lines indicate the threshold values for each ion. The horizontal gray dashed line indicates 50 %.

of counts due to crosstalk is insignificant in terms of the SPAM error. When longer chains or arrays of ions are used, we assume that the amount of crosstalk scales with the number of neighbouring ions. We can extrapolate that arrays with four or six neighbouring ions would result in a SPAM error below 1 % if all other parameters are similar to the experiment presented here and if one can manage to find suitable binning areas for those lattices.

4.4 Two-ion Rabi oscillations

In this section, we verify the previously made assumption that each ion has different Rabi frequencies in a two-ion crystal. The experimental sequence works exactly like the one described in section 4.2, but this time we extend the pulse lengths up to 1300 µs in steps of 0.4 µs and we only perform 100 repetitions for each pulse length. We conduct the measurement one time with the PMT and one time with the EMCCD camera to detect the ions' fluorescence light. With the PMT, we can only detect the collective fluorescence light of both ions; therefore, we expect to find a beat signal in case

of different Rabi frequencies as it is shown in figure 4.10. A decreasing amplitude of the oscillation as in the first half of the plot could also be explained by unwanted effects such as decoherence, but since the amplitude recovers to its original value, we are sure that this signal is produced by two ions with different Rabi frequencies.

We fit an equation describing the sum of two harmonic oscillations with different frequencies and a constant offset B of the form

$$C(t) = A_1 \sin\left(\frac{\pi}{t_{\pi_1}} t + \varphi_1\right) + A_2 \sin\left(\frac{\pi}{t_{\pi_2}} t + \varphi_2\right) + B, \tag{4.6}$$

where A_1 and A_2 are the amplitudes, t_{π_1} and t_{π_2} are the π-times and φ_1 and φ_2 are the phases of each oscillation. The best fit yields $A_1 = 26.21(18)$, $t_{\pi_1} = 2.83557(7)\,\mu s$, $\varphi_1 = 1.590(19)$, $A_2 = 23.74(18)$, $t_{\pi_2} = 2.84904(8)\,\mu s$, $\varphi_2 = 1.656(21)$ and $B = 53.00(10)$. From the fitted parameters, we can tell that the Rabi frequencies differ by approximately 0.5 %, but we cannot tell which ion oscillates faster.

We repeat the same experiment with the EMCCD camera as detector and a readout rate of 30 MHz, a vertical shift speed of 0.6 µs, EM gain of 1000, the binning areas have a size of 30×30 pixels with two binning areas below and one above the ions' binning areas, a camera temperature of $-35\,°C$

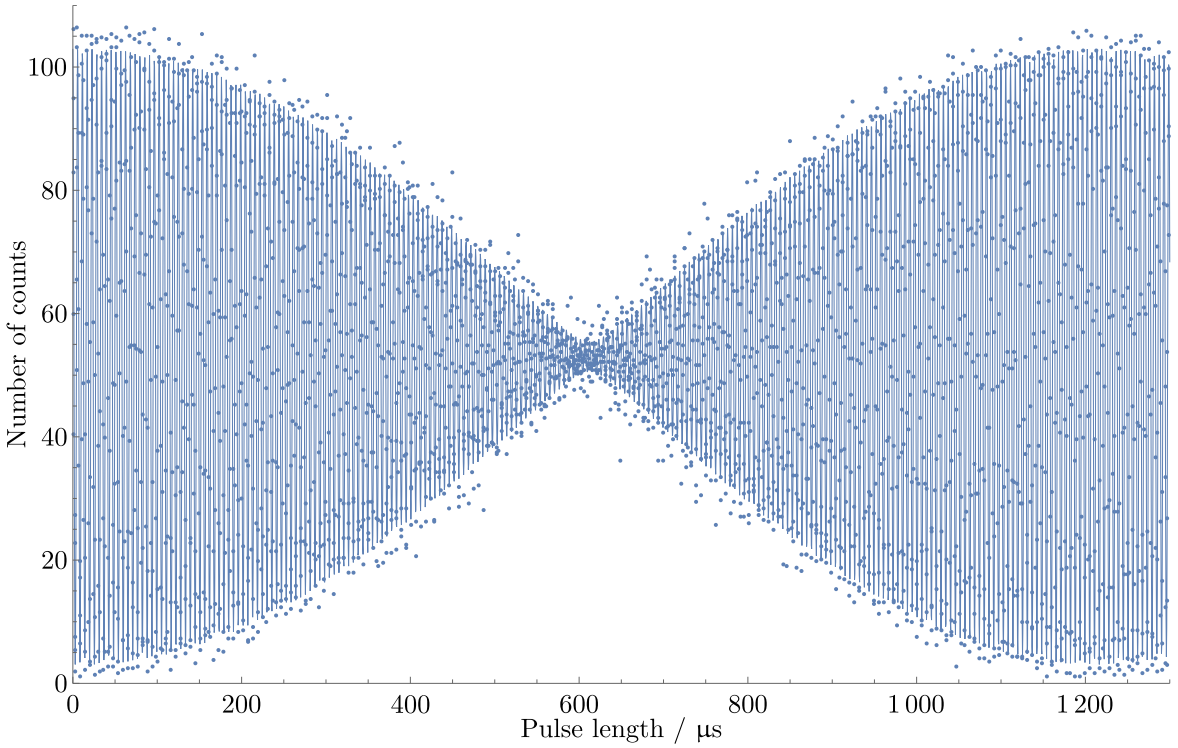

Figure 4.10: Rabi oscillations of two ions with different Rabi frequencies detected with the PMT. Points: experimental data, solid line: fit. Error bars are explicitly not shown for clarity.

and we did account for the temperature transient by running the experiment twice in a row. The measured data and sinusoidal fits of the two ions are shown in figure 4.11 for microwave pulse lengths up to 600 µs.

It is clearly visible that in the beginning, both oscillations are in phase and after approximately 600 µs they are oscillating in opposite phase. Of cause this behaviour is not due to a sudden phase jump, but because of the different Rabi frequencies of the two ions that leads to a slow "dephasing and rephasing". For pulse lengths longer than 600 µs, the oscillations are converging to an in-phase oscillation again. Since this is basically the mirrored version of the previous data, we refrain from showing it here.

We use functions of the form

$$C_i(t) = A_i \sin\left(\frac{\pi}{t_{\pi_i}} t + \varphi_i\right) + B_i \tag{4.7}$$

with $i \in \{1,2\}$ to describe the individual oscillation of ion 1 and ion 2 respectively, where A_i, t_{π_i}, φ_i and B_i follow the same nomenclature as in the measurement with the PMT. The best fit yields $A_1 = 4695(18)$, $t_{\pi_1} = 2.837688(27)\,\mu s$, $\varphi_1 = 1.759(8)$, $B_1 = 5338(13)$, $A_2 = 4723(19)$, $t_{\pi_2} = 2.851138(27)\,\mu s$, $\varphi_2 = 1.778(8)$ and $B_2 = 5417(13)$. As before, the π-times differ by approximately 0.5 %, but this time we can tell that the ion in binning area 1 (the lower one) oscillates faster.

It is worth mentioning that the time needed to determine the different Rabi frequencies from the Rabi oscillations depends on the detection method used. In figure 4.12, the fitted π-times of both ions are shown depending on the scan range of the microwave pulse length. This data is generated by fitting equations 4.6 and 4.7 to subsets of varying lengths of the original data. The grey part in figure 4.12 a) indicates the range in which the fit parameters jump so wildly that no useful information can be extracted, although we give the known final value as a starting point for the fit algorithm. While it takes a scan range of around 400 µs to reach an equilibrium of the fitted parameters for the detection with the PMT, the fits converge after around 70 µs of scan range when we use the EMCCD camera. Note that the time it takes to scan the microwave pulse length does not scale linearly with the maximum pulse length. With the script used for this measurement it takes around 3.5 minutes to scan up to 70 µs, around 22.5 minutes to scan up to 400 µs and around 97 minutes to scan up to 1300 µs.

To extract the π-times of each ion from the collective fluorescence light detected with the PMT, the microwave pulses have to be scanned almost to the node of the beat signal to allow the fit parameters to converge. This also means that the experiments take even longer when the π-times are closer together. When using the EMCCD camera for detection, the convergence time only depends on the absolute value of the π-times and not on the difference, therefore this technique is superior to check for slightly different Rabi-frequencies of two ions.

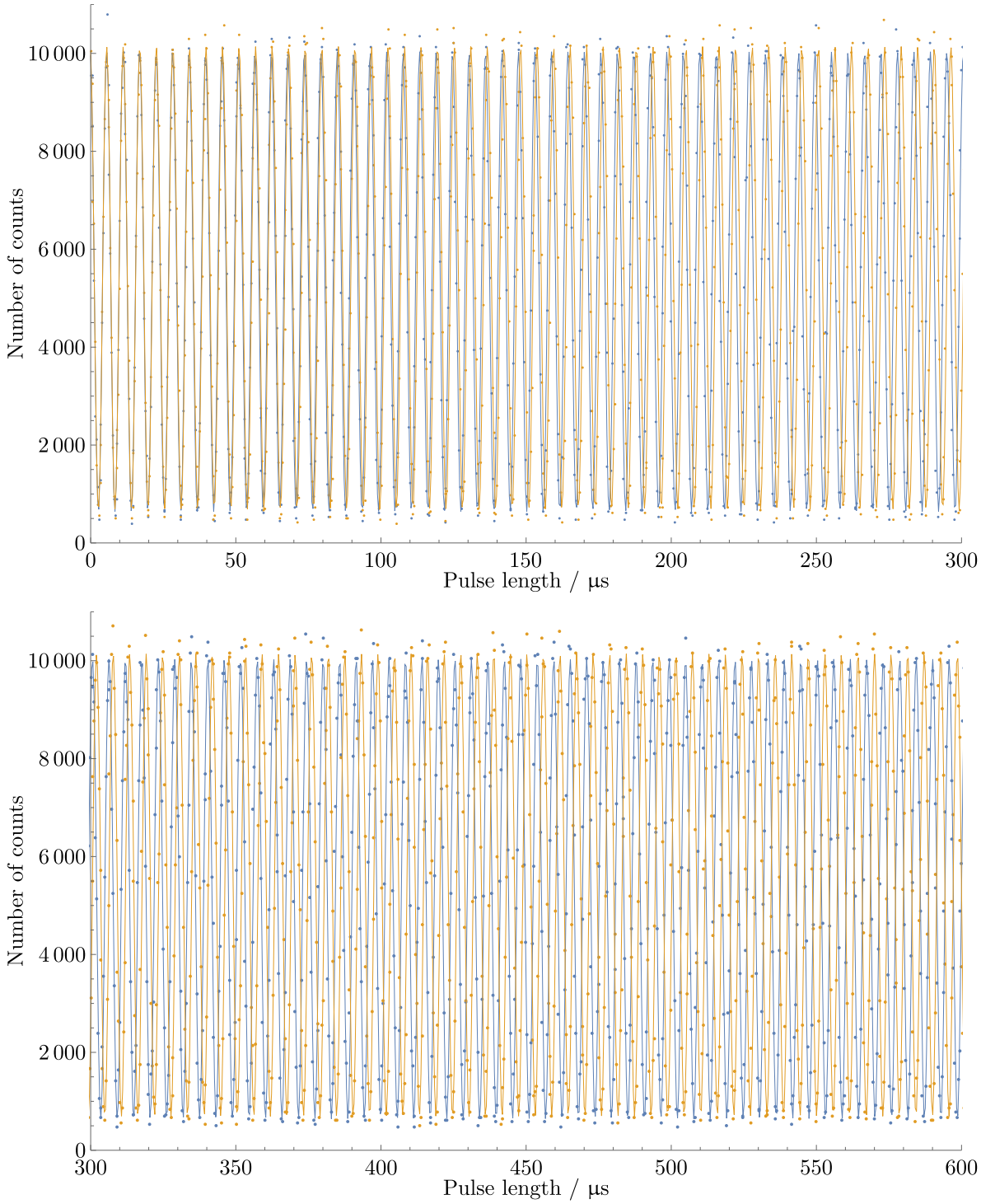

Figure 4.11: Rabi oscillations of two ions with different Rabi frequencies detected with the EMCCD camera. Blue: ion 1, orange: ion 2, points: experimental data, solid line: fit. Error bars are explicitly not shown for clarity.

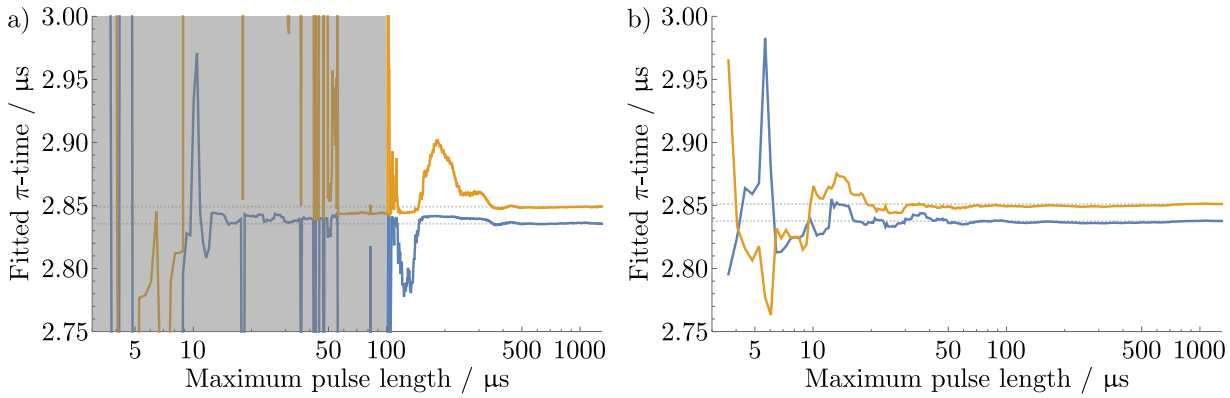

Figure 4.12: Fitted π-times for two ions depending on the maximum microwave pulse length. a) Detection with the PMT, b) detection with the EMCCD camera. Blue line: first ion, orange line: second ion. The dashed grey lines indicate the final value of the π-time for each ion.

Different Rabi-frequencies can be caused when the two-ion crystal is tilted relative to the microwave conductor that produces the oscillating magnetic field to drive the hyperfine transitions. It is possible to apply a DC field that can change this rotation angle to zero when equal Rabi frequencies of the two ions are required. It is also possible to further increase that angle to make the difference even larger and therefore enable individual-ion addressing. With the currently present difference in Rabi frequency, it takes over 200 $\pi-$times to get to a configuration where one ion is in the $|\uparrow\rangle$ state while the other ion is in the $|\downarrow\rangle$ state. We tried to use such long microwave pulses to deterministically prepare the ions in such a state, but it turned out that the Rabi frequencies are too unstable to prepare that state with a high efficiency, most likely caused by temperature drifts of the microwave amplifier that resulted in a change of the output power. Another and most likely more reliable way to implement single-ion addressing is by exploiting micromotion sideband transitions [87] in an ion crystal that is rotated in such a way that the micromotion of one ion is compensated while the other ion exhibits a high amount of micromotion.

The ability to detect the Rabi frequencies of each ion independently can be of great use in the future to find suitable DC trapping potentials that allow for efficient single ion addressing. Furthermore, it can be mandatory to detect the state of each ion simultaneously in certain quantum simulation experiments. While in quantum computation in the quantum CCD register model, one can afford to read out the information of one qubit after another, the ability to detect multiple qubits at once could still be useful for debugging and testing while setting up a quantum computer based on many ions.

5 Conclusions

5.1 Summary

In the context of this thesis, we investigated how an EMCCD camera can be utilized for individual state detection of $^9Be^+$ ions. We characterized the influence of different parameters of the EMCCD camera on the SPAM error by measuring fluorescence histograms for ions prepared in the dark state or in the bright state, respectively. We operate the camera in a mode that uses hardware binning to combine the charges of different pixels into few "macro-pixels" or binning areas. We found that defining additional binning areas in regions without any ion can be beneficial for the binning areas of interest that collect the fluorescence light of the ions. We also determined the nonlinear characteristic of the measured counts with the EMCCD camera depending of the illumination time and could show that the camera is completely insensitive to light for large binning areas and low light levels. We measured the effect of different camera temperatures on the SPAM error. We found a compromise between fast readout and low SPAM error at a maximum trigger frequency of $200\,\mathrm{s}^{-1}$ and a camera temperature of $-35\,^\circ\mathrm{C}$. At this trigger rate, the SPAM error is on the order of $0.3\,\%$ for a single ion. We also found that the temperature of the camera undergoes a transient during the first minutes of a measurement sequence. We developed a deterministic trigger scheme with low delays for the EMCCD camera to clean the sensor from charges generated during the state preparation process of the ions and to subsequently read out the sensor a second time to determine the qubit state of each ion individually.

We compared the performance of the state detection between EMCCD camera and PMT for experiments with one and two ions. We found that the difference in SPAM-error for the two detection methods is negligible as long as only one ion is concerned. However, we found that the contrast of Rabi oscillations of a single ions is higher when the ion is detected with the EMCCD camera since the binning technique makes it less sensitive to stray light. In the context of measurements with a single ion, we could also show that imperfect polarization of the cooling and detection laser has a significant influence on the SPAM error. We also investigated the effect of different detection times on the SPAM error and showed that around $400\,\mu\mathrm{s}$ are optimal. We could show that the state detection with the EMCCD camera is superior to the PMT when two ions are involved both in terms of SPAM error and in the ability to tell the state of each individual

ion. We investigated the effect of crosstalk on the SPAM error and found it to be negligible for the moment. We showed that with the EMCCD camera, we can follow coherent excitations of two ions individually and can resolve different Rabi frequencies of the two ions faster and more reliably than with a PMT.

5.2 Outlook

As already described in this thesis, the detection efficiency using the EMCCD camera can potentially be further improved by relatively simple changes. We know that the camera's firmware is not optimized for the multi-track readout mode that we are using for our measurements. Having an updated version installed in the camera's EEPROM by Andor could lead to a better discriminability between the dark state and the bright state and therefore to a lower SPAM error by increasing the sensitivity for low light levels (c.f. section 3.3). Another relatively easy but time-consuming improvement to the experimental apparatus would be to exchange the gold mesh used as part of the Faraday cage with a coarser mesh and to rotate the mesh by 45° (c.f. section 2.6.1 and 4.3.1). All the parts are already there and are ready to be put on the filterboard when the inner vacuum chamber needs to be opened the next time. Another degree of freedom that must be investigated at some point is the overall magnification factor of the imaging system and its potential influence on the SPAM error. Especially when a large number of qubits is to be read out, a smaller magnification factor is required to fit the images of all the ions onto the EMCCD sensor.

In the experiments presented in this thesis, we were solely manipulating the internal state of the ions, but did not address their motional state. Achieving control over the motional degrees of freedom of the trapped ions is the next crucial step. For this, we have to understand the origin of the motional mode drifts that we have observed in experiments that were not part of this thesis and then take measures to compensate them. One known source for motional mode drifts is a drifting amplitude of the RF voltage which generates the radial trapping potential. We already have the knowledge from our colleagues at PTB on how to deal with this problem and just have to copy their setup [61]. Another source of motional mode drifts is the time-varying heat load due to the high-power microwave sideband pulses. Some experiments were already conducted to understand this effect, but it could not be taken to an end since the motional mode drift was too high even in the absence of microwave pulses.

Once the motional modes are stable enough, we can utilize sideband transitions to implement ground state cooling. We know from the room-temperature experiment that our group runs at PTB that using Raman-transitions can be of great help at this stage. Therefore, we also plan to finish our Raman-laser setup in the near future. Once we can fully control the motion of the ions, we can start to implement a two-qubit gate based on the Mølmer-Sørensen interaction. Together

with techniques for individual ion addressing that are currently developed in our group at PTB, we will have a full set of operations to implement arbitrary quantum operations on multi-ion crystals.

At this point, the experiment control system is planned to be exchanged with the *Advanced Real-Time Infrastructure for Quantum physics* (ARTIQ). This system is much more flexible than the old *hfGui* system that we are currently using. One of its main benefits is a *Camera Link* port that allows to acquire the data measured with the EMCCD camera in real-time. Promising tests of this interface have already been performed together with Ilya Elenskiy and Daniel Fernández Barba from TU Braunschweig.

Once we have the ability to perform arbitrary quantum logic operations and to detect the state of each ion individually in real-time, we can start to run quantum simulation experiments within the collaborative research center *DQ-mat*.

List of Figures

List of Tables

Bibliography

[1] Seth Lloyd: *Universal Quantum Simulators.* Science **273**, 1073 –1078 (1996).

[2] Richard P. Feynman: *Simulating physics with computers.* International Journal of Theoretical Physics **21**, 467–488 (1982). ISSN 0020-7748.

[3] P.W. Shor: *Algorithms for quantum computation: discrete logarithms and factoring.* In *Proceedings 35th Annual Symposium on Foundations of Computer Science*, pages 124–134 (1994). doi:10.1109/SFCS.1994.365700.

[4] Lov K. Grover: *Quantum Mechanics Helps in Searching for a Needle in a Haystack.* Physical Review Letters **79**, 325–328 (1997).

[5] David P. DiVincenzo: *The Physical Implementation of Quantum Computation.* Fortschritte der Physik **48**, 771–783 (2000). ISSN 00158208, 15213978.

[6] John Clarke and Frank K. Wilhelm: *Superconducting quantum bits.* Nature **453**, 1031–1042 (2008). ISSN 1476-4687.

[7] J. I. Cirac and P. Zoller: *Quantum Computations with Cold Trapped Ions.* Physical Review Letters **74**, 4091 (1995).

[8] Gavin K. Brennen, Carlton M. Caves, Poul S. Jessen and Ivan H. Deutsch: *Quantum Logic Gates in Optical Lattices.* Physical Review Letters **82**, 1060–1063 (1999). ISSN 0031-9007, 1079-7114.

[9] M. Saffman, T. G. Walker and K. Mølmer: *Quantum information with Rydberg atoms.* Reviews of Modern Physics **82**, 2313 (2010).

[10] Daniel Loss and David P. DiVincenzo: *Quantum computation with quantum dots.* Physical Review A **57**, 120–126 (1998). ISSN 1050-2947, 1094-1622.

[11] Victor Acosta and Philip Hemmer: *Nitrogen-vacancy centers: Physics and applications.* MRS Bulletin **38**, 127–130 (2013). ISSN 0883-7694, 1938-1425. Publisher: Cambridge University Press.

[12] Stefanie Barz: *Quantum computing with photons: introduction to the circuit model, the one-way quantum computer, and the fundamental principles of photonic experiments.* Journal of Physics B: Atomic, Molecular and Optical Physics **48**, 083001 (2015). ISSN 0953-4075.

[13] Frank Arute, Kunal Arya, Ryan Babbush, Dave Bacon, Joseph C. Bardin, Rami Barends, Rupak Biswas, Sergio Boixo, Fernando G. S. L. Brandao, David A. Buell, Brian Burkett, Yu Chen, Zijun Chen, Ben Chiaro, Roberto Collins, William Courtney, Andrew Dunsworth, Edward Farhi, Brooks Foxen, Austin Fowler, Craig Gidney, Marissa Giustina, Rob Graff, Keith Guerin, Steve Habegger, Matthew P. Harrigan, Michael J. Hartmann, Alan Ho, Markus Hoffmann, Trent Huang, Travis S. Humble, Sergei V. Isakov, Evan Jeffrey, Zhang Jiang, Dvir Kafri, Kostyantyn Kechedzhi, Julian Kelly, Paul V. Klimov, Sergey Knysh, Alexander Korotkov, Fedor Kostritsa, David Landhuis, Mike Lindmark, Erik Lucero, Dmitry Lyakh, Salvatore Mandrà, Jarrod R. McClean, Matthew McEwen, Anthony Megrant, Xiao Mi, Kristel Michielsen, Masoud Mohseni, Josh Mutus, Ofer Naaman, Matthew Neeley, Charles Neill, Murphy Yuezhen Niu, Eric Ostby, Andre Petukhov, John C. Platt, Chris Quintana, Eleanor G. Rieffel, Pedram Roushan, Nicholas C. Rubin, Daniel Sank, Kevin J. Satzinger, Vadim Smelyanskiy, Kevin J. Sung, Matthew D. Trevithick, Amit Vainsencher, Benjamin Villalonga, Theodore White, Z. Jamie Yao, Ping Yeh, Adam Zalcman, Hartmut Neven and John M. Martinis: *Quantum supremacy using a programmable superconducting processor.* Nature **574**, 505–510 (2019). ISSN 0028-0836, 1476-4687.

[14] John Preskill: *Quantum Computing in the NISQ era and beyond.* Quantum **2**, 79 (2018).

[15] John Preskill: *Reliable quantum computers.* Proceedings of the Royal Society of London. Series A: Mathematical, Physical and Engineering Sciences **454**, 385–410 (1998).

[16] T.P. Harty, D.T.C. Allcock, C.J. Ballance, L. Guidoni, H.A. Janacek, N.M. Linke, D.N. Stacey and D.M. Lucas: *High-Fidelity Preparation, Gates, Memory, and Readout of a Trapped-Ion Quantum Bit.* Physical Review Letters **113**, 220501 (2014).

[17] J.P. Gaebler, T.R. Tan, Y. Lin, Y. Wan, R. Bowler, A.C. Keith, S. Glancy, K. Coakley, E. Knill, D. Leibfried and D.J. Wineland: *High-Fidelity Universal Gate Set for $^{9}Be^{+}$ Ion Qubits.* Physical Review Letters **117**, 060505 (2016).

[18] C.J. Ballance, T.P. Harty, N.M. Linke, M.A. Sepiol and D.M. Lucas: *High-Fidelity Quantum Logic Gates Using Trapped-Ion Hyperfine Qubits.* Physical Review Letters **117**, 060504 (2016).

[19] Florian Mintert and Christof Wunderlich: *Ion-Trap Quantum Logic Using Long-Wavelength Radiation.* Physical Review Letters **87**, 257904 (2001).

[20] C. Ospelkaus, C. E. Langer, J. M. Amini, K. R. Brown, D. Leibfried and D. J. Wineland: *Trapped-Ion Quantum Logic Gates Based on Oscillating Magnetic Fields.* Physical Review Letters **101**, 090502 (2008).

[21] T.P. Harty, M.A. Sepiol, D.T.C. Allcock, C.J. Ballance, J.E. Tarlton and D.M. Lucas: *High-Fidelity Trapped-Ion Quantum Logic Using Near-Field Microwaves.* Physical Review Letters **117**, 140501 (2016).

[22] G. Zarantonello, H. Hahn, J. Morgner, M. Schulte, A. Bautista-Salvador, R. F. Werner, K. Hammerer and C. Ospelkaus: *Robust and Resource-Efficient Microwave Near-Field Entangling $^9Be^+$ Gate.* Physical Review Letters **123**, 260503 (2019). ISSN 0031-9007, 1079-7114.

[23] D.J. Wineland, C. Monroe, W.M. Itano, D. Leibfried, B.E. King and D.M. Meekhof: *Experimental issues in coherent quantum-state manipulation of trapped atomic ions.* Journal of Research of the National Institute of Standards and Technology **103**, 259 (1998). ISSN 1044677X.

[24] D. Kielpinski, C. Monroe and D. J. Wineland: *Architecture for a large-scale ion-trap quantum computer.* Nature **417**, 709–711 (2002). ISSN 0028-0836.

[25] J. M. Pino, J. M. Dreiling, C. Figgatt, J. P. Gaebler, S. A. Moses, M. S. Allman, C. H. Baldwin, M. Foss-Feig, D. Hayes, K. Mayer, C. Ryan-Anderson and B. Neyenhuis: *Demonstration of the trapped-ion quantum CCD computer architecture.* Nature **592**, 209–213 (2021). ISSN 1476-4687.

[26] J. Chiaverini, R.B. Blakestade, J. Britton, J.D. Jost, C. Langer, D. Leibfried and D.J. Wineland: *Surface-electrode architecture for ion-trap quantum information processing.* Quantum Information and Computation **5**, 419–439 (2005).

[27] J. M. Amini, H. Uys, J. H. Wesenberg, S. Seidelin, J Britton, J. J. Bollinger, D. Leibfried, C. Ospelkaus, A. P. VanDevender and D. J. Wineland: *Toward scalable ion traps for quantum information processing.* New Journal of Physics **12**, 033031 (2010). ISSN 1367-2630.

[28] Kenneth Wright, Jason M. Amini, Daniel L. Faircloth, Curtis Volin, S. Charles Doret, Harley Hayden, C-S Pai, David W. Landgren, Douglas Denison, Tyler Killian, Richart E. Slusher and Alexa W. Harter: *Reliable transport through a microfabricated X -junction surface-electrode ion trap.* New Journal of Physics **15**, 033004 (2013). ISSN 1367-2630.

[29] C. Ospelkaus, U. Warring, Y. Colombe, K. R. Brown, J. M. Amini, D. Leibfried and D. J. Wineland: *Microwave quantum logic gates for trapped ions.* Nature **476**, 181–184 (2011). ISSN 0028-0836.

[30] Tony Hyun Kim, Peter F. Herskind and Isaac L. Chuang: *Surface-electrode ion trap with integrated light source.* Applied Physics Letters **98**, 214103 (2011). ISSN 0003-6951.

[31] A. P. VanDevender, Y. Colombe, J. Amini, D. Leibfried and D. J. Wineland: *Efficient Fiber Optic Detection of Trapped Ion Fluorescence.* Physical Review Letters **105**, 023001 (2010).

[32] J. True Merrill, Curtis Volin, David Landgren, Jason M. Amini, Kenneth Wright, S. Charles Doret, C-S Pai, Harley Hayden, Tyler Killian, Daniel Faircloth, Kenneth R. Brown, Alexa W. Harter and Richart E. Slusher: *Demonstration of integrated microscale optics in surface-electrode ion traps.* New Journal of Physics **13**, 103005 (2011). ISSN 1367-2630.

[33] Amira M. Eltony, Shannon X. Wang, Gleb M. Akselrod, Peter F. Herskind and Isaac L. Chuang: *Transparent ion trap with integrated photodetector.* Applied Physics Letters **102**, 054106 (2013). ISSN 0003-6951. Publisher: American Institute of Physics.

[34] W. J. Setzer, M. Ivory, O. Slobodyan, J. W. Van Der Wall, L. P. Parazzoli, D. Stick, M. Gehl, M. Blain, R. R. Kay and H. J. McGuinness: *Fluorescence Detection of a Trapped Ion with a Monolithically Integrated Single-Photon-Counting Avalanche Diode.* arXiv:2105.01235 [physics, physics:quant-ph] (2021).

[35] S. L. Todaro, V. B. Verma, K. C. McCormick, D. T. C. Allcock, R. P. Mirin, D. J. Wineland, S. W. Nam, A. C. Wilson, D. Leibfried and D. H. Slichter: *State Readout of a Trapped Ion Qubit Using a Trap-Integrated Superconducting Photon Detector.* Physical Review Letters **126**, 010501 (2021). Publisher: American Physical Society.

[36] J. A. Sedlacek, A. Greene, J. Stuart, R. McConnell, C. D. Bruzewicz, J. M. Sage and J. Chiaverini: *Distance scaling of electric-field noise in a surface-electrode ion trap.* Physical Review A **97**, 020302 (2018).

[37] J. Chiaverini and J. M. Sage: *Insensitivity of the rate of ion motional heating to trap-electrode material over a large temperature range.* Physical Review A **89**, 012318 (2014).

[38] D. A. Hite, Y. Colombe, A. C. Wilson, K. R. Brown, U. Warring, R. Jördens, J. D. Jost, K. S. McKay, D. P. Pappas, D. Leibfried and D. J. Wineland: *100-Fold Reduction of Electric-Field Noise in an Ion Trap Cleaned with In Situ Argon-Ion-Beam Bombardment.* Physical Review Letters **109**, 103001 (2012).

[39] S. Sellner, M. Besirli, M. Bohman, M. J. Borchert, J. Harrington, T. Higuchi, A. Mooser, H. Nagahama, G. Schneider, C. Smorra, T. Tanaka, K. Blaum, Y. Matsuda, C. Ospelkaus, W. Quint, J. Walz, Y. Yamazaki and S. Ulmer: *Improved limit on the directly measured antiproton lifetime.* New Journal of Physics **19**, 083023 (2017). ISSN 1367-2630.

[40] S. Debnath, N. M. Linke, C. Figgatt, K. A. Landsman, K. Wright and C. Monroe: *Demonstration of a small programmable quantum computer with atomic qubits.* Nature **536**, 63–66 (2016). ISSN 1476-4687.

[41] A. H. Burrell, D. J. Szwer, S. C. Webster and D. M. Lucas: *Scalable simultaneous multiqubit readout with 99.99% single-shot fidelity.* Physical Review A **81**, 040302 (2010).

[42] D. M. Lucas, B. C. Keitch, J. P. Home, G. Imreh, M. J. McDonnell, D. N. Stacey, D. J. Szwer and A. M. Steane: *A long-lived memory qubit on a low-decoherence quantum bus.* arXiv:0710.4421 [quant-ph] (2007).

[43] Martina Wahnschaffe: *Engineered microwave control for trapped ions.* PhD thesis, Gottfried Wilhelm Leibniz Universität, Hannover (2016).

[44] Henning Hahn: *Two-qubit microwave quantum logic gate with $^9Be^+$ ions in scalable surface-electrode ion traps.* PhD Thesis, Gottfried Wilhelm Leibniz Universität, Hannover (2019).

[45] Samuel Earnshaw: *On the nature of the molecular forces which regulate the constitution of the luminiferous ether.* Trans. Camb. Phil. Soc **7**, 97–112 (1842).

[46] H. G. Dehmelt: *Radiofrequency Spectroscopy of Stored Ions I: Storage.* In D. R. Bates and Immanuel Estermann, editors, *Advances in Atomic and Molecular Physics*, volume 3, pages 53–72. Academic Press (1968). doi:10.1016/S0065-2199(08)60170-0.

[47] Wolfgang Paul: *Electromagnetic traps for charged and neutral particles.* Reviews of Modern Physics **62**, 531–542 (1990).

[48] Pradip K. Ghosh: *Ion Traps.* International Series of Monographs on Physics. Clarendon Press, Oxford (1996).

[49] Fouad G. Major, Viorica N. Gheorghe and Günther Werth: *Charged particle traps: physics and techniques of charged particle field confinement*, volume 37. Springer Science & Business Media (2006).

[50] D.F.V. James: *Quantum dynamics of cold trapped ions with application to quantum computation.* Applied Physics B: Lasers and Optics **66**, 181–190 (1998). ISSN 0946-2171.

[51] C. Monroe, D. M. Meekhof, B. E. King, S. R. Jefferts, W. M. Itano, D. J. Wineland and P. Gould: *Resolved-sideband Raman cooling of a bound atom to the 3D zero-point energy.* Physical review letters **75**, 4011–4014 (1995). ISSN 1079-7114.

[52] P. O. Schmidt, T. Rosenband, C. Langer, W. M. Itano, J. C. Bergquist and D. J. Wineland: *Spectroscopy Using Quantum Logic.* Science **309**, 749–752 (2005).

[53] Anders Sørensen and Klaus Mølmer: *Quantum Computation with Ions in Thermal Motion.* Physical Review Letters **82**, 1971–1974 (1999).

[54] R. B Blakestad, C. Ospelkaus, A. P VanDevender, J. H Wesenberg, M. J Biercuk, D. Leibfried and D. J Wineland: *Near-ground-state transport of trapped-ion qubits through a multidimensional array.* Physical Review A **84**, 032314 (2011).

[55] Fabian Ude: *Laser und Radiofrequenzquellen für den Betrieb einer kryogenen Paulfalle.* Master's thesis, Gottfried Wilhelm Leibniz Universität, Hannover (2018).

[56] Timko Dubielzig: *Ultra-low vibration closed-cycle cryogenic surface-electrode ion trap apparatus.* Ph.D. thesis, Gottfried Wilhelm Leibniz Universität, Hannover (2020).

[57] T. Dubielzig, S. Halama, H. Hahn, G. Zarantonello, M. Niemann, A. Bautista-Salvador and C. Ospelkaus: *Ultra-low-vibration closed-cycle cryogenic surface-electrode ion trap apparatus.* Review of Scientific Instruments **92**, 043201 (2021). ISSN 0034-6748.

[58] Christopher E. Langer: *High Fidelity Quantum Information Processing with Trapped Ions.* PhD Thesis, University of Colorado, Boulder, Colorado (2006).

[59] Sebastian Grondkowski: *Pulsgenerator für die Quanteninformationsverarbeitung mit einzelnen gespeicherten Ionen.* Bachelor's Thesis, Gottfried Wilhelm Leibniz Universität, Hannover (2012).

[60] R. Bowler, U. Warring, J. W. Britton, B. C. Sawyer and J. Amini: *Arbitrary waveform generator for quantum information processing with trapped ions.* Review of Scientific Instruments **84**, 033108–033108–6 (2013). ISSN 00346748.

[61] Jonathan Morgner: *Developments towards high-fidelity entangling gates in a surface-electrode ion trap.* Master's thesis, Gottfried Wilhelm Leibniz Universität, Hannover (2020).

[62] Sebastian Grondkowski: *Quantenkontrolle von $^9Be^+$ Hyperfein-Qubits.* Master's thesis, Gottfried Wilhelm Leibniz Universität, Hannover (2014).

[63] M. Carsjens, M. Kohnen, T. Dubielzig and C. Ospelkaus: *Surface-electrode Paul trap with optimized near-field microwave control.* Applied Physics B **114**, 243–250 (2014). ISSN 0946-2171, 1432-0649.

[64] Hsiang-Yu Lo, Joseba Alonso, Daniel Kienzler, Benjamin C. Keitch, Ludwig E. de Clercq, Vlad Negnevitsky and Jonathan P. Home: *All-solid-state continuous-wave laser systems for ionization, cooling and quantum state manipulation of beryllium ions.* Applied Physics B **114**, 17–25 (2014). ISSN 1432-0649.

[65] Johannes Mielke: *A Frequency Quadrupled Lasersystem for Photoionization of ^9Be.* Master's thesis, Gottfried Wilhelm Leibniz Universität, Hannover (2016).

[66] R. W. P. Drever, J. L. Hall, F. V. Kowalski, J. Hough, G. M. Ford, A. J. Munley and H. Ward: *Laser phase and frequency stabilization using an optical resonator.* Applied Physics B **31**, 97–105 (1983). ISSN 1432-0649.

[67] A. C. Wilson, C. Ospelkaus, A. P. VanDevender, J. A. Mlynek, K. R. Brown, D. Leibfried and D. J. Wineland: *A 750-mW, continuous-wave, solid-state laser source at 313 nm for cooling and manipulating trapped $^9Be^+$ ions.* Applied Physics B **105**, 741–748 (2011). ISSN 1432-0649.

[68] Kai Voges: *Lasersysteme für Einzel-Ionen- Experimente mit $^9Be^+$*. Master's thesis, Gottfried Wilhelm Leibniz Universität, Hannover (2014).

[69] T. W. Hänsch and B. Couillaud: *Laser frequency stabilization by polarization spectroscopy of a reflecting reference cavity.* Optics Communications **35**, 441–444 (1980). ISSN 0030-4018.

[70] Hans G. Dehmelt: *Monoion oscillator as potential ultimate laser frequency standard.* IEEE Transactions on Instrumentation and Measurement **IM-31**, 83–87 (1982). ISSN 1557-9662.

[71] Mariia Stepanova: *Laser frequency stabilization for quantum logic experiments with single trapped $^9Be^+$ ions.* Bachelor's Thesis, Gottfried Wilhelm Leibniz Universität, Hannover (2014).

[72] E J Elliffe, J Bogenstahl, A Deshpande, J Hough, C Killow, S Reid, D Robertson, S Rowan, H Ward and G Cagnoli: *Hydroxide-catalysis bonding for stable optical systems for space.* Classical and Quantum Gravity **22**, S257–S267 (2005). ISSN 0264-9381.

[73] T. Andersen, K. A. Jessen and G. Sørensen: *Mean-Life Measurements of Excited Electronic States in Neutral and Ionic Species of Beryllium and Boron.* Physical Review **188**, 76–81 (1969).

[74] C. J. Foot: *Atomic Physics.* Oxford Master Series in Atomic, Optical and Laser Physics. Oxford University Press, Oxford (2005). ISBN 0-19-850696-1.

[75] Precision Eforming LLC: *Mesh Product Catalog.* https://www.precisioneforming.com/wp-content/uploads/2016/06/PEF-Mesh-Product-Catalog-2016.pdf (2016). (visited on 27th July, 2021).

[76] Hamamatsu Photonics K.K.: *Photon Counting Head H10682 Series Datasheet.* https://www.hamamatsu.com/resources/pdf/etd/H10682_TPMO1075E.pdf (2016). (visited on 14th June, 2021).

[77] Andor Technology: *iXon Ultra 888 Specifications* (2016).

[78] Gerhard Pfestorf: *Die Bestimmung der optischen Konstanten von Metallen im sichtbaren und ultravioletten Teil des Spektrums.* Annalen der Physik **386**, 906–928 (1926). ISSN 1521-3889.

[79] Johann Heinrich Lambert: *Photometria sive de mensura et gradibus luminis, colorum et umbrae.* sumptibus vidvae E. Klett, typis C.P. Detleffsen (1760).

[80] R. J. Hanisch, A. Farris, E. W. Greisen, W. D. Pence, B. M. Schlesinger, P. J. Teuben, R. W. Thompson and A. Warnock: *Definition of the Flexible Image Transport System (FITS).* Astronomy & Astrophysics **376**, 359–380 (2001). ISSN 0004-6361, 1432-0746.

[81] W. S. Boyle and G. E. Smith: *Charge coupled semiconductor devices.* The Bell System Technical Journal **49**, 587–593 (1970). ISSN 0005-8580.

[82] G. F. Amelio, M. F. Tompsett and G. E. Smith: *Experimental verification of the charge coupled device concept.* The Bell System Technical Journal **49**, 593–600 (1970). ISSN 0005-8580.

[83] Raymond Thomas Bell and David James Burt: *CCD Imagers with multiplication register.* European Patent Office, Patent number EP0866501A1 (1998).

[84] Andor Technology: *iXon Ultra 888 Hardware Guide Version 1.1* (2015).

[85] Rudolf Kingslake: *Optics in Photography.* SPIE Press (1992). ISBN 978-0-8194-0763-4.

[86] Teresa Meiners: *Characterisation of an experiment for sympathetic cooling and coupling of ions in a cryogenic Penning trap.* PhD thesis, Gottfried Wilhelm Leibniz Universität, Hannover (2021).

[87] U. Warring, C. Ospelkaus, Y. Colombe, R. Jördens, D. Leibfried and D. J. Wineland: *Individual-Ion Addressing with Microwave Field Gradients.* Physical Review Letters **110**, 173002 (2013).

List of publications

- M. Wahnschaffe, H. Hahn, G. Zarantonello, T. Dubielzig, S. Grondkowski, A. Bautista-Salvador, M. Kohnen and C. Ospelkaus: *Single-ion microwave near-field quantum sensor.* Applied Physics Letters **110**, 034103 (2017)
- T. Dubielzig, S. Halama, H. Hahn, G. Zarantonello, M. Niemann, A. Bautista-Salvador and C. Ospelkaus: *Ultra-low-vibration closed-cycle cryogenic surface-electrode ion trap apparatus.* Review of Scientific Instruments **92**, 043201 (2021)

Acknowledgements

Now is the time to express my gratitude to those who were by my side during the last years.

First of all, I thank Christian Ospelkaus who made it possible for me to work on such an interesting experiment. Many years ago, I was lured into his group with the prospect of programming FPGAs, which never happened until today. However, my knowledge about electronics evolved over time and ended in me being the guy who everyone asks when something is not working. Besides that, I was also able to learn a lot of useful things when working with lasers, vacuum chambers and cryostats or even while plumbing.

I thank Piet Schmidt and Christof Wunderlich for being co-referees for this thesis. I also thank Piet for interesting discussions during the annual status reports and the group retreats.

The next in the list is Timko Dubielzig. Most parts in the lab were raised by us together. We suffered together when winding magnetic field coils or when being in the PTB cleanroom. Over the years, I learned a lot of random things from him, be it of the culinary kind or about administration. Of course I also learned a lot from him about physics. Timko had to endure some times when I was not very helpful or did not-so-clever things in the lab. Over the years we went together through sorrow and joy. I do not know where I would be today without him. It is a pity that he was not around when the first ion was trapped in our lab.

This special honor goes to Giorgio Zarantonello. He is the one who taught me how to trap ions and who was present on 22nd November 2019 when the first ions were trapped. It feels like there is nothing that Giorgio does not know about operating the experiment.

I would also like to thank Henning Hahn for being around and trying to trap ions with us. He is also the one who discovered a design flaw in the Faraday cage that made it basically impossible for the ablated Beryllium atoms to reach the trap.

Many thanks also go to my co-workers Niklas Orlowski and Celeste Torkzaban. They recently (on my timescales of working on this experiment) joined me in the lab after a period of being the only one. This really helped a lot in keeping up with the natural decay in the lab. I also thank Niels Kurz and Chloë Allen-Ede for joining our team. I am looking forward to working with you in the near future.

I also thank the many students who wrote their theses at this experiment or just worked as research assistants. Everyone of them left behind something more or less useful that stayed in the lab. I specially want to praise Fabian Ude who spent ages trying to understand and fix our RF resonator and the 940 nm laser. Unforgotten will be that he answered the question “Wie läuft’s” with “runter”.

I also had to do with people from the QLEDS experiment who deserve being mentioned here. I have to thank Teresa Meiners for answering all of my questions regarding optics and Zemax that Timko did not answer. I thank Johannes Mielke for the helpful discussions about lasers and cavities. Last but not least I thank my former office colleague Malte Niemann. He can criticize everything. Most of the time there is something useful buried under all that grumbling. I enjoyed attending the coffee breaks he took with Timko in our office talking about random stuff or commenting on people on the internet.

Our experiment would simply fall apart without all of the custom-made mechanical parts that were designed by us and often did not fit or work in the first attempt. Many thanks go to the people in the precision mechanics workshop for their never-ending efforts in building things for us.

I also would like to thank the people sitting in the offices and doing paperwork all day long to keep the institute running. Without people like Gunhild Faber, Elke Hünitzsch, Katrin Pfennig, Madeleine-Yasmin Miltsch, Stephanie Kaisik, Bianca Thiel, Birgit Ohlendorf and Barbara Thiele-Bode I would have been lost. Thank you for your support in dealing with unpleasant invoices, customs forms, work contracts or simply operating the laminator.

Finally, I would like to thank my friends and family, specially my wife Kristin Halama, with whom I spent by far the most time in the last one and a half years between lockdown and home office. Thank you all for being part of my life!

Sebastian Halama

né Grondkowski
Lilienweg 24A
30916 Isernhagen

Research

08/2014 - 11/2021 | **Doctoral Studies**

Leibniz Universität Hannover
Institut für Quantenoptik

PhD thesis in the group of Prof. Dr. Christian Ospelkaus

Real-time capable individual-ion qubit measurement

University

10/2011 - 09/2014 | **Master of Science (Physics)**

Leibniz Universität Hannover
Institut für Quantenoptik

Master's thesis in the group of Prof. Dr. Christian Ospelkaus

Quatenkontrolle von $^9Be^+$ Hyperfein-Qubits

10/2008 - 03/2012 | **Bachelor of Science (Physics)**

Leibniz Universität Hannover
Institut für Quantenoptik

Bachelor's thesis in the group of Prof. Dr. Christian Ospelkaus

Pulsgenerator für die Quanteninformationsverarbeitung mit einzelnen gespeicherten Ionen

School

09/1998 - 06/2007 | **Abitur**

Gymnasium Andreanum, Hildesheim